Study of the dissolution kinetics of montmorillonite, biotite and phlogopite (2:1 phyllosilicates) and reaction mechanisms

Chiara Cappelli

PhD Thesis

Granada, Marzo 2015

Editorial: Universidad de Granada. Tesis Doctorales
Autora: Chiara Cappelli
ISBN: 978-84-9125-100-2
URI: http://hdl.handle.net/10481/40151

Study of the dissolution kinetics of montmorillonite, biotite and phlogopite (2:1 phyllosilicates) and reaction mechanisms

Estudio de la cinética de disolución de montmorillonita, biotite y flogopita (filosilicatos 2:1) y mecanismos de reacción

Memoria de Tesis presentada por la Licenciada Dña. Chiara Cappelli para optar al grado de Doctor por la Universidad de Granada.

Esta Tesis Doctoral ha sido dirigida por los Drs. F. Javier Huertas Puerta, Investigador Científico del CSIC en el Instituto Andaluz de Ciencias de la Tierra (CSIC-UGR), y Jordi Cama, Científico Titular del CSIC en el Instituto de Diagnóstico Ambiental y Estudios del Agua (CSIC)

Granada, 6 de marzo de 2015

Vº Bº de los Directores La Doctoranda

F. Javier Huertas Puerta Jordi Cama Chiara Cappelli

Esta Tesis Doctoral ha sido financiada por los proyectos del Plan Nacional de I+D+i CGL2008-01652 y CGL2011-22567 y el Grupo de Investigación RNM-264 de la Junta de Andalucía, con contribución de fondos FEDER y la beca del programa de Formación de Profesorado Universitario (MEC). El trabajo de investigación ha sido desarrollado en su mayor parte en el Instituto Andaluz de Ciencias de la Tierra (CSIC-Universidad de Granada) y en la Estación Experimental del Zaidín (CSIC), con estancias breves en el Instituto de Diagnóstico Ambiental y Estudios del Agua (CSIC) y en MARUM - Center for Marine Environmental Sciences (Universidad de Bremen)

Declaración de originalidad

La doctoranda Chiara Cappelli y los directores de la tesis F. Javier Huertas Puerta y Jordi Cama garantizamos, al firmar esta tesis doctoral, que el trabajo ha sido realizado por el doctorando bajo la dirección de los directores de la tesis y hasta donde nuestro conocimiento alcanza, en la realización del trabajo, se han respetado los derechos de otros autores a ser citados, cuando se han utilizado sus resultados o publicaciones.

Originality statement

I, the PhD candidate Chiara Cappelli, and the supervisors, F. Javier Huertas Puerta and Jordi Cama, hereby declare that this submission is my own work and to the best of my knowledge it contains no materials previously published or written by another person, or substantial proportions of material which have been accepted for the award of any other degree or diploma at University of Granada or any other educational institution, except where due acknowledgement is made in the thesis. Any contribution made to the research by others, with whom I have worked at University of Granada or elsewhere, is explicitly acknowledged in the thesis. I also declare that the intellectual content of this thesis is the product of my own work, except to the extent that assistance from others in the project's design and conception or in style, presentation and linguistic expression is acknowledged.

Granada, 6 de marzo de 2015

Vº Bº de los Directores — La Doctoranda

F. Javier Huertas Puerta — Jordi Cama — Chiara Cappelli

Abstract

The kinetics of phyllosilicate dissolution has been extensively studied over the last 20 years. In particular, special attention has been paid to understand the effect that pH exerts on the dissolution mechanisms and rate. Only a few works have studied the effect of the degree of undersaturation (ΔG_r; Gibbs free energy) on some phyllosilicates (smectite and chlorite) dissolution rates. Within this context, this Thesis focuses on the dissolution kinetics of biotite, phlogopite and montmorillonite in acidic pH from 1 to 4 and temperature ranging from 11.5 to 100 °C. Dissolution of biotite and phlogopite was studied in the absence or presence of oxalic acid.

The dissolution of biotite and phlogopite was studied from the alteration of the (001) basal surfaces using complementary techniques (atomic force microscopy -AFM-, vertical scanning and phase shifting interferometry -VSI/PSI- and laser confocal microscopy with differential interference contrast microscopy - LCM-DIM) that allowed obtaining precise information of surface reactivity and topography at the micro- and meso-scales over long time periods. Special emphasis was given to LCM-DIM because it was the first time this technique has been used by first time to monitor *in situ* phyllosilicate dissolution and derive dissolution kinetics. Montmorillonite dissolution was studied using powder samples based on the variation in aqueous concentration of the outflow samples. Batch and well mixed flow-through experiments were combined.

Dissolution of montmorillonite. Regarding montmorillonite , the dissolution kinetics was investigated using well-mixed flow-through reactors at 25°C at pH ranging from 2 to 4 and variable solution saturation state. The objective was to measure the dependence of K-montmorillonite dissolution rate on pH as well as on degree of undersaturation. The K-montmorillonite dissolution rate increases by decreasing pH and decreases slowly as a function of the ΔG_r of reaction, which is a quantitative measure of the degree of undersaturation.

The K-montmorillonite dissolution rate as a function of pH and chemical affinity (ΔG_r) at 25 °C can be fit reasonably well with the following expression:

$$\mathrm{R(mol\ g^{-1}\ s^{-1})} = 10^{9.74\pm0.07} \cdot a_{H^+}^{0.58\pm0.01} \cdot \left(1 - \exp\left(-3.8 \times 10^{-4} \cdot \left(\frac{|\Delta G_r|}{RT}\right)^{2.13}\right)\right)$$

The nonlinearity of the rate law shows that the undersaturation ($\Delta Gr < -40$ kcal mol^{-1}) required to reach a limiting far-from-equilibrium rate (the so-called “dissolution plateau”) is

similar to those determined for smectite at pH 8.8 and 9 and 80 and 25 °C (Cama et al., 2000; Marty et al., 2011) and pH 3 and 50 °C (Metz, 2001) and chlorite at pH 3-7.5 and 100 °C (Zhang et al., 2015).

The rate law obtained in this study provides a basis for modeling montmorillonite mineral dissolution over a range of pH and saturation conditions, which is essential in applications such as acid mine drainage and geological CO_2 sequestration.

Dissolution of biotite and phlogopite. A systematic, *in situ*, and real time exploration of broad regions of the reacting biotite and phlogopite (001) basal surfaces (in the order of tens of thousands square micrometers) was performed using the recently developed non-invasive LCM-DIM technique. Although unambiguous quantitative information on the vertical surface topography is unavailable with LCM-DIM, horizontal quantification is possible, and measurements of step edge retreat with time were performed. Time-lapse image sequences of large areas (up to 1 mm) of the evolving cleavage (001) biotite surface showed that dissolution in nitric acid mainly occurs at surface edges. In addition, in contrast to an observed rapid dissolution at low steps (few layers), swelling and collapse of the edge layers occurred at high steps (many layers).

At pH 1, an increase in temperature enhanced the surface edge dissolution from 7.5×10^{-4} µm s^{-1} at 11.5 °C to 6.2×10^{-2} µm s^{-1} at 70 °C. Although dissolution of surface edges dominated the biotite dissolution reaction in nitric acid, dissolution at the basal planes also occurred. AFM exploration of the basal surface at pH 1 and 70 °C showed an uniform distribution of etch pits (≈20-60 nm diameter, 3 nm depth) indicating that the biotite basal surface also contributes to the overall dissolution reaction. Similar to biotite dissolution in nitric acid solutions, in the presence of oxalic acid, biotite (001) surface dissolution was controlled by both the step edge alteration and formation of etch pits. In general, VSI/PSI and LCM-DIM exploration shows frequently large circular and/or hexagonal or pseudo-hexagonal etch pits on the reacted biotite (001) surface.

Comparison between pristine and reacted basal surfaces of phlogopite shows that step retreat and formation of triangular-shaped etch pits are the mechanisms responsible for phlogopite dissolution.

The degree of undersaturation (ΔG_r) is likely the main factor controlling the predominance of one dissolution mechanism over the other. Etch pits generate from surface defects on the mica (001) surface in presence of both the HNO_3 and oxalic acids but hardly grow during dissolution with HNO_3. Formation of aqueous complexes of released cations

($Al(Ox)_3^{3-}$, $Fe(Ox)_3^{3-}$, $Mg(Ox)_2^{2-}$) lower ΔG_r below ΔG_{crit}, allowing etch pits to expand following the stepwave pattern. Triangular etch pits always open up on phlogopite surface being its density higher in the case of reaction with oxalic acid solutions. Phlogopite dissolves slower than biotite does.

Resumen

La cinética de disolución de los filosilicatos ha sido ampliamente estudiada a lo largo de los últimos 20 años. Particularmente, se ha puesto una especial atención en comprender el efecto que ejerce el pH sobre el mecanismo y la velocidad de disolución. Se han realizado sólo unos pocos estudios sobre el efecto del grado de saturación (ΔG_r) sobre la velocidades de disolución de algunos filosilicatos (esmectita y clorita). Dentro de este contexto esta Tesis se dirige al estudio de la cinética de disolución de biotita, flogopita y montmorillonita en pH ácido (1-4) y rango de temperatura desde 11.5 a 100 °C. La disolución de biotita y flogopita fue estudiada en soluciones libres de ligandos o en presencia de ácido oxálico.

La disolución de biotita y flogopita ha sido estudiada mediante la monitorización de las alteraciones sufridas por la superficie basal (001) usando técnicas complementarias como atomic force microscopy (AFM), vertical scanning and phase shifting interfeometry (VSI/PSI) and laser confocal microscopy with differential interference contrast microscopy (LCM-DIM)) que suministran información precisa de la reactividad y topografía de la superficie a escala micro y meso-métrica durante intervalos de tiempo largos. Se ha dado una especial atención al LCM-DIM por ser la primera vez que se utiliza esta técnica para obtener medidas *in situ* de disolución de filosilicatos. La disolución de montmorillonita se ha estudiado en muestras en polvo a partir de la variación de las concentraciones de los cationes estructurales en las disoluciones alterantes a la salida del reactor. El estudio de disolución de filosilicatos 2:1 se han realizado mediante experimentos en reactores batch y de flujo continuo.

Disolución de montmorillonita. La cinética de disolución de la K-montmorillonita fue investigada usando reactores de flujo continuo a 25 °C y en un rango de pH de 2 a 4 y estado variable de saturación de la solución. El objetivo fue medir la dependencia de la velocidad de disolución de K-montmorillonita tanto con el pH como con el grado de saturación. La velocidad de disolución de la K-montmorillonita aumenta con el descenso del pH y disminuye lentamente en función del ΔG_r de reacción, que es una medida cuantitativa del grado de saturación.

La velocidad de disolución de K-montmorillonita en función del pH y de la saturación de la solución (ΔG_r) a 25 °C se ajusta razonablemente a la siguiente expresión:

$$\mathrm{R(mol\,g^{-1}\,s^{-1})} = 10^{9.74\pm0.07} \cdot a_{H^+}^{0.58\pm0.01} \cdot \left(1 - \exp\left(-3.8 \times 10^{-4} \cdot \left(\frac{|\Delta G_r|}{RT}\right)^{2.13}\right)\right)$$

La no linealidad de la ley de velocidad muestra que la saturación ($\Delta Gr < -40$ kcal mol^{-1}) requerida para alcanzar la velocidad en condiciones lejos del equilibrio (*plateau de disolución*) es similar a aquellas determinadas para esmectita a pH 8.8 y 9 a 80 y 25 °C respectivamente (Cama et al., 2000; Marty et al., 2011), pH 3 a 50 °C (Metz, 2001) y clorita a pH 3-7.5 a 100 °C (Zhang et al., 2015).

La ley de velocidad obtenida en este estudio proporciona una base para modelar la disolución de la montmorillonita en un rango de pH y condiciones de saturación, lo que es esencial en aplicaciones como el drenaje ácido de minas y el almacenamiento geológico de CO_2.

Disolución de biotita y flogopita. Utilizando LCM-DIM como técnica no invasiva, se realizó una exploración sistemática, *in situ* y en tiempo real de áreas amplias (del orden de decenas de miles de micrómetros cuadrados) de las superficies basales de biotita y flogopita durante su alteración. A pesar de la ambigüedad de la información cuantitativa proporcionada por LCM-DIM de la topografía de la superficie en la dirección vertical (z), se puede realizar una cuantificación en el plano x-y midiendo el retroceso del borde de los escalones con el tiempo. Las secuencias temporales de imágenes de amplias áreas (más de 1 mm^2) de la superficie basal de biotita en el proceso de alteración muestran que, en presencia de ácido nítrico, la disolución se produce principalmente desde la superficie de los bordes de los cristales. Además, contrariamente a una rápida disolución de los escalones más bajos (pocas láminas), a lo largo de los escalones más altos (varias laminas) se observa un proceso de hinchamiento (*swelling)* seguido de colapso de las laminas.

A pH 1, el aumento de la temperatura desde 11.5 a 70 °C induce un aumento de la velocidad de disolución de la superficie de los bordes desde 7.5×10^{-4} a 6.2×10^{-2} µm s^{-1} respectivamente. Aunque en soluciones de ácido nítrico la disolución de la superficie de los bordes domina la reacción de disolución de biotita, también se produce disolución en el plano basal. La exploración de la superficie basal mediante AFM a pH 1 y 70 °C muestra una distribución uniforme de *etch pits* (20-60 nm de diámetro, 3 nm de profundidad), indicando que la superficie basal de la biotita contribuye a la disolución general. Tanto en disoluciones libres de oxálico como en presencia de ácido oxálico la disolución de la superficie de biotita está controlada por la alteración del borde de los escalones y por la formación de *etch pits*. En general, las observaciones mediante VSI/PSI y LCM-DIM muestran frecuentemente grandes *etch pits* circulares y/o hexagonales o pseudo-hexagonales en la superficie (001) de la biotita alterada.

La comparación entre las superficie basal de flogopita alterada y no alterada indica que el retroceso de los escalones y la formación de *etch pits* triangulares son los mecanismos responsables de su disolución.

El grado de saturación (ΔG_r) es probablemente el factor principal que controla el predominio de un mecanismo de disolución sobre el otro. Los *etch pits* se generan a partir de los defectos en la superficie basal de las micas en presencia bien de HNO_3 o de ácido oxálico, pero difícilmente crecen durante la disolución en HNO_3. La formación de complejos acuosos de los cationes disueltos ($Al(Ox)_3^{3-}$, $Fe(Ox)_3^{3-}$, $Mg(Ox)_2^{2-}$) provoca la disminución de ΔG_r por debajo de ΔG_{crit}, permitiendo que los *etch pits* se expandan siguiendo el patrón de *stepwave*. Los *etch pits* triangulares siempre se generan y crecen en la superficie de flogopita, siendo su densidad mayor en el caso de alteración con acido oxálico. La flogopita en general se disuelve más lentamente que la biotita.

Table of Contents

List of figure

Table heads

1 INTRODUCTION

Kinetic and thermodynamic studies of mineral alteration have yielded an extensive understanding of mineral behavior in Earth surface processes such as weathering and diagenetic transformations. From both approaches we have been enlarging our knowledge of the role that minerals play in the (bio)geochemical cycles of the elements. As Lasaga (1998) asserted in his book "Kinetic Theory in the Earth Science", quantification of earth science processes is not possible without a proper understanding of kinetics.

During the last three decades a great number of laboratory experiments and field studies have been performed to quantify mineral dissolution/precipitation rates and unravel the mechanisms that control mineral weathering. Silicates, as the most abundant minerals on Earth crust, have been extensively investigated. And within silicates, phyllosilicates are, at present, object of many studies because the often-contradictory experimental data leave the interpretation of their reactivity still unclear. The layered TO and TOT structures of phyllosilicates (Figure 1.1) along with isomorphic substitutions and mineralogical composition, make this minerals' reactivity be complex. A relevant consequence is that as phyllosilicates dissolve or precipitate, the distinct faces in contact with aqueous media show different reactivity. For this reason, the study of the dissolution and precipitation of phyllosilicates at the laboratory scale has not been a trivial task.

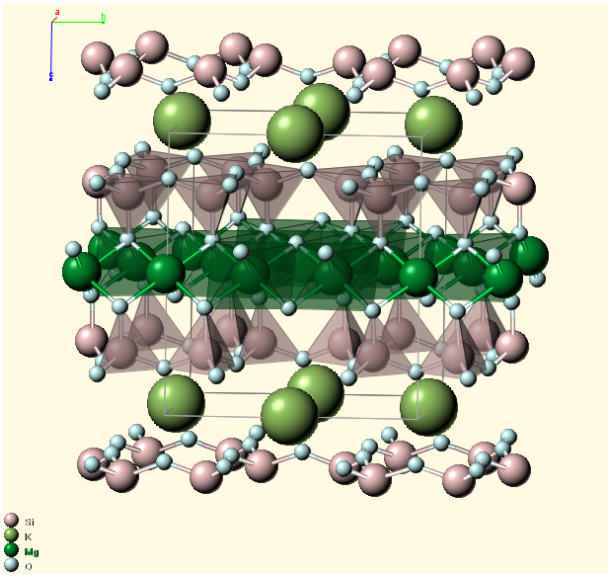

Figure 1.1. Crystallographic structure of Mg-biotite from *http://www.webmineral.com*. The cubic gray frame indicates a unit cell.

At the laboratory scale dissolution kinetics of phyllosilicates has been mainly investigated by means of flow-through and batch reactors (open and close systems, respectively) in which powdered samples react with the solution. The resulting variation in aqueous chemistry allows calculation of the phyllosilicate dissolution rates under different experimental conditions (Clemency and Lin, 1981; Knauss and Thomas J, 1989; Nagy et al., 1991; Acker and Bricker, 1992; Turpault and Trotignon, 1994; Ganor et al., 1995; Kalinowski and Schweda, 1996; Zysset and Schindler, 1996; Malmström and Banwart, 1997; Bauer and Berger, 1998; Huertas et al., 1999; Cama et al., 2000; Huertas et al., 2001; Metz and Ganor, 2001; Cama et al., 2002; Köhler et al., 2003; Amram and Ganor, 2005; Metz et al., 2005a; Oelkers et al., 2008; Rozalén et al., 2009b; Bibi et al., 2011; Ramos et al., 2011). Additionally, inspection of the solid samples has proved to be essential in the study of phyllosilicates dissolution kinetics. On the one hand, electron beam-based microscopy techniques, such as scanning electron microscopy (SEM) and transmission electron microscopy (TEM) with energy-dispersive X-ray spectroscopy (EDS) detectors have been used to characterize the variation in composition and structure of the solids. On the other hand, another group of microscopic techniques, such as atomic force microscopy (AFM), vertical scanning and phase shifting interferometry (VSI and PSI) and laser confocal microscopy combined with differential interferometry microscopy (LCM-DIM), has been used to characterize the reacting mineral surfaces and to measure variations in surface topography during dissolution/precipitation reactions, allowing the investigation of the reaction mechanisms at the solid/solution interface (Baba et al., 1997; Rufe and Hochella, 1999; Bosbach et al., 2000; Bickmore et al., 2001; Brandt et al., 2003; Tournassat et al., 2003; Yokoyama et al., 2005; Kuwahara, 2006; Aldushin et al., 2007; Kuwahara, 2008; Sánchez-Pastor et al., 2010; Haward et al., 2011; Kurganskaya et al., 2012; Pachana et al., 2012; Cappelli et al., 2013; Kurganskaya and Luttge, 2013; Satoh et al., 2013; Ueta et al., 2013a).

1.1 Thesis motivation

From the current knowledge on the reactivity of 2:1 phyllosilicates, there were two issues that drew my attention.

1. The first one concerns smectite reactivity. In the last two decades bentonite and especially smectite minerals have been object of study due to its importance in the stability of multibarrier systems for the storage of high-level nuclear waste in burial repositories. The high cation exchange capacity of smectite in this underground repository allows the confinement

of metals canister impeding its interaction with the groundwater. Because of its scientific and economic interest smectite stability has been investigated under several environmental conditions. Laboratory experiments of smectite dissolution have been performed in order to assess the effect that pH (Zysset and Schindler, 1996; Bauer and Berger, 1998; Amram and Ganor, 2005; Golubev et al., 2006; Rozalén et al., 2008), temperature (Amram and Ganor, 2005; Rozalén et al., 2009a; Rozalén et al., 2009b; Lee et al., 2010), organic acids and inhibitors/catalysts (Cambier and Sposito, 1991; Charlet et al., 1993; Golubev et al., 2006; Ramos et al., 2011) exerts on the smectite dissolution rate. Likewise, the role of the smectite reactive surface area has been investigated (Bosbach et al., 2000; Bickmore et al., 2001; Tournassat et al., 2003; Metz et al., 2005b; Yokoyama et al., 2005; Kuwahara, 2006; Satoh et al., 2013).

While the effects of pH, temperature, organic acids, catalysts or inhibitors on the smectite dissolution rates have been studied over the whole pH range (1-14), the effect of the solution saturation state (ΔG_r) on the smectite dissolution rate has only been investigated under alkaline conditions (Cama et al., 2000; Marty et al., 2011) and some results were obtained at pH 3 (Metz, 2001). Hence, the effect of the solution saturation state on the smectite dissolution rate in acidic pH range remains still unknown.

2. The second question was that although the reactivity of 2:1 phyllosilicates has been extensively studied, the mechanisms that control the reactivity of the basal surface of mica minerals in acidic pH remained also unclear. Flow-through reactors (open system) were mostly used to study the reaction mechanisms of mica dissolution and possible formation of new phases (e.g. aluminum and iron oxides and hydroxides or vermiculite) (Clemency and Lin, 1981; Kuwahara and Aoki, 1995; Malmström et al., 1996; Malmström and Banwart, 1997; Taylor et al., 2000b; Murakami et al., 2003; Samson et al., 2005). It is argued that at acidic pH phyllosilicate dissolution predominantly takes place at the clay mineral edge surface (Brantley and Conrad, 2008). Previous studies of dissolution of kaolinite (Ganor et al., 2003) and biotite (Acker and Bricker, 1992; Turpault and Trotignon, 1994; Kalinowski and Schweda, 1996) using powder samples and single biotite crystals showed that the contribution of the edge surface area to the dissolution rate is higher than the basal surface area, suggesting that the edge sites dissolve faster than the basal surface sites and often control the overall dissolution rate under acidic conditions.

Direct information about the reactivity of the different crystal faces, specific dissolution-precipitation mechanisms and location of secondary mineral formation has been gained using advanced microscope techniques (AFM, VSI, PSI and LCM-DIM). *In situ* and *ex situ*

observation of the mineral surfaces with high spatial (both vertical and horizontal) resolution allows characterization of the morphological and topographical changes that occur during the mineral alteration processes. AFM has been the most frequently used technique to investigate the reaction mechanisms of phyllosilicates dissolution. Dissolution features and precipitated phases were identified over a field of view ranging between hundreds of nm and 20 µm with a vertical nanometric resolution (Baba et al., 1997; Bickmore et al., 1999; Nagy et al., 1999; Rufe and Hochella, 1999; Bosbach et al., 2000; Bickmore et al., 2001; Brandt et al., 2003; Yokoyama et al., 2005; Aldushin et al., 2006; Kuwahara, 2006; Aldushin et al., 2007; Kuwahara, 2008; Sánchez-Pastor et al., 2010; Haward et al., 2011; Pachana et al., 2012; Satoh et al., 2013).

Rufe and Hochella (1999) assessed quantitatively the reactive surface area of dissolving phlogopite at acidic conditions and room temperature. Although the basal (001) surfaces showed certain reactivity, the dissolution rates normalized to the edge surface area were two orders of magnitude faster than rates normalized to the total surface area for this mineral. Bosbach et al. (2000) and Bickmore et al. (2001) showed that the basal surfaces of two smectite (hectorite and nontronite) crystallites appeared to be unreactive during the time scale of the experiments in acid solutions. At high temperature (100 - 140 °C), Aldushin et al. (2006) investigated the reactions of phlogopite and apophyllite with acidic solutions and observed that phlogopite dissolution occurred via nucleation of etch pits on the pristine surface, implying that the basal surface plays an important role in the dissolution processes, at least at elevated temperatures. The apophyllite basal surface underwent a swelling process forming square-shaped hillocks. McMaster et al. (2008) and Haward et al. (2011) suggested that etch pit nucleation at the biotite basal plane controls the biotite dissolution in the presence of oxalic acid. In the absence of oxalate, however, formation of discrete etch pits at room temperature was not observed. Pachana et al. (2012) based on SEM and AFM examinations observed stair-shaped etch pits on muscovite and biotite during hydrothermal (200 °C) alteration in acidic solutions (pH 1.1-5.7) and identified the role that coating phases exert on the control of mineral alteration.

Micro-topographical, *ex-situ* observations of silica minerals surface in larger field of view (90 µm - 1.5 mm) are possible using interferometry techniques also with a nanometric vertical resolution (e.g., VSI) (Luettge et al., 1999; Lüttge, 2006; Buss et al., 2007; Kurganskaya et al., 2012; Satoh et al., 2013). More recently a new designed high-resolution Phase Shifting Interferometer (PSI) has allowed the measurement of extremely low surface reaction rates of mineral surfaces submerged in aqueous solution (Banfield and Eggleton, 1990; Sorai et al.,

2007; Van Driessche et al., 2011; Ueta et al., 2013b; King et al., 2014) and was applied also to phyllosilicate dissolution study (Ueta et al., 2013a).

In the study on mica dissolution kinetics Kurganskaya et al. (2012) observed etch pits formation on muscovite (001) surface at high pH and temperature (pH=9.4, 155 °C). They interpreted dissolution mechanism in the light of stepwave theory introduced by Lasaga and Luttge (2001): trains of steps spreading from etch pits, previously formed from dislocation defects, were mainly responsible for the overall dissolution rate.

Based on these previous studies, one can assume that the likely mechanism controlling mica dissolution at acidic pH (in the absence of oxalate) is the retreat of the sheet edge parallel to the basal cleavage surface, resulting in an almost inert basal surface during dissolution. From the two types of mica surface, the basal (001) and the edge (lateral) (hk0), the latter is dominantly involved. However, it appears that at high temperature and pH and in presence of organic acid the formation of etch pits contributes to dissolution at the basal surface (McMaster et al., 2008; Haward et al., 2011; Kurganskaya et al., 2012; Pachana et al., 2012), in contrast to the absence of etch pits formation at ambient temperature (10-35°C) and acidic pH (with inorganic acid in solution) (McMaster et al., 2008; Haward et al., 2011). Then it still remains unclear whether the formation of etch pits at basal surface during mica dissolution at acid pH could intervene in the overall reaction.

Given this lack of knowledge, the motivation of this study was to deal with these two issues. With this aim, I have taken the advantages that offer the use of flow-through experiments for powder samples and the use of advance microscopic techniques to explore the reacted surfaces. This full approach complements experimental data from aqueous chemistry and surface/solution interface, providing a suitable quantification of the dissolution rates and an exhaustive characterization of the reaction mechanisms.

1.2 Objectives

With the aim at the enhancement of the understanding of the reactivity of 2:1 phyllosilicates the main goal of this Thesis was to investigate dissolution of smectite and two mica (biotite and phlogopite) in acidic pH and low temperature conditions. To achieve this goal the specific objectives to accomplish were:

1. Obtainment of a rate law that accounts for the dependence of smectite dissolution rate on the solution saturation state at acidic pH and room temperature. The smectite used in this study was montmorillonite, a dioctahedral smectite.

2. Understanding of the driving mechanisms of trioctahedral mica (biotite and phlogopite) dissolution in the absence and presence of organic acids, at acidic pH and temperature range from 11 to 100 °C by means of *in-situ* and *ex-situ* measurements at micro- and nano-scale.

3. Derivation of kinetic information from the topographic measurements of the mica (001) basal surface to interrelate macro and microscopic data sets.

The dissolution experiments have been performed at two levels. The macroscopic level to study the dissolution of K-montmorillonite using flow-through experiments and at the microscopic level to deal with the dissolution of biotite and phlogopite by carrying out micro-topographic measurements using high-resolution optical microscopy techniques (LCM-DIM, VSI-PSI and AFM).

1.3 Thesis outline

The thesis is composed of five main chapters including Introduction (***Chapter 1***) and Conclusions (***Chapter 5***). ***Chapter 2*** describes the methodology and experimental setup. ***Chapter 3*** deals with the kinetics of the smectite dissolution. ***Chapter 4*** is devoted to study the reactivity of mica sufaces in dissolution experiments in the absence and presence of oxalic acid. Finally, References (***Chapter 6***) and three appendices are provided. ***Appendix I*** includes methodology for smectite extraction and saturation, analytical techniques to determine solution composition and thermodynamic and adsorption data used in the reactive transport modeling. ***Appendix II*** shows data from biotite dissolution in batch experiments and VSI/PSI and LCM-DIM support images. ***Appendix III*** provides Labview script specifications used to perform the measurements and produced representative output images.

2 MATERIALS AND METHODS

This chapter describes the characterization of the three phyllosilicate samples (K-montmorillonite, biotite and phlogopite) used in this study, the experimental methodology to study the dissolution reactions by means of flow-through and batch experiments, and the calculations used to obtain dissolution rates to derive (1) the smectite dissolution rate law as a function of distance to equilibrium, expressed as Gibbs free energy, (2) pH and temperature dependence of biotite dissolution rate and (3) biotite and phlogopite dissolution rates.

2.1 Sample characterization

2.1.1 Smectite

The dioctahedral smectite used in this study was extracted from the La Serrata-Cortijo de Archidona bentonite deposit located at Cabo de Gata (Almeria, SE Spain). This bentonite is used as reference for the Spanish concept of nuclear waste repository and was already extensively characterized during the FEBEX (Full-Scale Engineered Barriers Experiments in Crystalline Host Rock) project (Huertas et al., 2000). Leone et al. (1983) and Caballero et al. (2005)[19] showed that it formed by hydrothermal alteration of volcanic tuff and is composed of approximately 92% montmorillonite and minor amounts (8 %) of accessory minerals (quartz, feldspars, micas, calcite and amphibole) and volcanic glass.

The flow-through experiments were performed using the < 4 μm size fraction, which was composed of nearly 100 % montmorillonite (Rozalén et al., 2008). This fraction was collected by repeated sedimentation-suspension in ultrapure water and then saturated in K^+ by dispersion in 0.5 M KCl solution. Details of the procedure are given in Appendix I. Powder X-ray diffraction (XRD) of the resulting K-smectite showed the sample consisted of dioctahedral smectite (K-montmorillonite) and no accessory minerals were identified (data not showed). No accessory/companying minerals were observed by SEM or TEM. The structural formula derived by analytical electron microscope (AEM) (based on half unit cell) analysis of the K- montmorillonite was:

$$K_{0.30}\ Ca_{0.02}(Al_{1.45}\ Fe^{3+}_{0.18}\ Mg_{0.44})\ (Si_{3.91}\ Al_{0.09})\ O_{10}(OH)_2$$

Some of the K-montmorillonite sample was pretreated to reduce the effect of the initial dissolution process and reach steady-state conditions faster, trying to avoid the changes

in the dissolution properties (Rozalén et al., 2008). The pretreatment consisted of placing ~2.5 g of sample in polyethylene bottles with 250 mL of 0.01 M KNO_3 solutions at pH 3 or 4, fixed using suprapure HNO_3, for three months at ambient temperature. During this period the bottles were shaken periodically. Thereafter the mixtures were centrifuged, the solid recovered and then dried at 40 °C for 48 hours. The smectite was ground to break up the mineral aggregates and stored to be used in flow-through experiments (Table 2.1).

The specific surface areas of the raw and pretreated K-montmorillonite samples were measured by the BET method (Brunauer, Emmett and Teller-BET) (Brunauer et al., 1938) with a Beckman-Coulter SA3100 surface area analyzer using 5-point N_2 adsorption isotherms. Sample degassing with nitrogen lasted for 2 h at 137 °C. The specific surface area was 82 $m^2\ g^{-1}$ for the raw sample and 91 and 93 $m^2\ g^{-1}$ for the pretreated samples at pH 3 and pH 4, respectively. Given the usual 10 % error in the BET analysis, it appears that the pretreatment slightly modifies the specific surface area of the pretreated sample.

2.1.2 Mica

The biotite and phlogopite samples were from Bancroft and Templeton (Ontario, Canada), respectively, and purchased from Ward's Natural Science Establishment. The supplied samples were centimetre-size specimens. The respective chemical compositions were determined by AEM and, assuming that total iron was Fe^{2+}, the structural formulas were calculated to be:

biotite: $K_{0.97}(Mg_{1.40}Fe_{1.29}Al_{0.04}Ti_{0.09}Mn_{0.09})(Al_{0.97}Si_{3.03})O_{10}(OH)_2$

phlogopite: $K_{0.93}(Mg_{2.63}Fe_{0.15}Al_{0.16})(Al_{1.03}Si_{2.97})O_{10}(OH)_2$

The resulting biotite stoichiometry was consistent with that reported by Turpault and Trotignon (1994) and Samson et al. (2005). Biotite flakes with surfaces of ~ 2 × 8 mm^2 and between 0.08 and 0.15 mm in thickness were used in the flow-through experiments to monitor the topographic variation on the (001) cleavage surfaces by LCM-DIM. On the other side single biotite and phlogopite fragments with a cleaved (001) surface of approximately 100 mm^2 and thickness of 0.08-0.15 mm were used for VSI/PSI observation while sample flakes of 0.5 × 0.5 mm^2 were used to perform AFM experiments.

The specific surface are of the biotite fragments of 0.8 to 2 mm^2 was measured by the BET method using 5-point N_2 adsorption isotherms. Fragment degassing with nitrogen lasted for 2 h at 137 °C. The specific surface area was 0.42 $m^2\ g^{-1}$.

2.2 Experimental setup

2.2.1 K-montmorillonite dissolution experiments

The K- montmorillonite dissolution experiments were performed in stirred flow-through cells fully immersed in a thermostatic water-bath held at a constant temperature of 25 ± 1 °C (Figure 2.1). The flow rate was controlled with a peristaltic pump that injects the input solution into the bottom chamber of the cell, where the solution is homogenized by a magnetic bar before reaching the upper chamber. The solid sample was confined within the upper chamber by membrane filters (a 5 μm nylon mesh plus a 1.2 μm Durapore membrane at the bottom, and a 0.45 μm Durapore membrane at the top). The total volume of the cell was 46 mL. This type of experiments allowed the control and variation of the experimental conditions (flow rate, initial powder mass and Si and Al input concentrations), facilitating the calculation of mineral dissolution rates under fixed saturation state conditions (Cama et al., 2000).

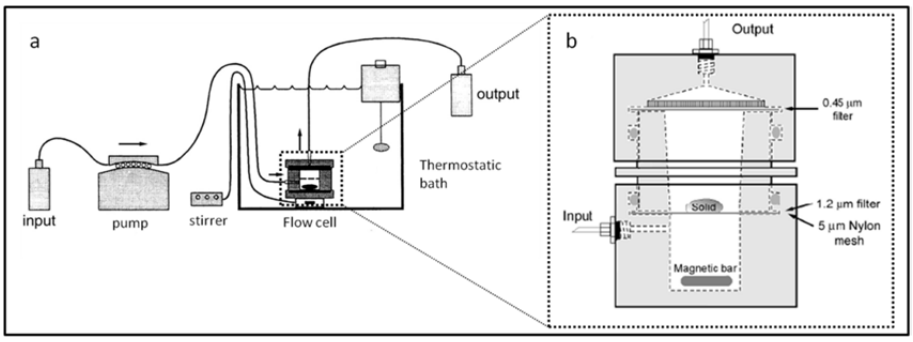

Figure 2.1. Schematic representations of (a) the experimental setup and (b) flow-through reactor (modified from Rozalén et al., 2009 [2s]).

A total of 36 flow-through experiments were performed with the K-montmorillonite. Table 2.1 shows the experimental conditions. Most experiments were finished when steady state was reached. In a few cases, the experiments were stopped earlier for the onset of technical problems (e.g., cell opening). Steady state was achieved when the output Si concentration remained approximately constant and differed by less than 6% between consecutive samples (at least 100 h). In each experiment the flow rate and the input solution pH were held constant until steady state was achieved. Experiments lasted between 1340 h to 2940 h, depending on the experimental conditions.

Table 2.1. Initial experimental conditions of the smectite flow-through dissolution experiments.

Experiment[†]	**initial mass (g)**	**flow rate (mL min^{-1})**	**pH$_{inp}$**	**C$_{Si,inp}$ (μM)**	**C$_{Al,inp}$ (μM)**	**duration (h)**
			pH ≈ 2			
Sm-SL1-2	0.0464	0.072	2.00	0	0	1411
Sm-SL2-2a	0.0918	0.025	2.05	0	0	2372
Sm-SL2-2b	0.0919	0.073	2.01	0	0	1431
Sm-SL10-2a	0.4602	0.024	2.02	12	0	2372
Sm-SL10-2b	0.4605	0.026	2.06	35	0	2372
Sm-SL10-2c	0.4605	0.024	2.03	113	0	2371
Sm-SL10-2d	0.4601	0.027	2.04	376	0	2371
			pH ≈ 3			
Sm-SL2-3	0.0919	0.022	2.99	0	0	1909
Sm-SL10-3	0.4598	0.020	2.98	0	0	1909
Sm-Sl20-3	0.9210	0.021	3.00	0	0	1909
Sm-SL2-3b	0.0923	0.022	2.95	103	39	2945
Sm-SL10-3b	0.4603	0.020	2.96	106	34	2945
Sm-SL20-3b	0.9200	0.022	2.98	107	42	2945
Sm-SL10-3c	0.4606	0.023	3.16	34	37	2668
Sm-SL20-3c	0.9203	0.024	3.15	34	36	2518
Sm-SL10-3Al	0.4601	0.021	3.08	0	37	2781
Sm-SL10-3d*	0.4614	0.023	2.97	209	11	2326
Sm-SL10-3e*	0.4606	0.023	3.10	421	9	2326
Sm-SL10-3f*	0.4602	0.022	3.08	893	0	2917
Sm-SL10-3ba*	0.4600	0.021	3.03	106	40	2942
Sm-SL10-3h*	0.4602	0.007	3.03	105	38	2925
Sm-SL10-3i*	0.4603	0.011	3.03	104	41	2925
Sm-SL2-3d*	0.0920	0.070	3.03	0	0	1337
			pH ≈ 4			
Sm-SL2-4	0.0918	0.021	3.91	0	0	1909
Sm-SL10-4	0.4611	0.024	3.94	0	0	1861
Sm-SL20-4	0.9214	0.023	3.95	0	0	1909
Sm-SL10-4b	0.4601	0.024	4.10	104	37	2945
Sm-SL20-4b	0.9198	0.023	4.08	105	37	2945
Sm-SL2-4c	0.0920	0.022	4.08	37	36	2783
Sm-SL10-4c	0.4600	0.022	4.09	36	35	2764
Sm-SL20-4c	0.9202	0.023	4.15	36	51	2666
Sm-SL10-4Al	0.4600	0.023	4.01	0	37	2684
Sm-SL10-4e*	0.4611	0.024	3.98	202	11	2036
Sm-SL10-4ba*	0.4618	0.021	3.99	108	41	2924
Sm-SL10-4i*	0.4606	0.006	4.03	108	43	2924
Sm-SL10-4l*	0.4604	0.011	4.02	104	40	2924

[†]The labels of the experiment indicate mineral name (Sm for smectite), solid/liquid ratio (SL 2, 10 and 20) and pH (2, 3 and 4). Labels with a different letter indicate experiments with same pH and initial mass but different flow rate or input Si and Al concentration.
*preconditioned solid

In all experiments, 0.01 mol L^{-1} KNO_3 was used as a background electrolyte, and HNO_3 was used to fix the input solution pH. Acetic acid/acetate was used to buffer the pH at 4. In some experiments, Si and Al were added to the input solutions. All chemicals were suprapur or reagent grade. Different solid/liquid ratios (SL= 2, 10 and 20) and flow rates were used in the experiments (Table 2.1) to obtain the dissolution rates at different solution saturation state (variation in far-from-equilibrium to near equilibrium conditions).

Output solutions were collected every one or two days and analyzed for pH and total dissolved Si, Al and Mg. After reaction, the pH of the output solution was immediately measured using Crison combination electrodes, standardized against pH 4 and 7 buffer solutions. The reported accuracy was of ± 0.02 pH units. The output solutions of experiments at pH 4 were further acidified to pH 3 with ultrapure HNO_3 to prevent precipitation of Al or Fe-bearing phases during storage.

2.2.2 Biotite dissolution in flow-through experiments

Biotite flakes were placed in a flow-through cell to monitor the variation in the (001) cleavage surface morphology using the LCM-DIM advanced optical system (Figure 2.2 a; Table 2.2). A custom-made Teflon flow-through cell consisted of a rectangular prism with a volume of 0.08 cm^3 and a fissure on one side (Figure 2.2 d). The cell was mounted inside a copper sample stage which completely surrounds the cell, leaving an observation area (7 mm in diameter) at the bottom side (Figure 2.2 c,d). To precisely control the temperature of the sample stage a curve-matched thermistor and two Peltier elements were employed. A PR-59 (Supercool ®) temperature controller PC-interfaced through a serial connection by means of a Labview ® driver was also used. Water jackets with circulating water were placed on top of the Peltier hot sides to increase the cooling capacity for set points below room temperature. Thermal silicon grease was employed to minimize thermal contact resistance. The precision of the temperature control was ± 0.5 °C (Van Driessche et al., 2009).

Biotite flakes reacted with 0.1 mol L^{-1} HNO_3 (~ pH 1) or 0.1 mol L^{-1} oxalic acid and 0.01 mol L^{-1} $NaNO_3$ solutions prepared from ultrapure grade chemicals (Table 2.2).

To observe the dissolving basal surface the flakes were fixed parallel to the (001) surface on the bottom of the fissure of the flow-through cell by a silicone adhesive. A small canal on each side of the cell (Figure 2.2c,d) allowed circulation of the reacting solution at a constant flow rate (0.01-0.07 mL min^{-1}), yielding a residence time from approximately 1 to 8 min. The Teflon flow-through cell was carefully sealed with a cover glass glued with high

vacuum grease (Dow Corning ®). The experiments were conducted over a wide temperature range (11.5 - 70°C). To increase the thermal stability in the experiments at T ≥ 40°C, the reacting solutions were pre-heated in a thermostatic bath (Figure 2.2b). Additionally, the input solutions were degasified with a vacuum pump for ~ 2 h to reduce bubble formation during the high temperature runs (T ≥ 40°C).

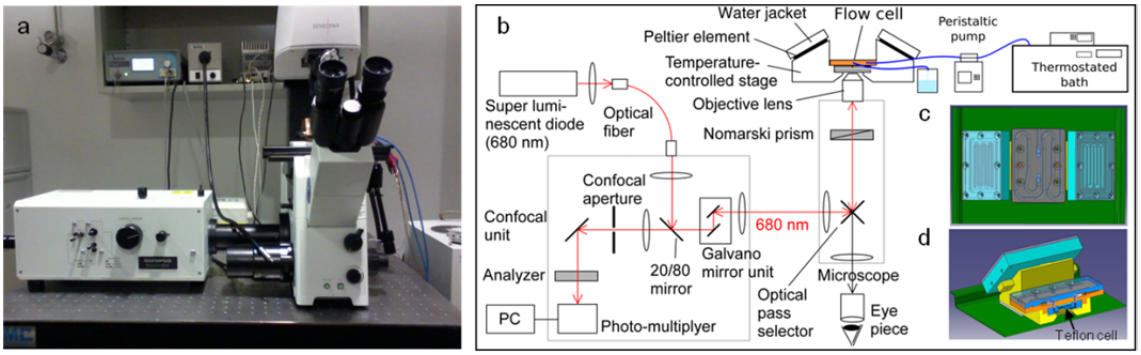

Figure 2.2. Image (a) and schematic representation (b) of the experimental setup: the Laser confocal differential interference contrast microscopy equipment; top view (c), and a cross-sectional view (d) of the temperature-controlled observation flow cell.

Table 2.2. Initial experimental conditions of the biotite LCM-DIM experiments.

Experiment[†]	T	flow rate	oxalic acid	HNO_3	$NaNO_3$	duration
	(°C)	(mL min^{-1})	(mol L^{-1})	(mol L^{-1})	(mol L^{-1})	(h)
B11.5-1-1	11.5	0.07	-	0.1	0.01	142
B11.5-1-2	11.5	0.07	-	0.1	0.01	90
B25-1-3	25	0.07	-	0.1	0.01	31
B25-1-4	25	0.07	-	0.1	0.01	18
B40-1-1	40	0.07	-	0.1	0.01	4
B40-1-1c	40	0.07	-	0.1	0.01	4
B50-1-1	50	0.01	-	0.1	0.01	98
B50-1-2	50	0.01	-	0.1	0.01	25
B70-1-3	70	0.07	-	0.1	0.01	5
B70-1-3b	70	0.07	-	0.1	0.01	2
B70-1-5b	70	0.07	-	0.1	0.01	2
B25-ox0.1-1	25	0.07	0.1	-	0.01	100
B50-ox0.1-1	50	0.07	0.1	-	0.01	18

[†] The labels of the experiments indicate mineral (e.g., B for biotite), temperature, pH and number (and additional letter in some cases) of the experiment.

Experiments lasted from 2 hours to 6 days according to the experimental conditions (i.e., the lowest the temperature the longer the experiment span due to the slower biotite

dissolution kinetics). Images of the (001) cleavage surface were taken every 20 s to 15 min with a time of capture of 9.6 s. Replicas were performed for each experiment.

2.2.3 Mica dissolution in batch experiments

Batch experiments placed into a thermostatic water-bath or an heater held at constant temperature were used to study mica dissolution in the absence and presence of oxalic acid over a temperature range of 25-100 °C (Figure 2.3a; Table 2.3 and Table 2.4).

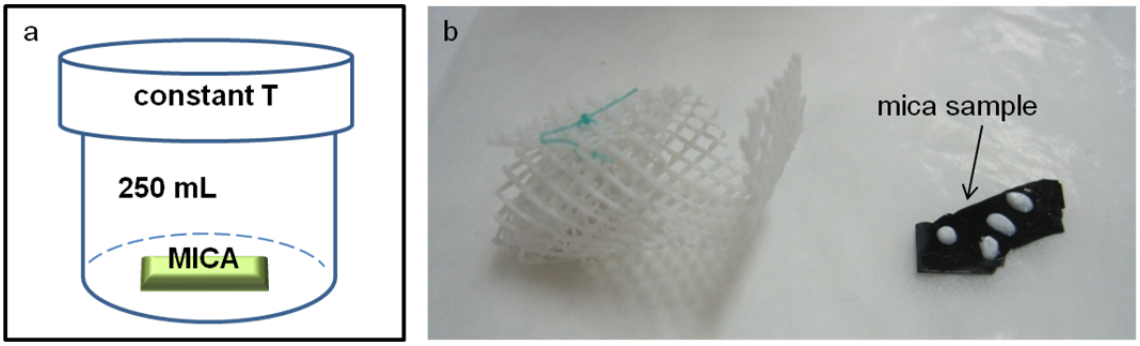

Figure 2.3. Dissolution batch experiments: (a) representation of a batch experiment and (b) image of mesh to hold biotite samples. The (001) surface was partially covered with silicon masks.

Single biotite and phlogopite fragments were placed in polyethylene bottles (or in high pressure reactors at high temperature) that were filled with 250 mL of 0.1-0.001 mol L^{-1} HNO_3 (pH 1-3) or 0.1-0.01 mol L^{-1} oxalic acid (pH 1.4-2.2) solutions. In every solution 0.01 mol L^{-1} $NaNO_3$ was used as background electrolyte. During the experiments, the solution was changed every 1 to 14 days, depending on the experimental conditions, to keep the solution undersaturated with respect to biotite and phlogopite.

Several small spots on some unreacted biotite basal surface were covered with Loctite Superflex clear or white RTV or Permatex High Temperature red RTV silicone, high-temperature commercial silicone polymers. The covered spots did not react and could be used as reference for the height measurements by interferometry (Figure 2.3b). After quenching the experiments, the rubber masks were gently removed, the retrieved reacted fragments were immediately dried and *ex situ* interferometric (VSI and/or PSI) measurements of the topography of the reacted biotite (001) surfaces were performed. Height difference between preserved unreacted and reacted (001) surfaces was measured for the estimation of dissolution rate.

Table 2.3. Initial experimental conditions of the biotite and phlogopite VSI/PSI experiments performed with HNO_3.

Experiment†	T	mass	HNO_3	$NaNO_3$	duration
	(°C)	(g)	(mol L^{-1})		(h)
B13_25_1	25	0.0801	0.1	0.01	1194
B10_40_1	40	0.0505	0.1	0.01	504
B8_50_1	50	0.0532	0.1	0.01	183
B30_70_1	70	0.0277	0.1	0.01	284
B59_80_1	80	-	0.1	0.01	96
B12_25_2	25	0.0647	0.01	0.01	2087
B21_40_2	40	0.0740	0.01	0.01	670
B25_40_2	40	0.0266	0.01	0.01	1026
B6_50_2	50	0.0327	0.01	0.01	560
B26_50_2	50	0.0766	0.01	0.01	496
B29_70_2	70	0.0350	0.01	0.01	458
B66_70_2	70	0.0305	0.01	0.01	335
B23_25_3	25	0.0289	0.001	0.01	2693
B24_40_3	40	0.0231	0.001	0.01	577
B47_70_3	70	0.0700	0.001	0.01	192
Phg10_40_1	40	0.1007	0.1	0.01	1056
Phg31_70_1	70	0.0302	0.1	0.01	168
Phg36_70_2	70	0.0228	0.01	0.01	144
HPhg2_100_1	100	-	0.1	0.01	24
HPhg3_100_1	100	-	0.1	0.01	96
HPhg10_100_2	100	-	0.01	0.01	24

† The labels of the experiment indicate mineral (B = biotite, Phg = phlogopite), number of sample (number and additional letter in some cases), temperature and pH. H before Phg stands for high temperature experiment.

Table 2.4. Initial experimental conditions of the biotite and phlogopite VSI/PSI experiments performed with oxalic acid.

Experiment	T	mass	oxalic acid	$NaNO_3$	duration
	(°C)	(g)	(mol L^{-1})		(h)
B37b_25_0.1	25	0.0782	0.1	0.01	212
B56_25_0.1	25	0.074*	0.1	0.01	311
B58_40_0.1	40	0.076*	0.1	0.01	121
B65_40_0.1	40	0.069*	0.1	0.01	72
B38b_40_0.1	40	0.0708	0.1	0.01	191
B53_50_0.1	50	0.0351	0.1	0.01	72
B39b_50_0.1	50	0.0512	0.1	0.01	191
B54_70_0.1	70	0.0573	0.1	0.01	72
B40b_70_0.1	70	0.0519	0.1	0.01	192
B44_25_0.01	25	0.0631	0.01	0.01	407
B48_25_0.01	25	0.0170	0.01	0.01	212
B71_25_0.01	25	0.0649	0.01	0.01	72
B49_40_0.01	40	0.0170	0.01	0.01	191
B57_40_0.01	40	0.046*	0.01	0.01	121
B70_40_0.01	40	0.0560	0.01	0.01	72
B51_50_0.01	50	0.0682	0.01	0.01	72
B50_50_0.01	50	0.0354	0.01	0.01	191
B43b_70_0.01	70	0.0421	0.01	0.01	192
B52_70_0.01	70	0.0545	0.01	0.01	72
Phg2_70_0.1	70	0.0548	0.1	0.01	168
Phg2_80_0.1	80	-	0.1	0.01	48
Phg1_70_0.01	70	0.0239	0.01	0.01	168
Phg1_80_0.01	80	-	0.01	0.01	48

† The labels of the experiment indicate mineral (B = biotite, Phg = phlogopite), number of sample, temperature and oxalic acid concentration (0.01-0.1 M).

*final mass

Two similar batch experiments were performed to examine the biotite (001) surface using AFM. Two sample flakes were placed in the 250 mL polyethylene bottles with inorganic (0.01 $NaNO_3$ mol L^{-1} + 0.1 mol L^{-1} HNO_3) and organic acid (0.01 $NaNO_3$ mol L^{-1} + 0.1 mol L^{-1} oxalic acid) solution respectively at 70 °C during 72 h. The surfaces were scanned *ex situ* after sample retrieve.

2.3 Solution analysis

Input and output solutions from the K-montmorillonite and biotite flow-through and batch experiments were analysed for pH and Si, Al, Mg, K and Fe (samples structural cations) concentrations.

Silica concentration was determined by colorimetry, using the molybdate blue method (Grasshoff et al., 2009) with a Visible/UV spectrophotometer (Appendix I). Ammonium molybdate added to solution forms with Si a yellow complex in acidic ambient that turns blue when reduced. The maximum of absorption is measured at 825 nm in a UV/Visible Perkin Elmer Lambda 25 spectrometer. The detection limit is 5 ppb and the uncertainty is less than 3 %. Aluminium concentration was measured by spectrofluorimetry using lumogallion as complexing agent (Howard et al., 1986) (Appendix I). An electromagnetic wave with wavelength λ_{ex} excites the fluorescent Al-lumogallion complex that relaxing emits at a higher wavelength λ_{em}. A FluoDia T70 High Temperature Fluorescence Microplate Reader was used, being the excitation and emission wavelengths 486 and 550 nm respectively. The detection limit was 2 ppb and the uncertainty was less than 5%. Mg and K concentrations were determined by ion chromatography using a Methrohm 883 Basic IC plus with a Metrosep C3 column. The detection limit and the uncertainty for Mg and K analysis were 0.5 ppb and 3 %, respectively. The Fe concentration was determined by colorimetry, measuring the absorption of the red complex that iron (II) form with 1,10–phenanthroline (Pyenson and Tracy, 1945; Lazic et al., 2010) (Appendix I). The detection limit was 0.2 ppm and the uncertainty was less than 3%.

In presence of oxalic acid, colorimetry could not be used to measure the total Si and Al concentrations for the interferences between organic species. For this reason, the total Si and Al concentrations were analyzed by inductive coupled plasma-atomic emission spectrometry (ICP-AES; Thermo Jarrel-Ash with CID detector and a Perkin Elmer Optima 3200 RL). The detection limits for Si and Al were 4.5×10^{-7} mol L^{-1} and 1.3×10^{-6} mol L^{-1}, respectively. The accuracy of the measurement was estimated to be around 3%.

2.4 Microscopy techniques

2.4.1 Laser Confocal Microscopy with Differential Interference Microscopy

The dissolving biotite basal surface was observed by LCM-DIM, which is a combination of two microscopy techniques: a confocal system (FV300, Olympus) attached to an inverted optical microscope (IX70, Olympus) and a Nomarski prism introduced into the optical path (Figure 2.2). A partially coherent super luminescent diode (Amonics Ltd., model ASLD68-050-B-FA: 680 nm) is used to eliminate diffraction noise. This combination provides high contrast and high resolution in the vertical plane (z ~1 nm) of the crystal surface, and the x-y plane resolution is ~1380 nm for a 10× objective lens (LUCplan FLN 10x, Olympus) (Van Driessche et al., 2008). The surface is scanned line-by-line deflecting the laser beam in the x-y plane by galvanic mirrors. The light reflected at the crystal surface/solution interface is detected by a photomultiplier tube (PMT). Although LCM-DIM cannot give topographical quantitative information, it allows following *in situ* a dissolution process over a wide field of view at high vertical and lateral resolution.

2.4.2 Vertical Scanning and Phase Shifting Interferometry

Variation in the topography of the biotite (001) surface was measured *ex situ* using a vertical scanning interferometer (Zemapper; Zemetrics, Tucson, AZ) equipped with 2048 × 2048 pixel CCD camera and 10× and 100× Mirau objectives (Figure 2.4). In the case of unreacted surfaces, very smooth surfaces and fragments immersed in fluid, Phase Shifting Interferometry (PSI) was performed using a Linnik objective (Sensofar, version 1).

Interferometric optical systems use light interference as operational physical principle. The objectives use an internal beam splitter to create two beams, one reflected by a reference mirror and the other by the sample surface. These two beams will differ in path length (optical path difference) as a function of the distance to the sample surface (surface height) (Lüttge and Arvidson, 2010). When recombined they give an interference pattern creating a series of fringes whose distribution is recorded by the high resolution CCD camera that measures the resultant light intensity over multiple image points. From measured intensity variation, by means an algorithm, relative heights are calculated.

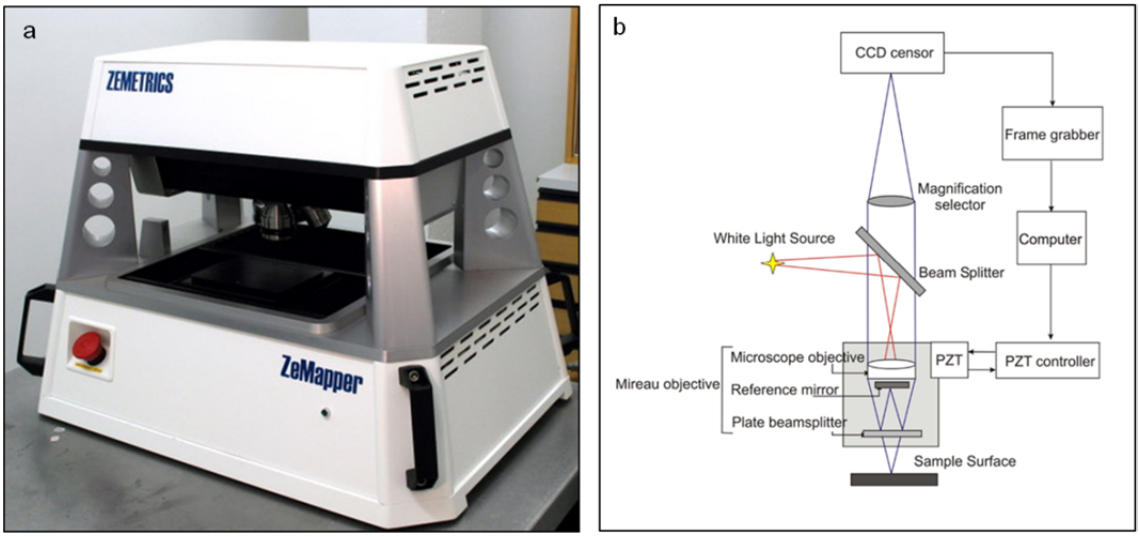

Figure 2.4. Vertical scanning interferometry: a) photograph of the Zemapper interferometer and (b) schematic of the vertical scanning interferometer.

2.4.3 Atomic Force Microscopy

AFM inspection of the biotite and phlogopite (001) surface was carried out using a Nanotec microscopy (Electronica, Madrid, Spain). Atomic force microscopy uses a laser beam deflection system where a laser is reflected from the back of a reflective lever (cantilever) towards a sensitive detector. The cantilever tip scans the sample surface and the resultant deflection of the cantilever, proportional to the force between tip and sample, is measured (Figure 2.5). Contact mode was used to scan the cleaved surfaces.

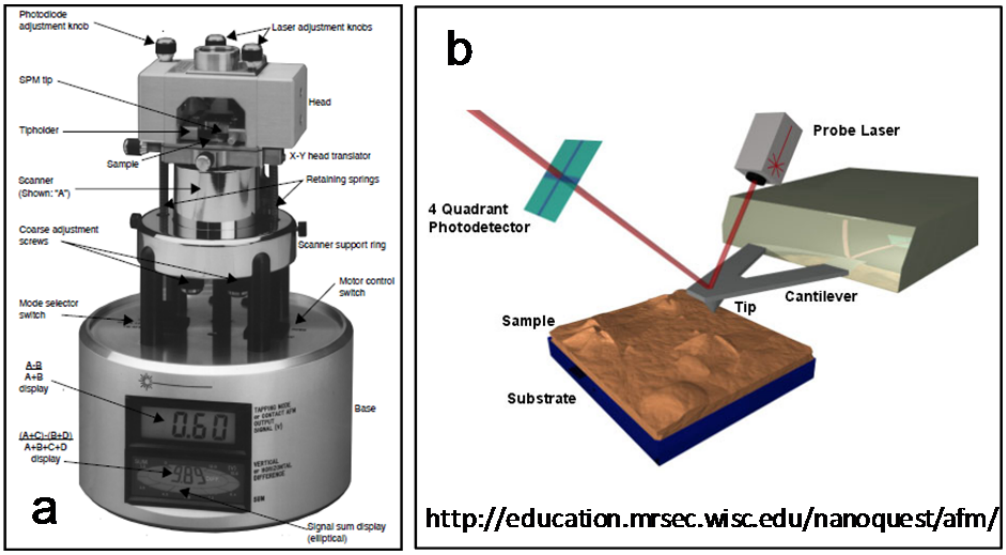

Figure 2.5. Atomic force microscope: (a) photograph of the AFM microscope (from Multimode SPM Instruction VEECO manual) and (b) schematic of the AFM functioning.

2.5 Calculations

2.5.1 K-montmorillonite dissolution rate

The steady-state dissolution rate, $R_{diss,j}$ (mol m^{-2} s^{-1}), in a well-mixed flow-through reactor can be calculated based on a mass balance equation from the expression (Cama et al., 2000; Rozalén et al., 2009b):

$$R_{diss,j} = \frac{1}{\nu_j}\frac{q}{S \cdot m_f}(C_{j,out} - C_{j,inp}) \qquad 2.1$$

where ν_j is the stoichiometric coefficient of component *j* in the dissolution reaction, *q* stands for the flow rate, *S* is the specific surface area, m_f is the final sample mass, and $C_{j,out}$ and $C_{j,in}$ correspond to the concentrations of component *j* in the output and input solutions, respectively.

Variation in the output concentrations of Si, Al and Mg with time allows estimation of dissolved sample mass according to:

$$m_f = m_0 - \left(\sum_{t_0}^{t} c_{j,t} \cdot V_{out} \cdot \frac{P_m}{\nu_j} \right) \qquad 2.2$$

where m_f and m_0 are final and initial mass respectively, $c_{j,t}$ is the concentration at time *t* of component *j* (Si, Al or Mg), V_{out} is the volume of output solution between two consecutive samples, and P_m *is* the K-montmorillonite molar mass. In the present study, the dissolution rate, $R_{diss,j}$, was not normalized to the specific surface area as expressed in Eq. (2.1), but calculated in mol g^{-1} s^{-1} as:

$$R_{diss,j} = -\frac{1}{\nu_j}\frac{q}{m_f}(C_{j,out} - C_{j,inp}) \qquad 2.3$$

This decision was taken given the still arguable suitability to normalize smectite dissolution rates using the BET specific surface area, edge surface area (ESA) or geometric area as representative proxy of the "reactive" surface area (Bosbach et al., 2000; White and Brantley, 2003; Metz et al., 2005b; Hodson, 2006a; Hodson, 2006b).

The propagated error (ΔP) associated with the calculated dissolution rate was estimated according to the Gaussian error propagation method (Barrante, 1974; Cama et al., 2000).

2.5.2 Solution saturation state (Gibbs free energy, ΔG_r)

The degree of saturation of the solutions with respect to K-montmorillonite and biotite dissolution was calculated in terms of the Gibbs energy of reaction, ΔG_r (kcal mol^{-1}):

$$\Delta G_r = RT \ln\left(\frac{IAP}{K_{eq}}\right) \qquad 2.4$$

where *R* is the gas constant, *T* is the absolute temperature, and *IAP* and K_{eq} are actual and equilibrium ion activity products of the solution, respectively.

The IAP was calculated as:

$$IAP = \prod_j a_j^{\nu_j} = \prod_j \gamma_j^{\nu_j} \cdot C_j^{\nu_j} \qquad 2.5$$

where a_j, γ_j and C_j are the activity, the activity coefficient and the concentration of component *j*, respectively, and ν_j is the stoichiometric coefficient of component *j* in the dissolution reaction.

Activity coefficients were calculated using the EQ3NR geochemical code (Wolery, 1992a, b) and the Lawrence Livermore National Laboratory thermodynamic database (data0.cmp in the EQ3/6 package). Aqueous speciation between Al, Mg, Fe, Na, K and the oxalate at 25 °C was considered in the calculations using the reactions and associated K_{eq} values listed in Table 2.5. Since the Fe concentration in the flow-through smectite experiments was always below the detection limit, in order to calculate *IAP*, the output Fe concentration was set to be the stoichiometric one at pH 2 and 3, whereas at pH 4 the equilibrium concentration with $Fe(OH)_3$ was assumed (Rozalén et al., 2009b). It is important to note that the contribution of the Fe concentration to the IAP value is very low with respect to that of Si and Al. Therefore its weight on ΔG_r calculation is exiguous. The uncertainty associated to the calculated IAP value is less than 38%.

Table 2.5. Equilibrium constants for the speciation of aqueous Al, Mg, Fe, Na, K and oxalate at 25 °C[28].

Reaction					log (K_{eq})	Reference
Al^{3+}	+	$C_2O_4^{2-}$	=	$Al(C_2O_4)^+$	6.1	Jaber et al. 1977
Al^{3+}	+	$2\ C_2O_4^{2-}$	=	$Al(C_2O_4)_2^-$	11.1	Jaber et al. 1977
Al^{3+}	+	$3\ C_2O_4^{2-}$	=	$Al(C_2O_4)_3^{3-}$	15	Jaber et al. 1977
Fe^{3+}	+	$C_2O_4^{2-}$	=	$Al(C_2O_4)^+$	8.8	Cheah et al. 2003
Fe^{3+}	+	$2\ C_2O_4^{2-}$	=	$Fe(C_2O_4)_2^-$	15.44	Cheah et al. 2003
Fe^{3+}	+	$3\ C_2O_4^{2-}$	=	$Fe(C_2O_4)_3^{3-}$	19.83	Cheah et al. 2003
Mg^{2+}	+	$C_2O_4^{2-}$	=	MgC_2O_4	3.43	Martell and Smith 1977
K^+	+	$C_2O_4^{2-}$	=	$KC_2O_4^-$	-0.8	Prapaipong et al. 1999
Na^+	+	$C_2O_4^{2-}$	=	$NaC_2O_4^-$	-0.86	Prapaipong et al. 1999

The equilibrium constant for the dissolution reaction of the K-montmorillonite at 25 °C was computed following Vieillard (2000) according to the overall K-montmorillonite dissolution reaction expressed as:

$$K_{0.30}Ca_{0.02}(Al_{1.45}Fe^{3+}_{0.18}Mg_{0.44})(Si_{3.91}Al_{0.09})O_{10}(OH)_2 + 6.18H^+ \rightarrow$$
$$\rightarrow 0.30K^+ + 0.02Ca^{2+} + 1.54Al^{3+} + 0.18Fe^{3+} + 0.44Mg^{2+} + 3.91SiO_2 + 4.09H_2O \quad (2.6)$$

log K_{eq} at 25 °C and 1 atm. was estimated to be 5.30. The propagated error for ΔG_r was ± 0.23.

2.5.3 Biotite dissolution rates

In the LCM-DIM flow-through experiments, the biotite dissolution rates were obtained from the topography measurements. A retreat rate, R_r (μm s^{-1}), at a given location of the (001) basal surface was computed as:

$$R_r = \frac{\Delta L}{(t_2 - t_1)} \quad (2.7)$$

where ΔL is the change in the horizontal surface length as measured over the period between t_1 and t_2 (Cappelli et al., 2013).

In batch experiments, biotite dissolution rate, R_{diss} (mol g^{-1} s^{-1}), was calculated from VSI/PSI images by two methods depending on if HNO_3 or oxalic acid was used in the reacting solution. In the former case, using silicone mask small areas of unreacted biotite surface (reference surface) were preserved. From the change in surface height between the reacted

and the unreacted reference surface, Δh, of a selected surface region, dissolution rate was calculated by the following equation:

$$R_{diss} = \frac{\Delta h_i \cdot f_i}{\Delta t} \cdot \frac{1}{V_{mol}} \cdot S \qquad 2.8$$

where Δh_i is the height difference for an *i* surface point (image pixel), f_i is the *i* height frequency, V_{mol} is the biotite molar volume (140 cm^3 mol^{-1}), Δt is the reaction time and *S* is biotite specific BET surface area.

In order to quantify the vertical amplitude variation (z variation) for a homogenous distribution of etch pits formed on biotite surface in presence of oxalic acid, the root-mean-square roughness (R_q) is defined as:

$$R_q = \sqrt{\frac{1}{M \times N} \sum_{i=1}^{M} \quad \sum_{i=1}^{N} [\mathrm{z(i,j)}]^2} \qquad 2.9$$

where *M*×*N* is the extension of the inspected area in pixels. This parameter quantifies and weights the deviations of height of all data points, in a limited *M*×*N* area, from a *zero* plane.

Also, volume loss was calculated by subtracting the etched surface to a reference flat surface. The system-design platform LabView (Laboratory Virtual Instrument Engineering Workbench) was used to elaborate a script to measure the volume of each pit standing on a selected biotite (001) surface area. The moles of dissolved biotite are obtained dividing the total volume loss, V_{loss} (sum of all etch pits volume), by the biotite molar volume. $R_{diss,p}$ (mol g^{-1} s^{-1}) (where the subscript stands to pit) was then calculated by:

$$R_{diss,p} = \frac{V_{loss}}{V_{mol}} \cdot \frac{1}{A * \Delta t} \cdot S \qquad 2.10$$

where *A* is the selected area.

Biotite dissolution rate, R_j (mol g^{-1} s^{-1}), was also obtained by measuring the change in concentration of a component *j* in batch experiment solution during the entire stage of dissolution. When the change in concentration was linear with time, R_j was calculated using the expression:

$$R_j = -\frac{1}{\nu_i} \cdot \frac{(C_{i,out} - C_{i,inp})}{m_0} \cdot \frac{V}{dt} \qquad 2.11$$

where *V* is the volume of the batch experiment. The propagated error associated with the calculated dissolution rate (R_j) was estimated according to the Gaussian error propagation method (Barrante, 1974).

3 SMECTITE DISSOLUTION KINETICS

This chapter deals with the smectite dissolution kinetics, and in particular with the effect that the degree of saturation (ΔG_r) exerts on the K-montmorillonite dissolution rate. Dissolution rates were obtained in acid pH (2-4), at different solution saturation states and room temperature using stirred flow-through reactors.

The initial mass of K-montmorillonite, concentration of Al and Si in the input solution and the flow rate were varied among the experiments. The K-montmorillonite dissolution rates were obtained based on the release of Si (R_{Si}), Al (R_{Al}) and Mg (R_{Mg}) at steady state. The experimental conditions and results are given in (Table 3.1).

The steady-state dissolution rates obtained were used to establish a dissolution rate law that accounts for the dependence of the K-montmorillonite dissolution rate on the degree of saturation (ΔG_r). Based on the release of Si, Al and Mg, the congruency of the dissolution was examined to understand the mechanisms that intervene in the overall smectite dissolution reaction at acid pH.

Table 3.1 Experimental results of the smectite flow-through experiments at steady state.

Experiment	pH out	$C_{Si.out}$	$C_{Al.out}$	$C_{Mg.out}$	$\Delta C_{Al}/\Delta C_{Si}$	$\Delta C_{Mg}/\Delta C_{Si}$	R_{Si}	R_{Al}	R_{Mg}	ΔG_r	error R_{Si}	error R_{Al}	error R_{Mg}	error ΔG_r
		(μM)					(mol g^{-1} s^{-1})			(kcal mol^{-1})		(%)		(kcal mol^{-1})
pH ≈ 2														
Sm-SL1-2	2.00	3.34	1.28	1.50	0.38	0.45	1.17E-11	1.36E-11	3.71E-11	-38.59	5	5	5	0.23
Sm-SL2-2a	2.05	13.1	5.46	2.58	0.42	0.20	8.16E-12	8.61E-12	1.43E-11	-33.46	5	5	5	0.23
Sm-SL2-2b	2.01	6.72	2.27	1.67	0.34	0.25	1.22E-11	1.05E-11	2.24E-11	-36.20	5	5	6	0.23
Sm-SL10-2a	2.02	59.7	24.0	6.82	0.50	0.14	5.70E-12	7.21E-12	7.16E-12	-28.51	6	5	5	0.23
Sm-SL10-2b	2.06	84.0	21.8	6.83	0.45	0.14	6.17E-12	7.02E-12	7.18E-12	-27.45	8	5	5	0.23
Sm-SL10-2c	2.03	164	24.5	7.44	0.48	0.15	5.97E-12	7.34E-12	7.80E-12	-26.03	15	5	5	0.23
Sm-SL10-2d	2.04	410	22.9	6.60	0.66	0.19	4.55E-12	7.67E-12	7.75E-12	-23.93	56	5	5	0.23
pH ≈ 3														
Sm-SL2-3	2.99	4.10	1.94	0.56	0.47	0.14	2.14E-12	2.57E-12	2.50E-12	-29.43	5	5	5	0.23
Sm-SL10-3	2.98	23.1	7.51	3.29	0.32	0.14	2.16E-12	1.78E-12	2.73E-12	-23.63	12	8	8	0.23
Sm-Sl20-3	3.00	44.4	8.56	5.78	0.19	0.13	2.22E-12	1.09E-12	2.57E-12	-21.61	5	5	5	0.23
Sm-SL2-3b	2.95	106	39.7	0.41	0.21	0.14	1.55E-12	1.25E-12	1.90E-12	-19.59	180	212	5	0.23
Sm-SL10-3b	2.96	122	44.3	2.04	0.64	0.13	1.49E-12	2.40E-12	1.66E-12	-18.49	39	22	5	0.23
Sm-SL20-3b	2.98	135	45.3	6.78	0.12	0.25	1.41E-12	4.23E-13	3.09E-12	-17.71	24	70	5	0.23
Sm-SL10-3c	3.16	47.4	42.5	1.83	0.44	0.14	1.42E-12	1.57E-12	1.75E-12	-19.08	18	38	5	0.23
Sm-SL20-3c	3.15	57.5	45.2	2.62	0.38	0.11	1.31E-12	1.26E-12	1.30E-12	-18.51	12	25	5	0.23
Sm-SL10-3Al	3.08	14.9	41.7	2.00	0.31	0.13	1.48E-12	1.02E-12	1.66E-12	-22.42	5	53	5	0.23
Sm-SL10-3d	2.97	221	15.2	1.83	0.38	0.16	1.21E-12	1.16E-12	1.74E-12	-17.92	97	18	5	0.23
Sm-SL10-3e	3.10	432	14.5	1.49	0.47	0.13	1.19E-12	1.42E-12	1.40E-12	-15.54	197	14	5	0.23
Sm-SL10-3f	3.08	911	6.21	1.93	0.34	0.11	1.06E-12	1.62E-12	1.63E-12	-14.77	442	5	5	0.23
Sm-SL10-3ba	3.03	122	47.7	1.85	0.45	0.11	1.61E-12	1.82E-12	1.60E-12	-17.90	37	32	5	0.23
Sm-SL10-3h	3.03	147	51.1	5.20	0.31	0.12	1.37E-12	1.09E-12	1.52E-12	-17.00	18	20	5	0.23
Sm-SL10-3i	3.03	134	52.8	3.73	0.38	0.13	1.48E-12	1.44E-12	1.66E-12	-17.30	23	23	5	0.23
Sm-SL2-3d	3.03	2.48	0.99	0.54	0.40	0.22	4.11E-12	4.24E-12	8.24E-12	-30.91	5	5	5	0.23

Table 3.1. (Cont.)

Experiment	pH out	$C_{Si.out}$	$C_{Al.out}$	$C_{Mg.out}$	$\Delta C_{Al}/\Delta C_{Si}$	$\Delta C_{Mg}/\Delta C_{Si}$	R_{Si}	R_{Al}	R_{Mg}	ΔG_r	error R_{Si}	error R_{Al}	error R_{Mg}	error ΔG_r
		(μM)					(mol g^{-1} s^{-1})			(kcal mol^{-1})		(%)		(kcal mol^{-1})
pH ≈ 4														
Sm-SL2-4	3.91	1.75	0.89	0.40	0.51	0.23	8.79E-13	1.10E-12	1.62E-12	-23.82	5	5	6	0.23
Sm-SL10-4*	3.94	9.32	1.89	1.49	0.20	0.16	1.04E-12	5.35E-13	1.48E-12	-18.68	5	5	5	0.23
Sm-SL20-4*	3.95	21	1.20	4.19	0.06	0.20	1.12E-12	1.63E-13	1.88E-12	-16.83	5	5	5	0.23
Sm-SL10-4b	4.10	106	34.5	0.69	-	0.30	2.55E-13	-	6.80E-13	-9.35	233		5	0.23
Sm-SL20-4b	4.08	111	24.0	1.87	-	0.33	3.09E-13	-	8.67E-13	-9.48	97		5	0.23
Sm-SL2-4c	4.08	37.8	36.9	0.48	1.14	-	5.07E-13	1.48E-12	-	-12.15	189	161	-	0.23
Sm-SL10-4c	4.09	39.5	35.2	0.55	-	0.17	3.36E-13	-	4.95E-13	-11.68	61		5	0.23
Sm-SL20-4c	4.15	41.4	21.6	2.59	-	0.53	2.71E-13	-	1.27E-12	-11.22	42		5	0.23
Sm-SL10-4Al	4.01	2.96	35.3	0.42	-	0.14	3.12E-13	-	3.16E-13	-18.45	5		7	0.23
Sm-SL10-4e*	3.98	213	6.98	0.49	-	0.05	1.20E-12	-	4.84E-13	-10.22	100		5	0.23
Sm-SL10-4ba	3.99	112	37.8	0.41	-	0.11	3.69E-13	-	3.56E-13	-10.07	149		5	0.23
Sm-SL10-4i	4.03	117	16.3	2.09	-	0.25	2.47E-13	-	5.54E-13	-10.07	71		5	0.23
Sm-SL10-4l	4.02	109	28.0	1.52	-	0.31	2.50E-13	-	6.53E-13	-9.90	112		5	0.23

*no steady state

3.1 Theoretical background

A general form of rate law for one mechanism of heterogeneous mineral surface reactions that include all variables involved in mineral alteration was proposed by Lasaga (1998):

$$\text{Rate} = k_0 \cdot A_{min} \cdot \mathrm{e}^{-E_{app}/RT} \cdot a_{H^+}^{n_{H^+}} \cdot \prod_i a_i^{n_i} \cdot g(I) \cdot f(\Delta G_r) \qquad 3.1$$

where k_0 is a constant, A_{min} is the reactive surface area of the mineral, E_a is the apparent activation energy of the overall reaction, R is the gas constant, T is the absolute temperature, a_i and a_{H^+} are the activities in solution of species i and H^+ respectively, n_{H^+} and n_i are the orders of the reaction with respect to protons and species *i,* g(*I*) is a function of the ionic strength (*I*) and *f*(ΔG_r) is a function of the Gibbs free energy. This last term accounts for the important variation of the rate with deviation from equilibrium.

The control that the degree of saturation exerts on the smectite dissolution rate was shown to be critic in diverse environmental scenarios, such as nuclear waste repositories (Cama et al., 2000; Savage et al., 2011) and silicate weathering (White and Brantley, 2003).

The form of the last term in Eq. (3.1), *f*(ΔG_r) for an elementary reaction based on the Transition State Theory (TST) is (Lasaga, 1998):

$$f(\Delta \mathrm{G_r}) = 1 - \exp\left(\frac{\Delta \mathrm{G_r}}{\mathrm{RT}}\right) \qquad 3.2$$

where *R* is the gas constant and *T* is the absolute temperature. The function *f*(ΔG_r) for overall reactions is difficult to predict a priori. Equation (3.2) may be generalized to (Aagaard and Helgeson, 1982):

$$f(\Delta \mathrm{G_r}) = 1 - \exp\left(\frac{\Delta \mathrm{G_r}}{\sigma \mathrm{RT}}\right) \qquad 3.3$$

where σ is a coefficient that is not necessarily equal to 1. Near equilibrium, i.e., $|\Delta G_r| << \sigma RT$, the approximation exp(x) = 1 + x leads to a linear dependence of the rate on $\Delta \mathrm{G_r}$:

$$f(\Delta \mathrm{G_r}) = \frac{\Delta \mathrm{G_r}}{\sigma \mathrm{RT}} \qquad 3.4$$

The form of Eq. (3.4) can be applied to overall reactions in a few simple cases that are described by Lasaga (1998). In all these cases, defects such as dislocations should not control the dissolution kinetics (Rimstidt and Barnes, 1980; Nagy et al., 1991; Berger et al., 1994; Gautier et al., 1994; Oelkers et al., 1994; Devidal et al., 1997; Oelkers and Schott, 1999). In

other studies on the dissolution and precipitation kinetics of silica, gibbsite, albite, labradorite, smectite, kaolinite and fluorite (Nagy and Lasaga, 1992; Burch et al., 1993; Carroll et al., 1998; Nagy et al., 1999; Cama et al., 2000; Taylor et al., 2000a; Yang and Steefel, 2008; Cama et al., 2010; Marty et al., 2011) the experimental observations lead to fully nonlinear rate laws, i.e., rate laws in which the rate is not a linear function of the Gibbs free energy even very close to equilibrium. For example, Nagy and Lasaga (1992) described the gibbsite rate dependence using the function:

$$f(\Delta G_r) = 1 - exp\left(m \cdot \left(\frac{\Delta G_r}{RT}\right)^n\right) \quad 3.5$$

and Yang and Steefel (2008) described the kaolinite rate dependence at pH 4 and 22 °C using the function:

$$f(\Delta G_r) = 1 - \exp\left(\frac{-\Delta G_r}{2RT}\right) \quad 3.6$$

Eqs. (3.5) and (3.6) show that the dissolution rate near equilibrium is slower than at far from equilibrium conditions where it is independent of ΔG_r and becomes constant at the dissolution plateau (Figure 3.1).

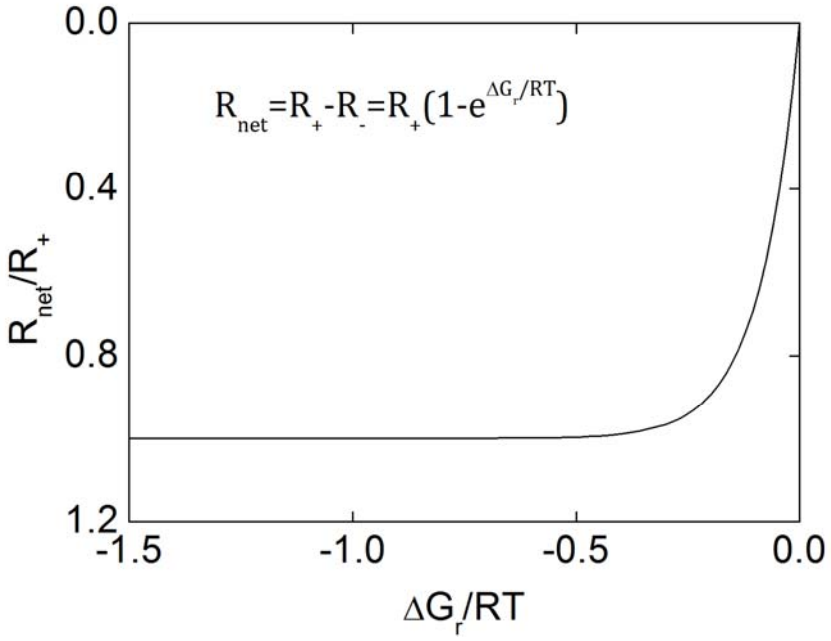

Figure 3.1. The effect of deviation from equilibrium (ΔG_r) on dissolution rate is described by the highly no linear $f(\Delta G_r)$ function. The far from equilibrium region where the function $f(\Delta G_r)$ is flat is termed the dissolution plateau (Nagy et al., 1991).

Cama et al. (2000) established the effect of the degree of saturation on the Cabo de Gata Na-smectite dissolution rate at pH 8.8 and 80 °C over a ΔG_r range from -31 to -3 kcal mol^{-1} using Nagy and Lasaga (1992) $f(\Delta G_r)$ function (Eq. (3.5) with m= -6x10^{-10} and n= 6:

$$R_{diss} = -8.1 \times 10^{-12} \cdot \left(1 - exp\left(-6 \times 10^{-10} \cdot \left(\frac{\Delta G_r}{RT}\right)^6\right)\right) \quad 3.7$$

Marty et al. (2011) used a similar $f(\Delta G_r)$ expression to propose a dissolution rate law for a synthetic Na-smectite at 50 °C and pH=9 with m=-8.23×10^{-10} and n=5.47 over a ΔG_r range from -25 to -19 kcal mol^{-1}:

$$R_{diss} = -3.8 \times 10^{-12} \cdot \left(1 - exp\left(-8.23 \times 10^{-10} \cdot \left(\frac{\Delta G_r}{RT}\right)^{5.47}\right)\right) \quad 3.8$$

An important aspect to highlight is that Eqn. (3.7) and (3.8) are not based on a first principle theory, and therefore there is no physical meaning to the values of the coefficients m and n (Cama et al., 2000). Also, the dissolution plateau was not approached in both studies over the respective ΔG_r ranges.

Contrary to Cama et al. (2000) and Marty et al. (2011), Metz (2001) studied the SAz-1 smectite dissolution kinetics at acid pH (3) and 50 °C over a ΔG_r range from -44 to -2 kcal mol^{-1}. The proposed smectite dissolution rate law was based on the same functional dependency (the m and n coefficients of the $f(\Delta G_r)$ term were 1x10^{-7} and 5±2, respectively):

$$R_{diss} = -8 \times 10^{-13} \cdot \left(1 - exp\left(-1 \times 10^{-7} \cdot \left(\frac{\Delta G_r}{RT}\right)^{5\pm2}\right)\right) \quad 3.9$$

In this study, the smectite dissolution plateau was approached at ΔG_r of -34 kcal mol^{-1} (Figure 3.2). Interestingly, Metz (2001) used the $f(\Delta G_r)$ term proposed by Cama et al. (2000) to account for the ΔG_r-rate dependency, yielding the expression:

$$R_{diss} = -8 \times 10^{-13} \cdot \left(1 - exp\left(-6 \times 10^{-10} \cdot \left(\frac{\Delta G_r}{RT}\right)^6\right)\right) \quad 3.10$$

Therefore, a $f(\Delta G_r)$ term obtained at basic and acid pH was valid to account for the effect of degree of saturation on the smectite dissolution rate independent of pH.

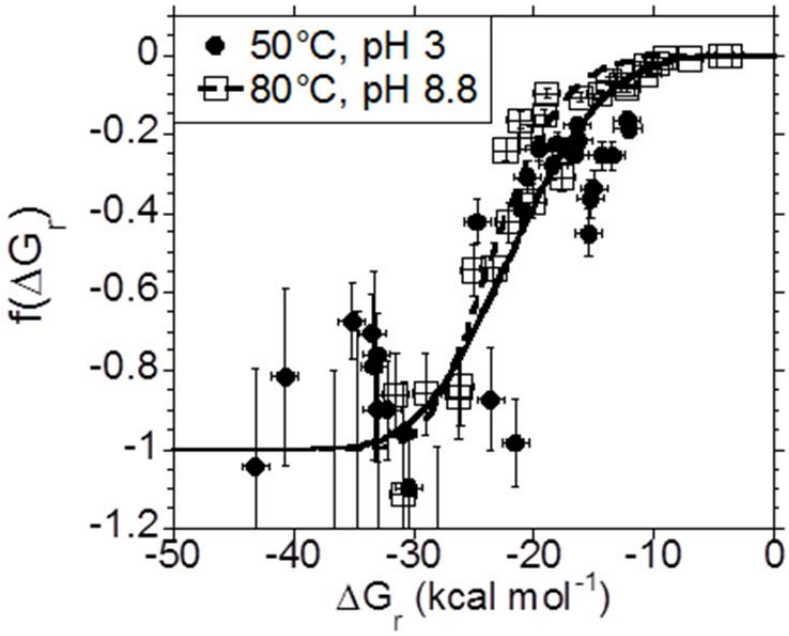

Figure 3.2. Comparison between normalized smectite dissolution rates obtained at pH 8.8 and 80 °C (Cama et al., 2000) and pH 3 and 50 ° C (Metz, 2001). Solid curves show similar $f(\Delta G_r)$ shape between the smectite rate laws proposed by the authors (see text).

3.2 Reactive transport modeling

Simulations of the variation in aqueous Si, Al and Mg with time in a representative stirred flow-through experiment at pH 3, 25 °C and atmospheric pressure (Sm-SL-20-3) were performed using CrunchFlow (Steefel, 2009; Steefel et al., 2014). This numerical approach allows further discussion on potential processes other than montmorillonite dissolution that could intervene in the overall reaction.

3.2.1 Description of the CrunchFlow reactive transport code

The CrunchFlow code solves numerically the mass balance of solutes expressed as

$$\frac{\partial(\phi C_j)}{\partial t} = \nabla \cdot \left(D \nabla C_j\right) - \nabla\left(q C_j\right) + R_j \qquad (j = 1, 2, \ldots, n) \qquad 3.11$$

where ϕ is porosity, C_j is the concentration of component j (mol m^{-3}), D is the combined dispersion-diffusion coefficient (m^2 s^{-1}), q is the Darcian fluid flux (m^3 m^{-2} s^{-1}) and R_j is the total reaction rate affecting component j (mol m^{-3}_{bulk} s^{-1}).

The total reaction rate for the component *j*, R_j is given by

$$R_j = -\sum_m \nu_{jm} R_m \qquad 3.12$$

where R_m is the rate of dissolution ($R_m < 0$) or precipitation ($R_m > 0$) of mineral *m* in mol m^{-3}_{bulk} s^{-1}, and ν_{jm} is the number of moles of *j* per mole of mineral *m*.

Since mineral reactions are described using kinetic rate laws (Eq. (3.1)), initial reactive surface areas, initial mineral volume fractions and several reaction rate parameters have to be supplied by the user as input. In this set of simulations, the reaction rate laws used in the calculations are expressed as:

$$R_m = -A_m \sum_{terms} k_{r(m,T)} a_{H^+}^{n_{H^+}} \left(\prod_i a_i^{n_i}\right) f_m(\Delta G_r) \qquad 3.13$$

where R_m is the reaction rate for a given mineral in units of mol m^{-3}_{bulk} s^{-1}, A_m is the mineral surface area (m^2_m m^{-3}_{bulk}), k_r is the reaction rate constant (mol m^{-2} s^{-1}) at the temperature of interest, $a_{H^+}^{n_{H^+}}$ is the term describing the effect of pH on the rate, $a_i^{n_i}$ is a term describing a catalytic/inhibitory effect by another species on the rate, and $f_m(\Delta G_r)$ is the function describing the dependence of the rate on the solution saturation state. The summation term indicates that several parallel rate laws may be used to describe the dependence of the rate on pH or on other species.

The $f_m(\Delta G_r)$ function is defined as in Eq. (3.5), and the Gibbs energy of the reaction is defined as in Eq. (2.4) (J mol^{-1}) Note that in Eq. (3.5) *m* and *n* are empirical coefficients.

Changes in mineral surface area A_m (m^2_m m^{-3}_{bulk}) due to reaction are calculated according to:

$$A_m = A_{m,0} \left(\frac{\phi}{\phi_0}\right)^{2/3} \left(\frac{\phi_m}{\phi_{m,0}}\right)^{2/3} \qquad 3.14$$

where $\phi_{m,0}$ is the initial volume fraction of the mineral *m* and ϕ_m is the initial porosity of the medium. This formulation ensures that as the volume fraction of a mineral goes to 0, its surface area does too.

3.2.2 Numerical discretization

To reproduce the flow-through experiment conditions and considering the flow-through cell inner diameter (0.0125 m), a one-dimensional numerical domain composed of 3 elements of 0.312 m is used in the simulations.

3.2.3 Smectite and solution composition

Montmorillonite was the mineral considered in the calculations. Given the initial mineral mass (0.921 g) and the cell volume (46 cm^3), porosity porosity (ϕ) and mineral and mineral volume fraction (FV) for the experiment are 0.9915 and 0.00852, respectively. The fit of the model to the experimental data (aqueous Si, Al, Mg concentrations and pH) was performed by using a starting value for A_m of 12785 $m^2_m\ m^{-3}_{bulk}$.

In the simulations, the initial solution composition inside the flow-through cell was considered to be the same as the injected solution ([Ca] = [Mg] = [Al] = [Si] = [Fe] =10^{-9} mol kg^{-1}; [K] =10^{-2} mol kg^{-1}; [NO_3^-] = charge balance; pH = 3 and CO_2(aq) = 1.3x10^{-5}).

3.2.4 Flow and transport properties

The flow rate was the experimental one (0.0211 mL min^{-1}). The diffusion coefficient and longitudinal dispersivity used in the simulation were set at 10^{-5} m^2 s^{-1} and 10^{-1} m to guarantee the same concentration in the three nodes as expected in a well-mixed flow-through experiment.

3.2.5 Thermodynamic and kinetic data

Forty-three aqueous species were considered in the simulations. The equilibrium constant for the K-montmorillonite (log $K_{25°C}$) was the one derived in this study (5.30; Chapter 2). The stoichiometric coefficients, which were taken from the EQ3/6 database (Wolery, 1992a), included in the CrunchFlow code, are shown in Table 7.1 (Appendix I). Activity coefficients were calculated using the extended Debye-Hückel formulation (b-dot model) with parameters obtained from the CrunchFlow database (EQ3/6). The kinetic rate law used for K-montmorillonite is the one proposed in this study (see Section 3.5), such that m = -3.84·10^{-4} and n = 2.13 in Eq. (3.5).

3.2.6 Sorption reactions

Two types of reactions were included in the modeling to understand the behavior of the aqueous Mg and Al: cation exchange reaction between K^+ and Mg^{2+} and surface adsorption of Al^{3+}. The selectivity coefficients with respect to potassium and magnesium were expressed according to the Gaines and Thomas (1953) convention and are taken from Fernandez et al. (2004) (Table 7.2, Appendix I). The cation occupancies, the CEC value (9.59·10^{-4} eq/g of solid) and selectivity coefficients are from the FEBEX bentonite (Fernández et al., 2004). Following

Fernández et al. (2004), Al^{3+} adsorption was based on reactive sites associated with montmorillonite which are perceived as being surface hydroxyl groups (>SOHs and >SOHw) situated along the edges of the montmorillonite platelets. In this study, according to the surface complexation model developed by (Bradbury and Baeyens, 1997), two protolysis sites with the same capacities but with different protolysis constants were required (Table 7.2; Appendix I).

3.3 Effect of sample pretreatment

It has been shown that the use of pretreated clay samples shorten the time to reach steady state in flow-through experiments (Nagy et al., 1991; Cama et al., 2000). Sample pretreatment was examined in the present study to confirm whether steady state was approached faster. The pretreated and raw K-montmorillonite samples were reacted at pH 3 and 4 under the same experimental conditions (same mass and flow rate; Table 3.1).

The comparison between variations of the output concentration with time is shown in (Figure 3.3). Similar variation in the Si and Al output concentrations was observed in experiments that lasted for 3000 h (Figure 3.3a,b-d,e). At pH 3, however, the release of Si and Al from the raw sample was slightly higher than that from the pretreated sample for the first 500 h. At both experimental pHs, steady state was reached after approximately 2000 h regardless the type of sample. The measured Mg output concentrations at steady state were also the same within error (Figure 3.3c,f). Given this similarities, it is suggested that the performed pretreatment did not influence the K-montmorillonite dissolution reaction. In light of the above observations, the flow-through experiments were carried out using raw or pretreated K-montmorillonite samples indistinctly.

3.4 Dissolution reaction of K-montmorillonite

Overall, the temporal variation of Si, Al and Mg output concentrations in the flow-through experiments showed two stages. The first stage was characterized by a remarkable decrease in concentration of Si and Mg, and that of Al in some cases. In the second stage, the output concentration of Si, Mg and in some experiments Al gradually decreased and often reached steady state (Figures 3.3-3.6). The behaviour of the output Al concentrations depended on the initial composition of the input solutions.

3.4.1 Variation of the cation concentrations

The net variation of concentration of element *i*, ΔC_i, was defined as the difference between the concentrations of element *i* in the output and the input solutions ($C_{i,out}$ and $C_{i,inp}$):

$$\Delta C_i = C_{i,out} - C_{i,inp} \quad 3.15$$

Positive ΔC_i values corresponded to an excess of concentration of element *i*, associated to K-montmorillonite dissolution, whereas negative values indicated a deficit in concentration of element *i*, related to the occurrence of cation exchange, sorption and/or precipitation along with K-montmorillonite dissolution. Note that $C_{i,inp} = 0$ implies $\Delta C_i = C_{i,out}$.

Si was exclusively related to K-montmorillonite dissolution because precipitation of secondary Si-bearing phases (amorphous SiO_2 and quartz) was unlikely to occur in the studied pH range (2-4) and room temperature. In contrast, released Al and Mg from K-montmorillonite dissolution were involved in backward reactions. Although precipitation of Mg-bearing phases was unlikely, Mg sorption on the K-montmorillonite interlayer might occur. Al was incorporated in the interlayers by cation exchange, adsorbed on the surface and/or precipitated as a secondary phase (e.g., $Al(OH)_3$). Nonetheless, K-Al exchange should be little in this study considering that K-montmorillonite dissolved in a 0.01 mol L^{-1} KNO_3-electrolyte background.

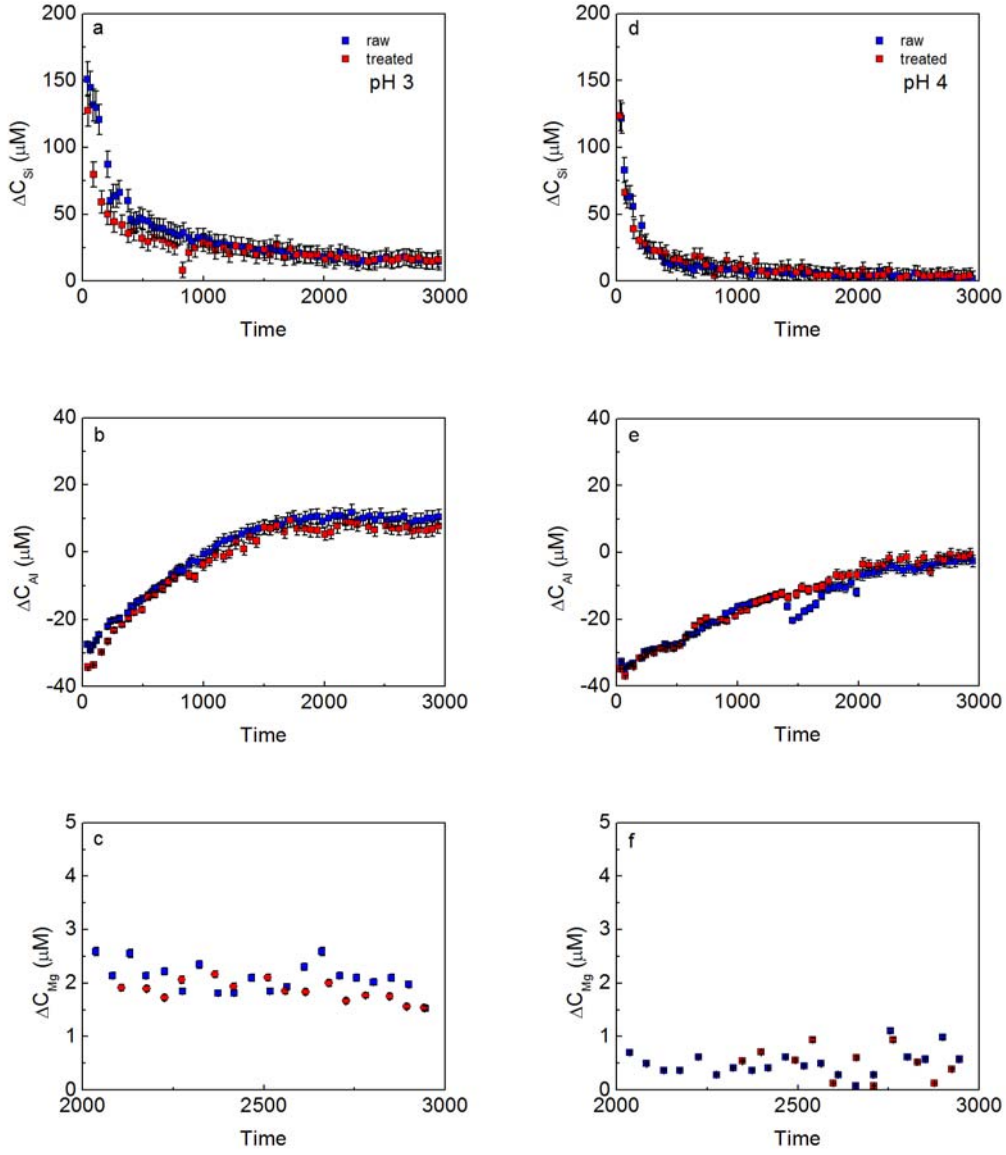

Figure 3.3. Variation in ΔC_{Si}, ΔC_{Mg} and ΔC_{Al} as a function of time in experiments with raw (Sm-SL10-3b and Sm-SL10-4b) and preconditioned (Sm-SL10-3b2 and Sm-SL10-4b2) solid sample, at pH3 (a-c) and b) pH4 (d-f). Observed ΔC_{Al} drop in (e) was probably caused by a temporary temperature fall.

3.4.2 Experiments with $C_{Si,inp} = C_{Al,inp} = 0$

Temporal variation of Si, Al and Mg concentration when when $C_{Si,inp} = C_{Al,inp} = 0$ is shown in Figures 3.4-3.6. At pH 2 (Figure 3.4a,b), the concentrations decreased until steady state was attained. It was observed that the higher the S/L ratio the higher the output concentration. At pH 3 and 4 (Figures 3.5a,b and 3.6a,b), the behavior of the Si and Mg concentrations was characterized by an initial descend in concentration (first stage) that was followed by a gradual decrease (second stage). Stoichiometry was approached only in the

experiments with S/L = 2, and the output concentrations increased by increasing S/L. The Al concentration started to increase, reaching steady state only for S/L = 2 (Figures 3.5c and 3.6c).

The solution pH barely changed over the experimental runs at pH 2 (Figure 3.7). Only at the beginning of the experiments at pH 3 and 4 (from 20 to 300 h; Figure 3.7), the output pH was slightly higher than the input pH. This initial H^+ consumption was attributed to an initially higher dissolution of K-montmorillonite and/or exchange of interlayer K^+ for H^+.

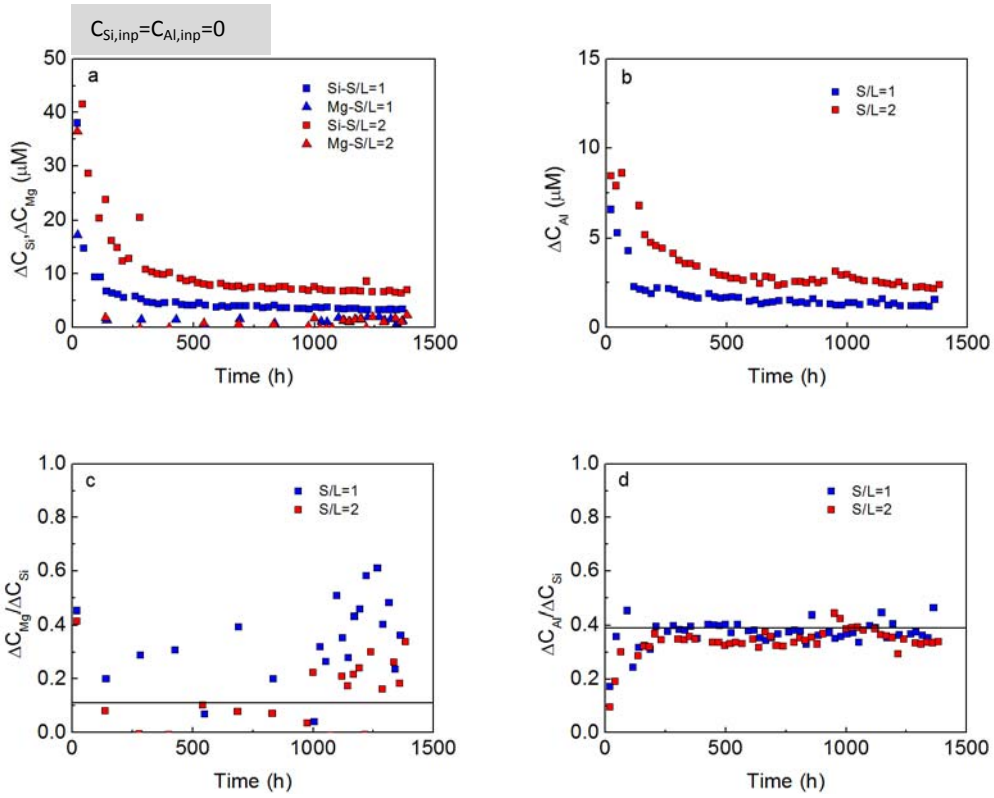

Figure 3.4. Variation in ΔC_{Si}, ΔC_{Mg} and ΔC_{Al} and stoichiometry ratios as a function of time in experiments run at pH 2, cation-free input solution and different S/L ratios (Sm-SL1-2 and Sm-SL2-2).

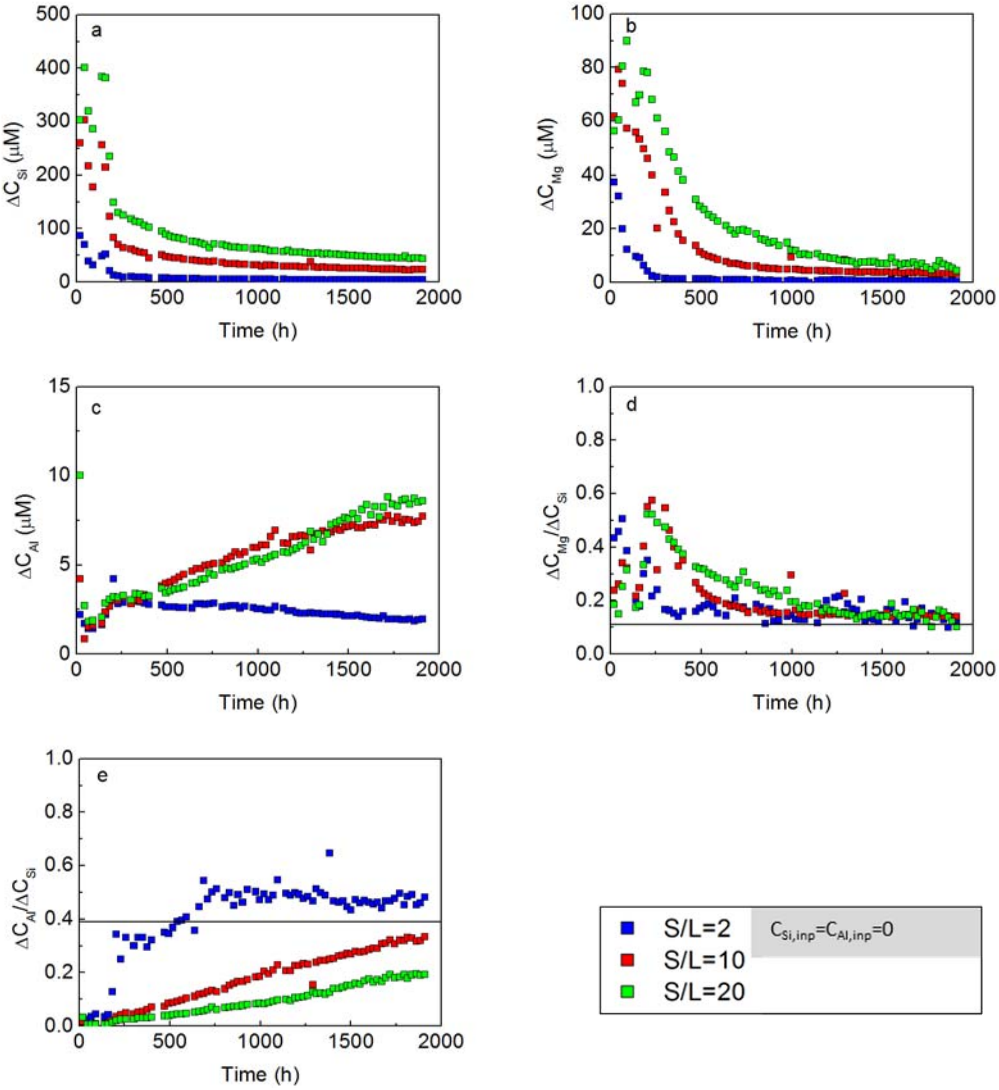

Figure 3.5. Variation in ΔC_{Si}, ΔC_{Mg} and ΔC_{Al} and stoichiometry ratios as a function of time in experiments run at pH 3, cation-free input solution and different S/L ratios (Sm-SL2-3a; Sm-SL10-3a and Sm-SL20-3a).

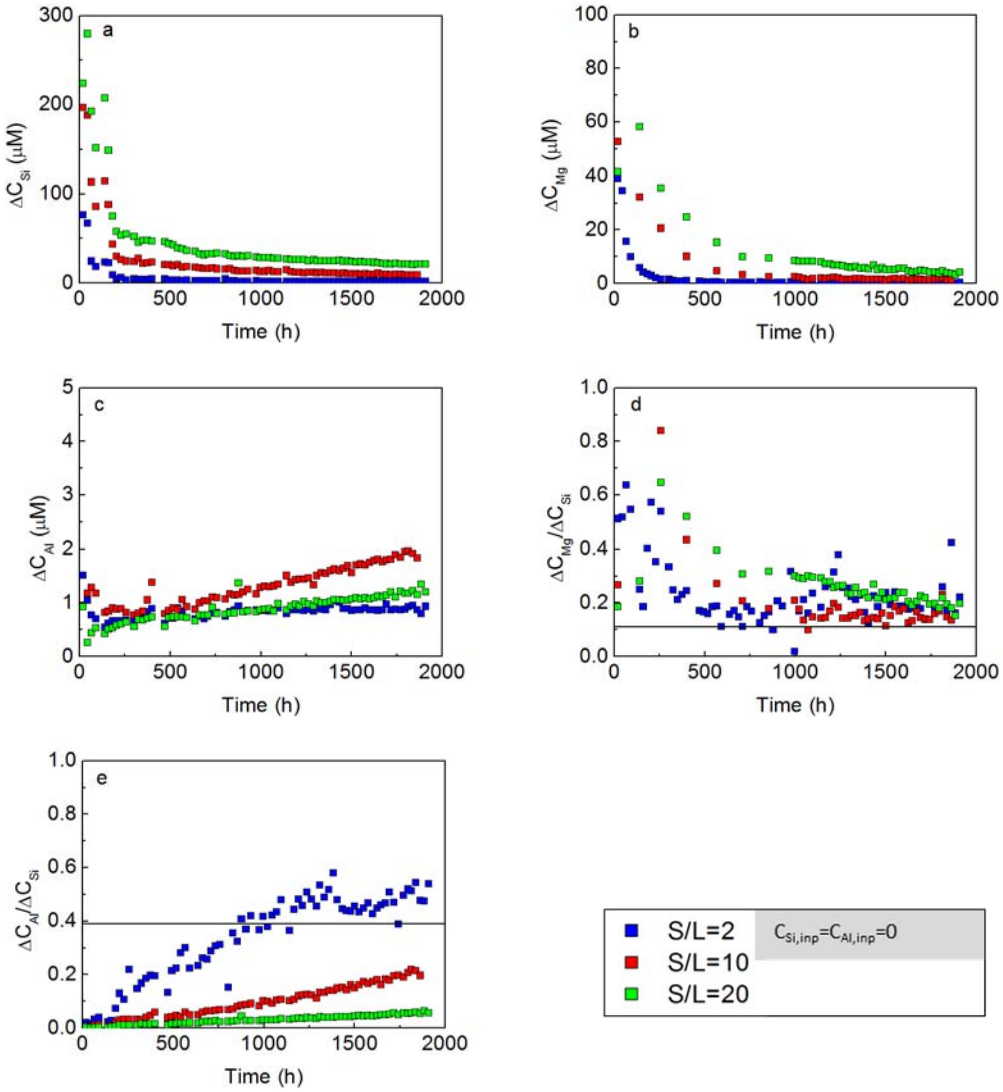

Figure 3.6. Variation in ΔC_{Si}, ΔC_{Mg} and ΔC_{Al} and stoichiometry ratios as a function of time in experiments run at pH 4, cation-free input solution and different S/L ratios (Sm-SL2-4a; Sm-SL10-4a and Sm-SL20-4a).

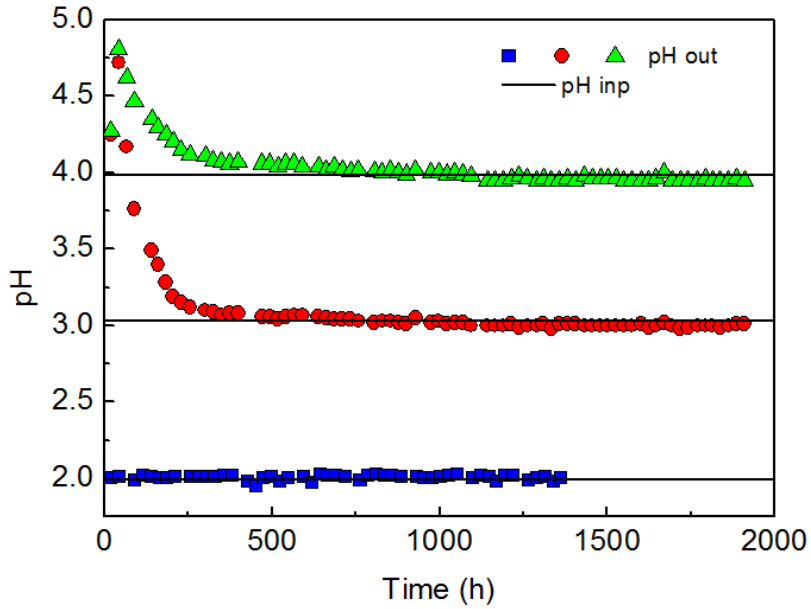

Figure 3.7. pH variation in the input and output solutions as a function of time. Blue, red and green solid symbols are for pH 2, 3 and 4, respectively.

3.4.3 Experiments with $C_{Si,inp}$ and/or $C_{Al,inp} > 0$

The temporal variation of the output Si, Al and Mg concentration when $C_{Si,inp}$ and/or $C_{Al,inp} > 0$ is shown in Figures 3.8-3.10. At pH 2 and $C_{Si,inp} > 0$ and $C_{Al,inp} = 0$, ΔC_{Si} and ΔC_{Mg} started to decrease to reach steady state thereafter (Figure 3.8a). Otherwise, ΔC_{Al} started to increase and thereafter gradually decreased (Figure 3.8b). ΔC_{Si}, ΔC_{Mg} and ΔC_{Al} were the same within error in both experiments independently of $C_{Si,inp}$,, which varied from 12 to 376 μM.

At pH 3 and $C_{Si,inp} \approx 107$ μM and $\approx C_{Al,inp}$ 37 μM and pH 4 and $C_{Si,inp} \approx 36$ μM and $C_{Si,inp} \approx$ 37 μM, ΔC_{Si} and ΔC_{Mg} also started to decrease and reached steady state thereafter (Figures 3.9a,b,c and 3.10a,b,c). Note that the higher the mass, the higher ΔC_{Si} and ΔC_{Mg}, indicating thus an increase in smectite dissolution by increasing the mass. In the case of Al release, in all experiments run at pH 3 and 4, a significant deficit in the output Al concentration was observed for several hundred hours, yielding negative ΔC_{Al} (Figures 3.9c and 3.10c). With time, at pH 3, ΔC_{Al} increased, an Al excess was obtained, and steady state was reached (Figure 3.9c). At pH 4, ΔC_{Al} also increased, but the approach to steady state took longer (Figure 3.10c). As in the experiments run at pH 3, the time span to reach steady state was longer by increasing the amount of mass (S/L from 2 to 20). In particular, when S/L = 20, an Al steady state was not achieved (Figure 3.9c).

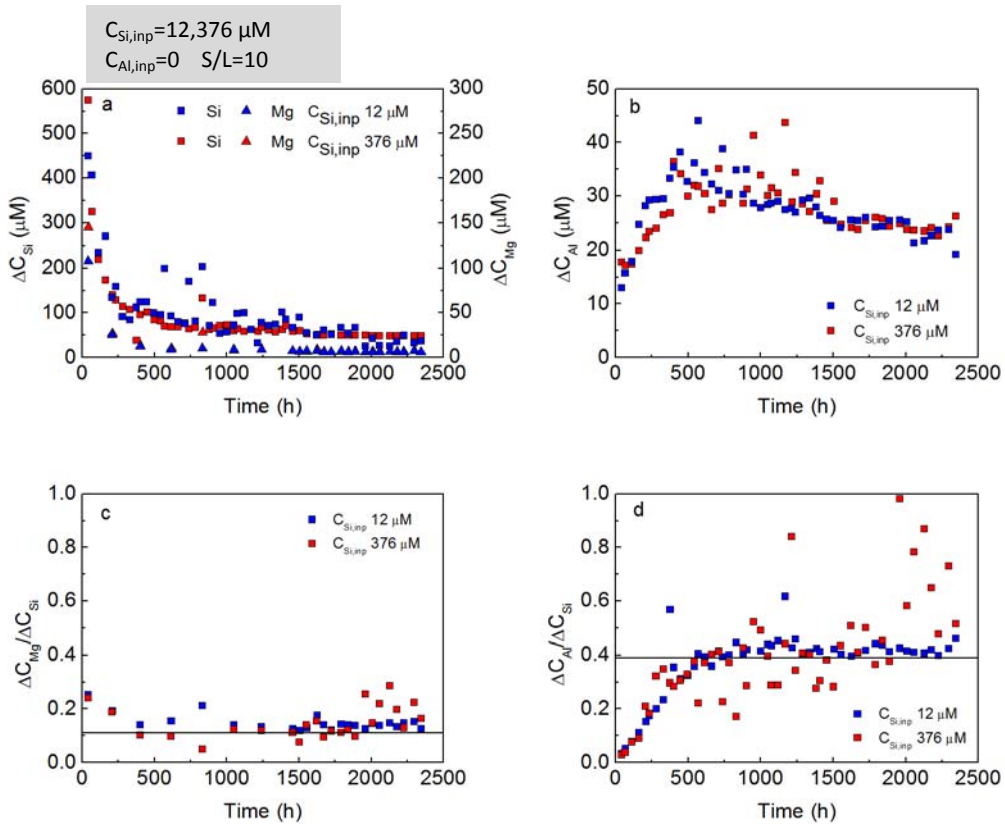

Figure 3.8. Variation in ΔC_{Si}, ΔC_{Mg} and ΔC_{Al} and stoichiometric ratios as a function of time in experiments run at pH 2, S/L = 10 and $C_{Si,inp}$ of 12 and 376 µM (Sm-SL10-2a and Sm-SL10-2d). Solid line indicates the ideal stoichiometric ratio value.

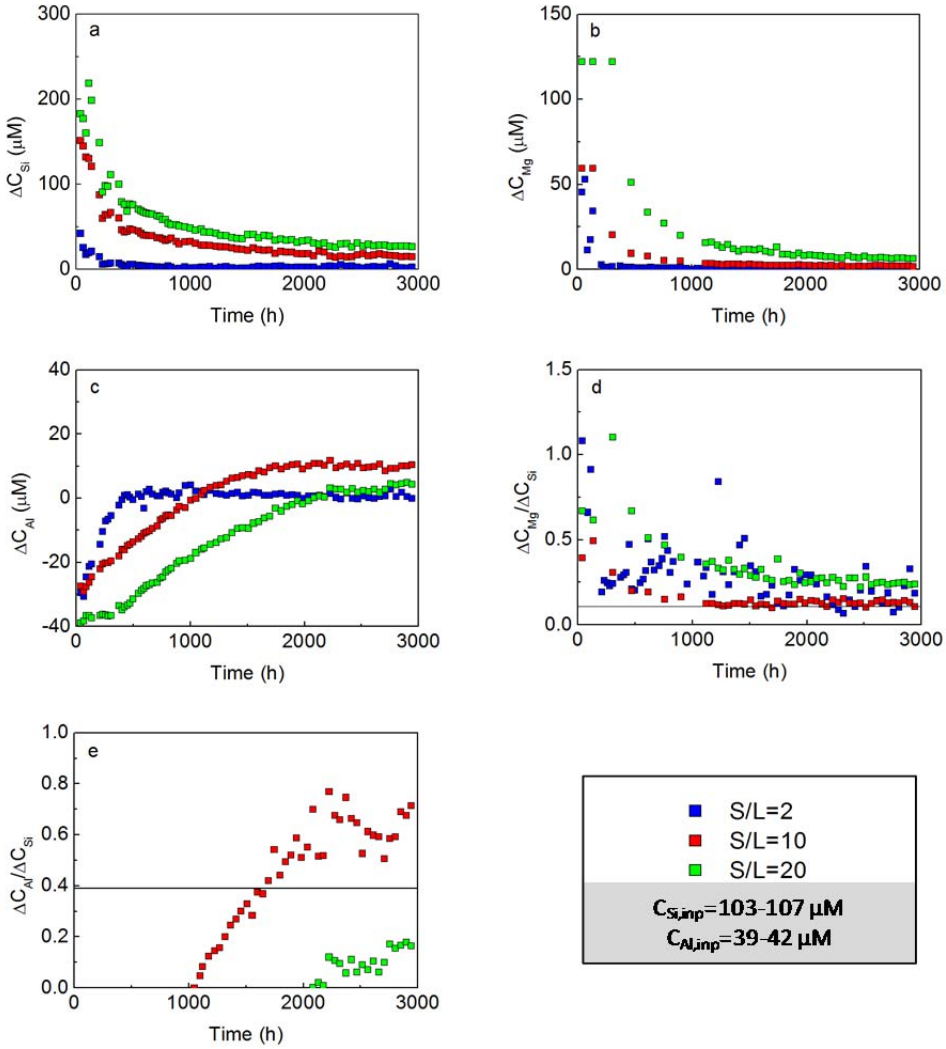

Figure 3.9. Variation in ΔC_{Si}, ΔC_{Mg} and ΔC_{Al} and stoichiometric ratios as a function of time in experiments run at pH 3, different S/L ratios and $C_{Si,inp}$ ≈100 μM and $C_{Al,inp}$ ≈ 40 μM (Sm-SL2-3b; Sm-SL10-3b and Sm-SL20-3b). Solid line indicates the ideal stoichiometric ratio value.

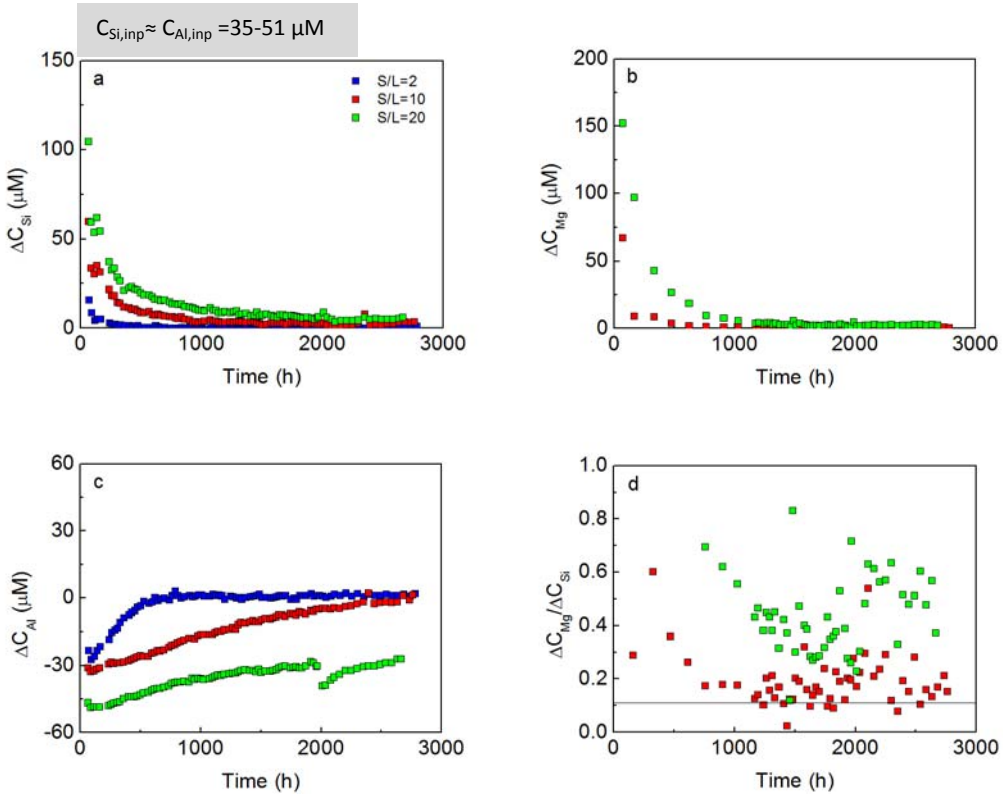

Figure 3.10. Variation in ΔC_{Si}, ΔC_{Mg} and ΔC_{Al} and stoichiometric ratios as a function of time in experiments run at pH 4, different S/L ratios and $C_{Si,inp} \approx C_{Al,inp} \approx$ 35-51 µM (Sm-SL2-4c, Sm-SL10-4c and Sm-SL20-4c). $\Delta C_{Al,out}$ is below the instrument detection limit. ΔC_{Al} drop in (c) was caused by a temporary temperature fall. Solid line indicates the ideal stoichiometric ratio value.

A second series of experiments was run at pH 3 and 4 and S/L of 10, where $C_{Si,inp}$ was varied from 0 to 107 µm and $C_{Al,inp}$ was always 37 µm (Figures 3.11 and 3.12). The variation of ΔC_{Si} was similar, decreasing with time and reaching steady state at both pH values. At pH 3, ΔC_{Al} started being negative, increasing thereafter to reach steady state (Figure 3.11c), and at pH 4, the ΔC_{Al} variation was similar but the attainment of steady state was longer (Figure 3.12c). From the experimental results, it was inferred that (1) as $C_{Al,inp} > 0$ (37 µm) an Al deficit was originated and (2) an increase in S/L delayed the steady-state achievement.

During the stage with negative ΔC_{Al}, two processes were contemplated to take place: Al sorption or Al re-precipitation on the K-smectite surface.

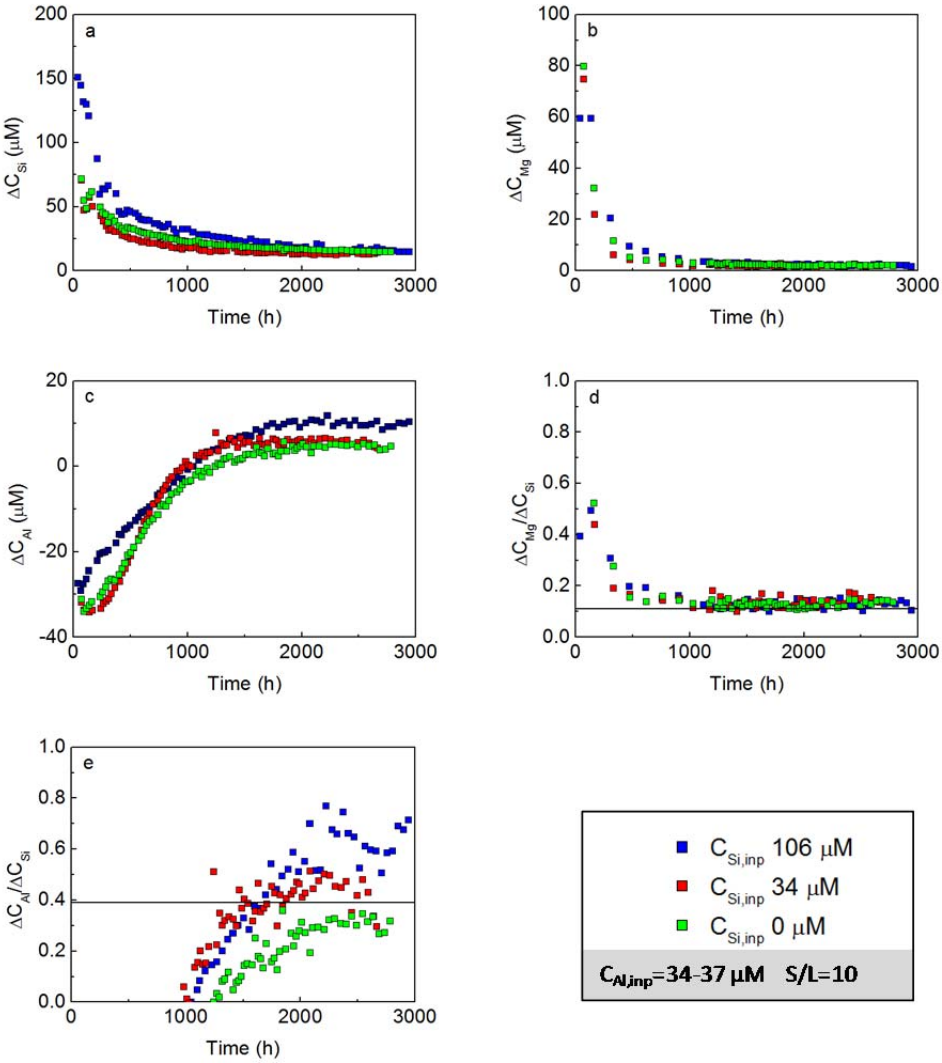

Figure 3.11. Variation in ΔC_{Si}, ΔC_{Mg} and ΔC_{Al} and stoichiometric ratios as function of time in experiments at pH 3, S/L =10 and $C_{Al,inp}$ ≈ 35 μM and $C_{Si,inp}$ ≈ 0, 34 and 106 μM (Sm-SL10-3b, Sm-SL10-3c and Sm-SL10-3Al). Solid line indicates the ideal stoichiometric ratio value.

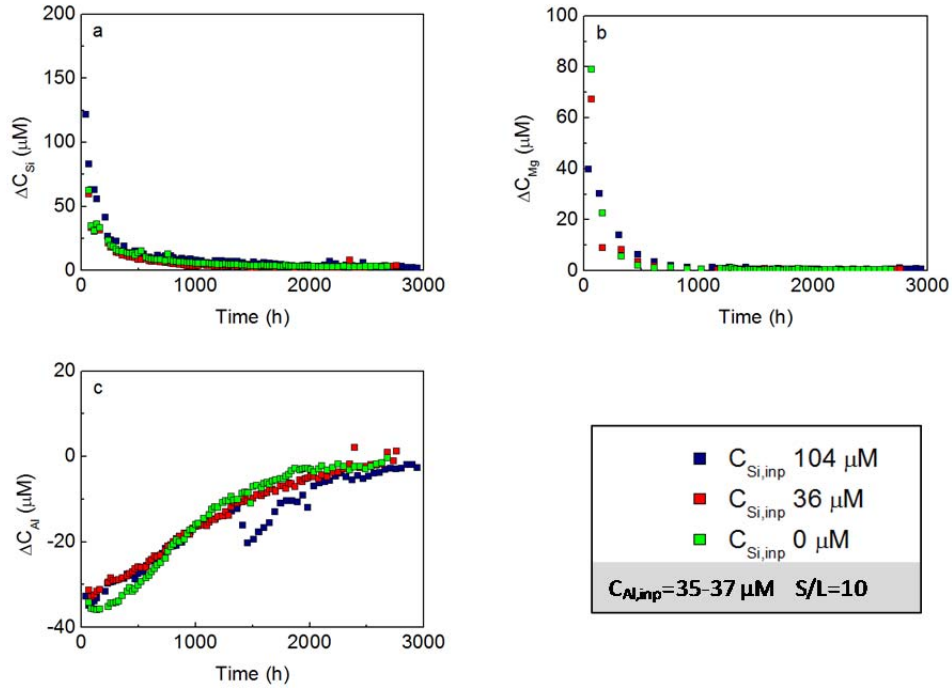

Figure 3.12. Variation in ΔC_{Si}, ΔC_{Mg} and ΔC_{Al} as a function of time in experiments run at pH 4, S/L = 10 and $C_{Al,inp}$ ≈ 35 μM and $C_{Si,inp}$ ≈ 0, 36 and 104 μM (Sm-SL10-4b; Sm-SL10-4c and Sm-SL10-4Al).

In a third series of experiments, a first experiment was performed at pH 2 with S/L = 2 (initial mass was ≈ 0.09 g), flow rate of 0.02 and 0.07 mL $min^{-1}$and $C_{Si,inp}$ = $C_{Al,inp}$ = 0 (Figure 3.13) ΔC_{Si}, ΔC_{Mg} and ΔC_{Al} increased by decreasing the flow rate, indicating that K-montmorillonite dissolution increased by increasing the residence time. In the second set, at pH 3 and 4 (Figure 3.14) and S/L = 10 (initial mass was ≈ 0.46 g), the flow rate varied from 0.006 to 0.02 mL min^{-1} and $C_{Si,inp}$ ≈ 104-108 μm and $C_{Al,inp}$ ≈ 34-43 μm. As expected, ΔC_{Si} and ΔC_{Mg} increased by decreasing the flow rate. However, the behavior of Al was more complex, as ΔC_{Al} depended not only on flow rate and initial mass, but also on eventual sorption (adsorption and precipitation) reactions.

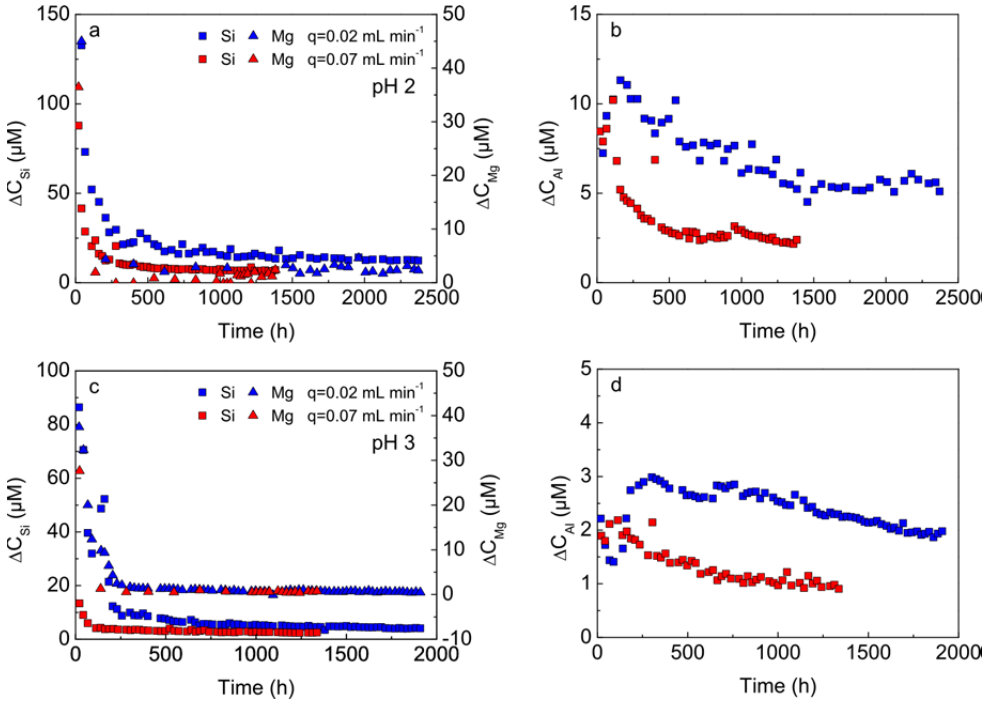

Figure 3.13. Variation in ΔC_{Si}, ΔC_{Mg} and ΔC_{Al} as a function of time in experiments with S/L = 2, free-cation input solution and variable flow rate (0.02-0.07 mL min^{-1}) (a) at pH 2 (Sm-SL2-2a and Sm-SL2-2b) and (b) at pH 3 (Sm-SL2-3a and Sm-SL2-3d).

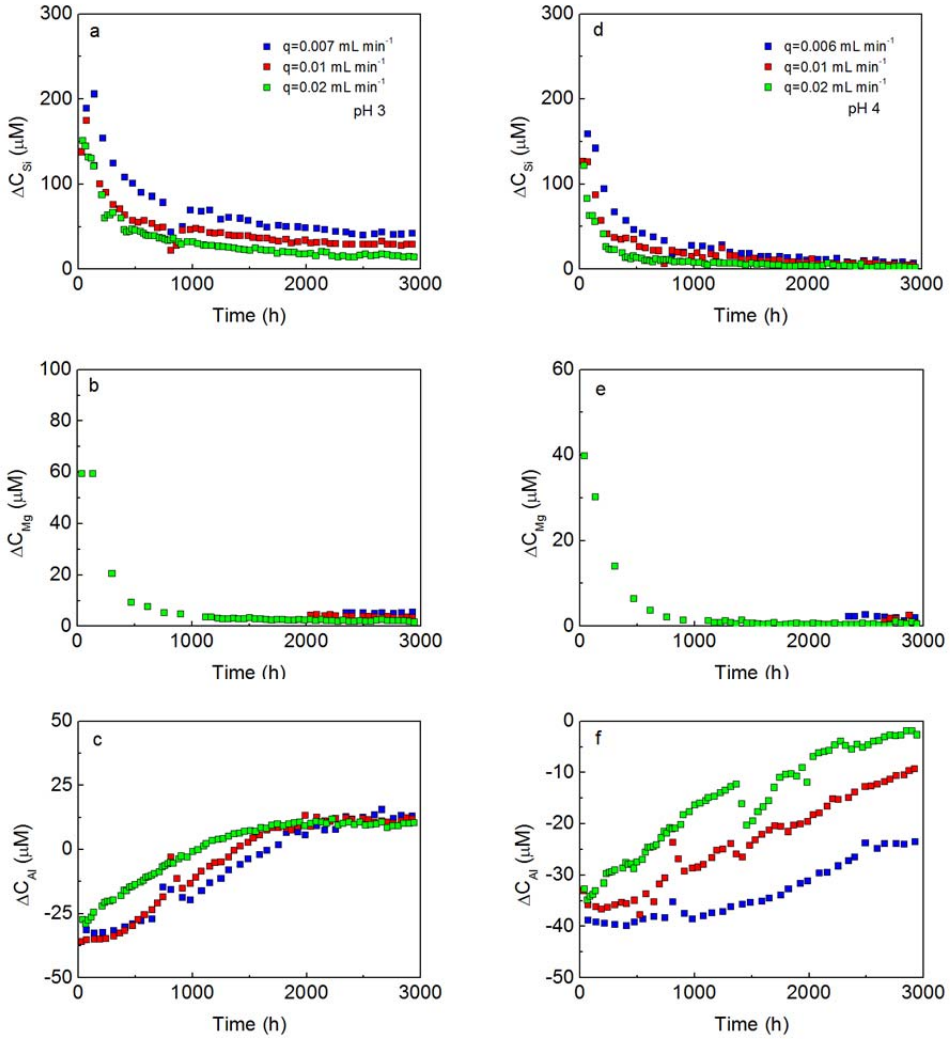

Figure 3.14. Variation in ΔC_{Si}, ΔC_{Mg} and ΔC_{Al} as a function of time in experiments with S/L =10, free-cation input solution and variable flow rate (0.007-0.02 mL min^{-1}) at pH 3 (a-c) (Sm-SL10-3b; Sm-SL10-3h and Sm-SL10-3i) and at pH 4 (d-f) (Sm-SL10-4b; Sm-SL10-4i and Sm-SL10-4l).

Table 3.2 lists the SI values with respect to plausible phases that could influence the results in the overall reaction. Most of the SI values are negative, suggesting undersaturation with respect to most of these phases, and only in a few experiments SI showed positive values with respect to quartz.

Table 3.2. Calculated saturation indexes (*SI*) with respect to K-montmorillonite (K-Mt), amorphous SiO_2 (SiO_2(am)), boehmite (Bhm), gibbsite (Gbs), kaolinite (Kln) and muscovite (Ms) from the steady-state output solutions.

Experiment	pH	K-Mt	SiO_2(am)	Qz	Bhm	Gbs	Kln	Ms
pH ≈ 2								
Sm-SL1-2	2.00	-34.59	-3.77	-2.02	-10.82	-11.08	-25.23	-42.53
Sm-SL2-2a	2.05	-29.38	-2.96	-1.20	-9.75	-10.01	-21.47	-36.82
Sm-SL2-2b	2.01	-32.26	-3.35	-1.60	-10.44	-10.70	-23.64	-40.14
Sm-SL10-2a	2.02	-24.39	-2.06	-0.31	-9.00	-9.26	-18.18	-31.92
Sm-SL10-2b	2.06	-23.34	-1.86	-0.10	-8.89	-9.15	-17.55	-30.92
Sm-SL10-2c	2.03	-21.88	-1.46	0.29	-8.95	-9.21	-16.87	-29.95
Sm-SL10-2d	2.04	-19.71	-0.92	0.84	-8.94	-9.21	-15.78	-28.30
pH ≈ 3								
Sm-SL2-3	2.99	-25.54	-3.65	-1.89	-6.39	-6.65	-16.13	-27.51
Sm-SL10-3	2.98	-19.83	-2.62	-0.87	-5.63	-5.89	-12.56	-22.17
Sm-Sl20-3	3.00	-17.88	-2.24	-0.48	-5.47	-5.73	-11.47	-20.50
Sm-SL2-3b	2.95	-15.23	-1.72	0.04	-4.77	-5.03	-9.03	-16.92
Sm-SL10-3b	2.96	-14.40	-1.64	0.12	-4.66	-4.93	-8.66	-16.34
Sm-SL20-3b	2.98	-13.74	-1.58	0.18	-4.58	-4.84	-8.36	-15.87
Sm-SL10-3c	3.16	-15.06	-2.20	-0.44	-3.87	-4.13	-8.18	-15.36
Sm-SL20-3c	3.15	-14.55	-2.07	-0.33	-3.90	-4.17	-8.01	-15.12
Sm-SL10-3Al	3.08	-18.46	-2.88	-1.13	-4.20	-4.47	-10.23	-18.54
Sm-SL10-3d	2.97	-13.84	-1.28	0.47	-5.21	-5.47	-9.03	-16.86
Sm-SL10-3e	3.10	-11.44	-0.89	0.87	-4.76	-5.02	-7.35	-14.20
Sm-SL10-3f	3.08	-10.66	-0.45	1.30	-5.36	-5.63	-7.68	-14.72
Sm-SL10-3ba	3.03	-13.80	-1.64	0.12	-4.34	-4.60	-8.01	-15.27
Sm-SL10-3h	3.03	-13.06	-1.53	0.23	-4.29	-4.55	-7.69	-14.80
Sm-SL10-3i	3.03	-13.31	-1.58	0.17	-4.27	-4.54	-7.77	-14.91
pH ≈ 4								
Sm-SL2-4	3.91	-20.89	-4.15	-2.40	-3.10	-3.36	-10.57	-17.91
Sm-SL10-4*	3.94	-15.67	-3.16	-1.41	-2.54	-2.80	-7.45	-13.19
Sm-SL20-4*	3.95	-13.88	-2.67	-0.92	-2.77	-3.03	-6.93	-12.40
Sm-SL10-4b	4.10	-5.96	-1.72	0.04	-0.18	-0.44	0.15	-1.60
Sm-SL20-4b	4.08	-6.13	-1.70	0.06	-0.47	-0.73	-0.39	-2.41
Sm-SL2-4c	4.08	-8.68	-2.33	-0.58	-0.22	-0.48	-1.15	-3.56
Sm-SL10-4c	4.09	-8.37	-2.32	-0.56	-0.17	-0.43	-1.04	-3.36
Sm-SL20-4c	4.15	-7.94	-2.28	-0.52	-0.25	-0.52	-1.12	-3.41
Sm-SL10-4Al	4.01	-15.18	-3.84	-2.09	-0.52	-0.78	-4.78	-9.10
Sm-SL10-4e*	3.98	-7.25	-1.32	0.45	-1.74	-2.00	-2.18	-5.28
Sm-SL10-4ba	3.99	-6.58	-1.69	0.06	-0.54	-0.80	-0.51	-2.70
Sm-SL10-4i	4.03	-6.76	-1.66	0.09	-0.90	-1.16	-1.18	-3.66
Sm-SL10-4l	4.02	-6.53	-1.70	0.05	-0.62	-0.88	-0.70	-2.96

Grey background indicates supersaturation

3.4.4 The stoichiometry of the K-montmorillonite dissolution

The stoichiometric ratio between two components *i* and *j*, $\Delta C_i/\Delta C_j$ was defined as the ratio between the release of component *i* and the release of component *j* at steady state:

$$\frac{\Delta C_i}{\Delta C_j} = \frac{C_{i,out} - C_{i,inp}}{C_{j,out} - C_{j,inp}} \quad 3.16$$

The $\Delta C_{Al}/\Delta C_{Si}$ and $\Delta C_{Mg}/\Delta C_{Si}$ ratios were calculated for all experiments except for those where the output Al concentration was lower than the input one, and the output Mg concentration was below detection limit. Small differences between the input and output concentrations of Si and Al at steady state led to significant uncertainties in ΔC_{Si} and ΔC_{Al} and to the calculated stoichiometric ratios (Table 3.1).

When $C_{i,inp} = C_{j,inp} = 0$, at pH 2, the variation of the $\Delta C_{Al}/\Delta C_{Si}$ ratio with time indicated that the steady-state release of Al and Si was fairly stoichiometric (Figure 3.4c), whereas the variation of the $\Delta C_{Mg}/\Delta C_{Si}$ ratio showed a preferential release of Mg over Si (Figure 3.4d). At pH 3 and 4, the $\Delta C_{Mg}/\Delta C_{Si}$ ratio indicated a preferential release of Mg over Si, with some differences between pH 2 and pH 3 and 4. For S/L>2 (i.e., S/L = 10 and 20) and pH 3 and 4, the $\Delta C_{Al}/\Delta C_{Si}$ ratio grew towards stoichiometry but did not achieve it within the experimental duration (Figures 3.5d and 3.6d). The aluminum trend is slightly different over the pH range, indicating that Al may undergo some sorption processes.

When $C_{i,inp}$ and/or $C_{j,inp} > 0$ (Table 3.1), at pH 2, the variation of the $\Delta C_{Al}/\Delta C_{Si}$ and $\Delta C_{Mg}/\Delta C_{Si}$ ratios with time indicated a reasonable stoichiometric steady-state release of Si, Al and Mg (Figure 3.8c,d). At pH 3 and 4, the ΔC_{Al} showed a reduction of the Al deficit with time (Figures 3.9c and 3.10c). The $\Delta C_{Mg}/\Delta C_{Si}$ ratio tended to show preferential release of Mg over Si (Figures 3.9d and 3.10d).

3.4.5 Mechanism of K-montmorillonite dissolution

Figure 3.15 shows both the experimental and numerical variation in concentration of Si, Mg and Al versus time in the representative experiment Sm-SL-20-3 (pH 3). The initially high concentration of Si and Mg is not matched numerically, and the steady state is reached after a few hundred hours instead of ≈ 1200 h. This behavior is expected from the simulation as K-montmorillonite was the only reaction that took place and, all particles of K-montmorillonite were of the same size (4 μm). Under these conditions, K-montmorillonite dissolution was stoichiometric (Al/Si = 0.39 and Mg/Si = 0.11 (not shown)).

It was possible to obtain a reasonable reproduction of the initially high and long release of Si and Mg by considering that dissolution of microparticles (size << 4 μm) with an amount that varied from 1.5 to 9 % of the initial mass of sample was taking place (Figure 3.16). This range coincides with the total dissolved mass of K-montmorillonite in the

experiments. Also, it must be considered that although the K-montmorilllonite flakes form aggregates of about 4 um, TEM images of the K-montmorillonite show that the aggregates are formed of particles of 0.3-0.5 um of about 10-100 nm of thickness (Rozalén et al., 2008). So the existence of microparticles is a firm explanation to account for the high release of Si and Mg. However, in general, the calculated release of Si was overestimated (Figure 3.16a,b), the release of Mg was reasonably matched (Figure 3.16a,b) and there was always an experimental deficit in Al.

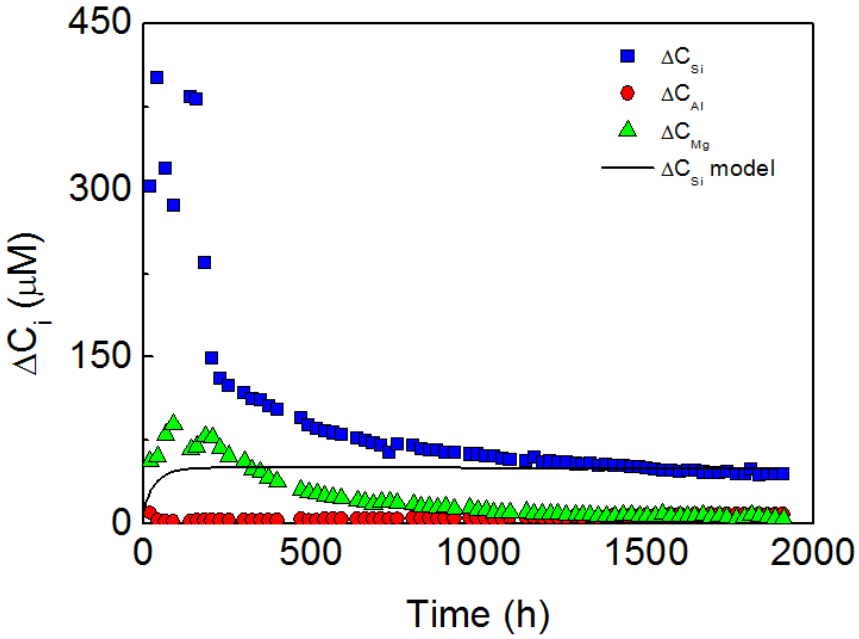

Figure 3.15. Experimental (symbols) and numerical (solid line) variation in ΔC_{Si}, ΔC_{Mg} and ΔC_{Al} versus time in experiment Sm-SL-20-3. Numerical variation is only shown for ΔC_{Si} concentration.

A preferential dissolution of fine-grained particles was observed by (Rozalén et al., 2008) during montmorillonite dissolution. Metz et al. (2005b) suggested that, during the first stage of montmorillonite dissolution, a Si-rich phase (i.e., ultra-fine amorphous silica particles) dissolve faster than the smectite. In the current experiments, both phenomena could account for the high variation in the experimental Si concentration and the numerical Si overestimation.

The simulations also show an initial increase in pH (Figure 3.17).

Regarding Mg, preferential release of Mg at both the initial stage and steady state during smectite and illite dissolution was reported in previous studies (Cama et al., 2000; Metz et al., 2005a; Golubev et al., 2006; Rozalén et al., 2008; Bibi et al., 2011; Marty et al., 2011).

The simulations show that a good match of experimental Mg leads to significant overestimation of Si release, indicating that the high Mg release is likely caused by a preferential Mg release.

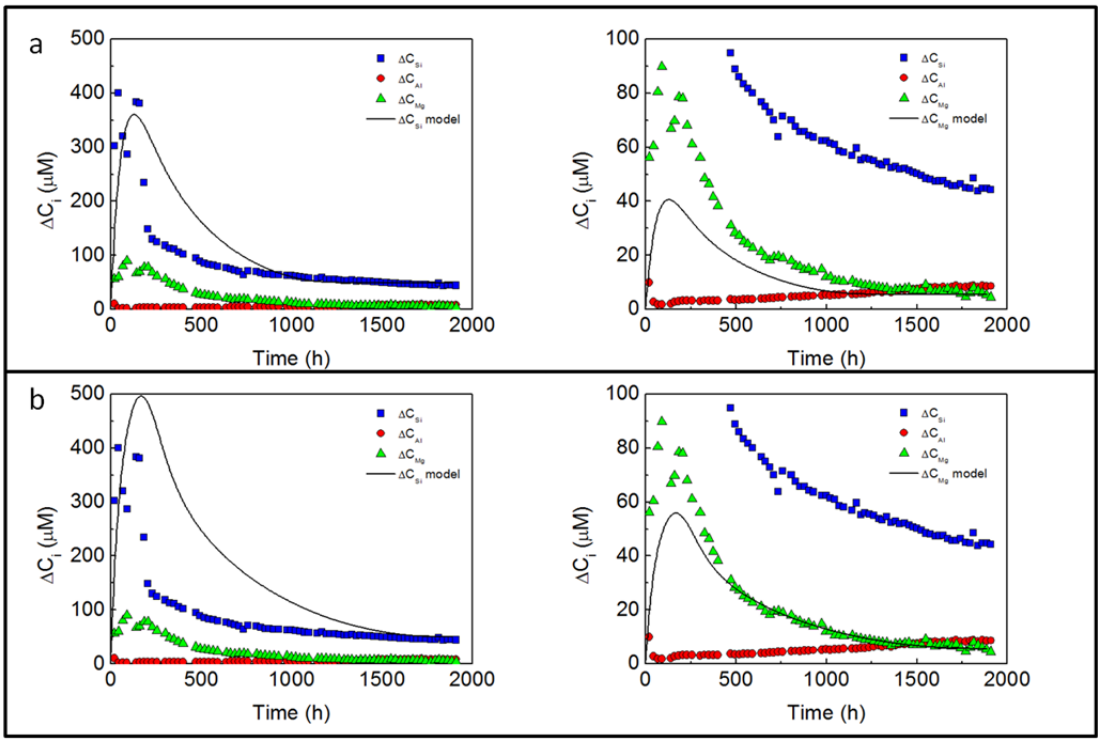

Figure 3.16. Experimental (symbols) and numerical (solid line) variation in ΔC_{Si}, ΔC_{Mg} and ΔC_{Al} versus time in experiment Sm-SL-20-3: (a) reasonable reproduction of the experimental Si release (left) implies underestimation of Mg (right) and (b) reasonable reproduction of Mg release (right) implies numerical overestimation of the experimental Si release (left).

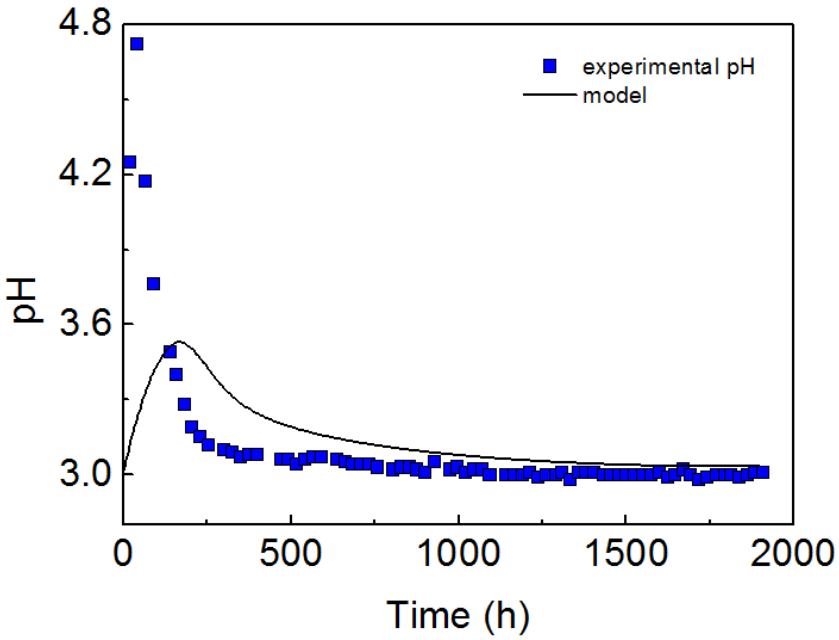

Figure 3.17. Experimental (symbols) and numerical (solid line) variation in pH versus time in experiment Sm-SL-20-3.

Golubev et al. (2006) and Rozalén et al. (2008) suggested that cation-proton exchange reactions are behind the excess of Mg over Si concentration during montmorillonite dissolution. Oelkers et al. (2009) identified metal-proton exchange (leaching) as a proton consuming reaction, with replacement of metal cation to protons during dissolution of multi-oxides and silicates. Leaching processes during dissolution of ino- and tectosilicates lead to formation of a thin layer enriched in silica (Petit et al., 1990; Banfield et al., 1995; Hellmann, 1997; Ferrage et al., 2005). In the case of phyllosilicate dissolution, Kaviratna and Pinnavaia (1994) studied acid hydrolysis of phlogopite and fluorohectorite in presence of high concentration of HCl (0.5-5 mol L^{-1}). While phlogopite hydrolyzed mainly by proton attack at the edges, the hydrolysis of fluorohectorite (Mg-Li smectite) occurred by both proton attack at the edges and gallery access. The latter mechanism involves ion exchange, Mg^{2+} for H^{+}, at the ditrigonal cavity of the basal surface.

Given that K concentration is 0.01 mol L^{-1} in all the experiments, the modeling of the results was performed by taking into account the Mg^{2+}-K^{+} exchange (Figure 3.18). The inclusion of the cation exchange reaction improved the match between the fitting and experimental data (Fig. 3.18b,c).

Also, Oelkers (2001) and Bibi et al. (2011) pointed out the fast initial release of Mg could be associated with the lower bond energy of the Mg-O or Al-O compared with Si-O. If

breaking of metal-oxygen bonds of di and trivalent cations is easier than Si-O bond, preferential release of Al should also be observed at least during the first stage of dissolution. However, in the current experiments, Al concentration increased only initially and thereafter reached a value that was lower than the stoichiometric one. Only in a few experiments performed at pH of 2, 3 and 4 the Al release was higher than the stoichiometric one (e.g. Figures 3.5 and 3.9). The observed Al deficit cannot be accounted with only K-montmorillonite dissolution. Precipitation of Al-bearing phases could be causing the Al deficit. However, as the output solutions were undersaturated with respect to Al-bearing phases (Table 3.2), these reactions were ruled out. Metz at al. (2005a) argued that an initially slow release of Al from smectite dissolution was caused by coating or cementation of the smectite aggregates by amorphous silica. When the aggregates fall apart, as the faster dissolved silica disappears, more smectite surface would be exposed, leading to an increase in dissolution rate. Since the authors did not observe Al deficit at pH 2 and 50 °C, re-adsorption of Al due to ion exchange and/or surface complexation was discarded. However, Al adsorption on silicate surface was reported in other studies (Charlet et al., 1993; Zysset and Schindler, 1996; Amram and Ganor, 2005; Oelkers et al., 2009). Zysset and Schindler (1996) found adsorption of Al^{3+} by ion exchange at pH<3.5 and by surface complexation on amphoteric hydroxyl group at pH>3.5 with 0.03 M ionic strength. Amram and Ganor (2005) observed essencially the same behaviour but ion exchange was significant only below pH 1.5.

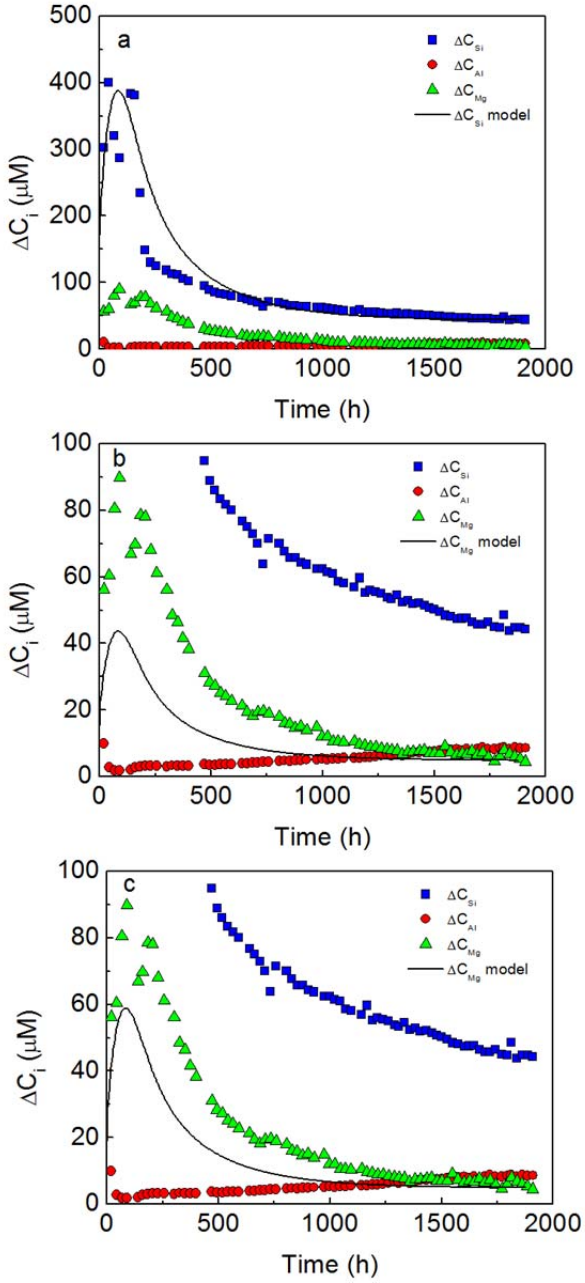

Figure 3.18. Experimental (symbols) and numerical (solid line) variation in ΔC_{Si}, ΔC_{Mg} and ΔC_{Al} versus time in experiment Sm-SL-20-3: a) reasonable match between numerical and experimental variations in ΔC_{Si}; b) numerical variation in ΔC_{Mg} and c) the numerical variation in ΔC_{Mg} is closer to the experimental one when the Mg^{2+}-K^{+} exchange reaction was taken into account.

To examine whether the effect of Al adsorption onto the K-montmorillonite is as a plausible mechanism to account for the observed Al deficit, modeling of the results was first performed considering the surface complexation model (Figure 3.19). The modeling results showed that dissolution of K-montmorillonite microparticles would be responsible for a high Al release (Figure 3.19a), and Al adsorption would occur during the first hours of the

experiment (Figure 3.19b), being thus to unable reproduce the long and systematic Al deficit. Also, Al adsorption would slightly diminish the pH (Figure 3.19c).

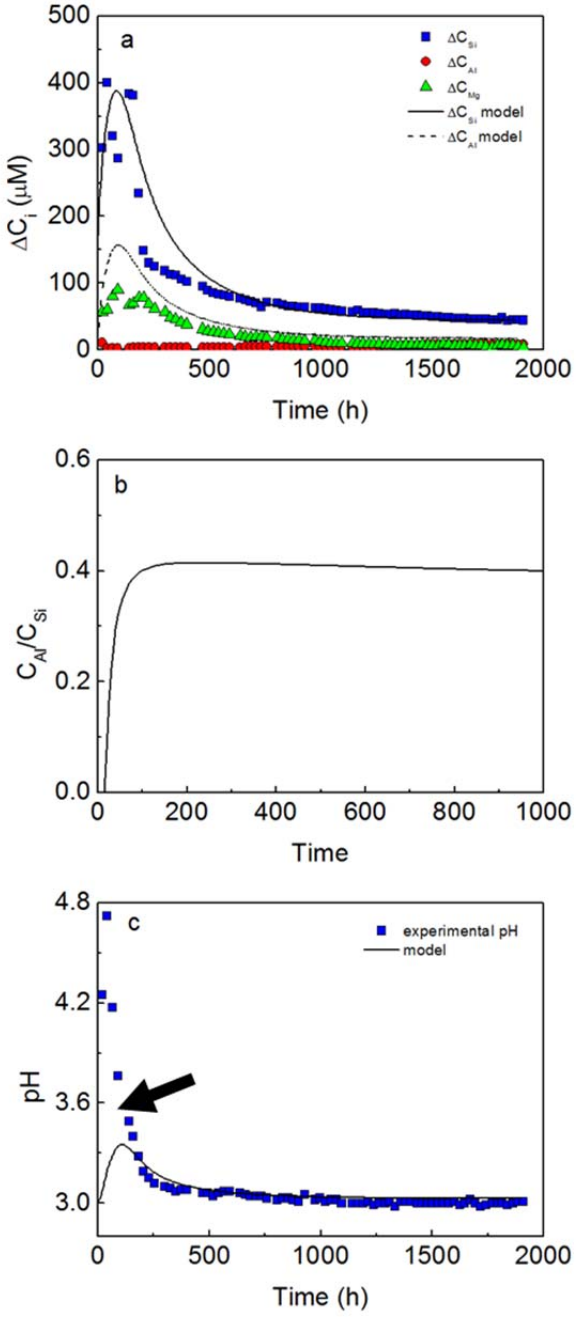

Figure 3.19. Experimental (symbols) and numerical (solid line) variation in ΔC_{Si}, ΔC_{Mg}, and ΔC_{Al}, C_{Al}/C_{Si} ratio and pH versus time in experiment Sm-SL-20-3: (a) the numerical variation in ΔC_{Al} is higher than the experimental Al release; (b) Al^{3+} adsorption takes only place for ≈ 100 h (C_{Al}/C_{Si} < 0.4) and (c) pH diminishes from 3.5 (arrow) to 3.3 at the maximum associated to Al^{3+} adsorption.

Putnis and Putnis (2007) suggested that dissolution–reprecipitation is a universal mechanism controlling fluid–mineral interactions. In this context, Al concentrations below

stoichiometry could be due to secondary reaction after Al release from the structure. Hellman et al. (2012) proposed the existence of a chemical weathering continuum based solely on the interfacial dissolution–reprecipitation mechanism. It was postulated that mineral dissolution is always stoichiometric but it is coupled to precipitation of an amorphous silica-rich surface layer whose dissolution depended on bulk conditions. Although the model was derived from feldspar dissolution experiments, it could apply to phyllosilicate dissolution.

In general, dissolution rates of silicate minerals are obtained from Si release since the rate limiting step in silicate dissolution is the breakdown of bridging oxygen bonds and the detachment of Si atoms induced by the previous detachment of octahedral cations (Huertas et al., 1999; Bickmore et al., 2001; Oelkers, 2001; Rozalén et al., 2009a). Moreover, in the case of mica dissolution, Kalinowski and Schweda (1996) attributed to tetrahedral sheet a higher weathering stability than to octahedral sheet.

Although in this study, the steady-state smectite dissolution rates were based on the release of Si (R_{Si}), Al (R_{Al}) and Mg (R_{Mg}) (Table 3.1), taking into account the above it was considered that R_{Si} was a good proxy for the K-montmorillonite dissolution rate.

3.5 K-montmorillonite dissolution rate: effect of pH and solution saturation state (ΔG_r)

Figure 3.20 shows the variation in R_{Si} as a function of pH. From the one hand, R_{Si} decreased by increasing pH (Figure 3.20a) and, on the other hand, R_{Si} also varied at fixed pH values as R_{Si} was obtained at different solution saturation state (ΔG_r; Figure 3.20c-e). The R_{Si} values considered to be further from equilibrium at pH 2, 3 and 4 (Figure 3.20c-e) were selected to calculate the R_{Si}-pH dependence (Figure 3.20b), assuming that the K-montmorillonite dissolution rate was proportional to a fractional power of the hydrogen ion activity:

$$R_{Si} = k \cdot a_{H^+}^{n_{H^+}} \quad 3.17$$

where k is a proportionality constant, $a_{H+}$is the proton activity in solution and n_{H+} is the proton reaction order. Accordingly:

$$R_{Si}(mol\ g^{-1}\ s^{-1}) = 10^{9.74\pm0.07} \cdot a_{H^+}^{0.58\pm0.01} \quad 3.18$$

The 0.58 value for n_{H+} was slightly higher than the 0.40 value obtained by Rozalén et al. (2008. Nonetheless, the R_{Si} values obtained at pH 2 and pH 4 were the same within error in both studies.

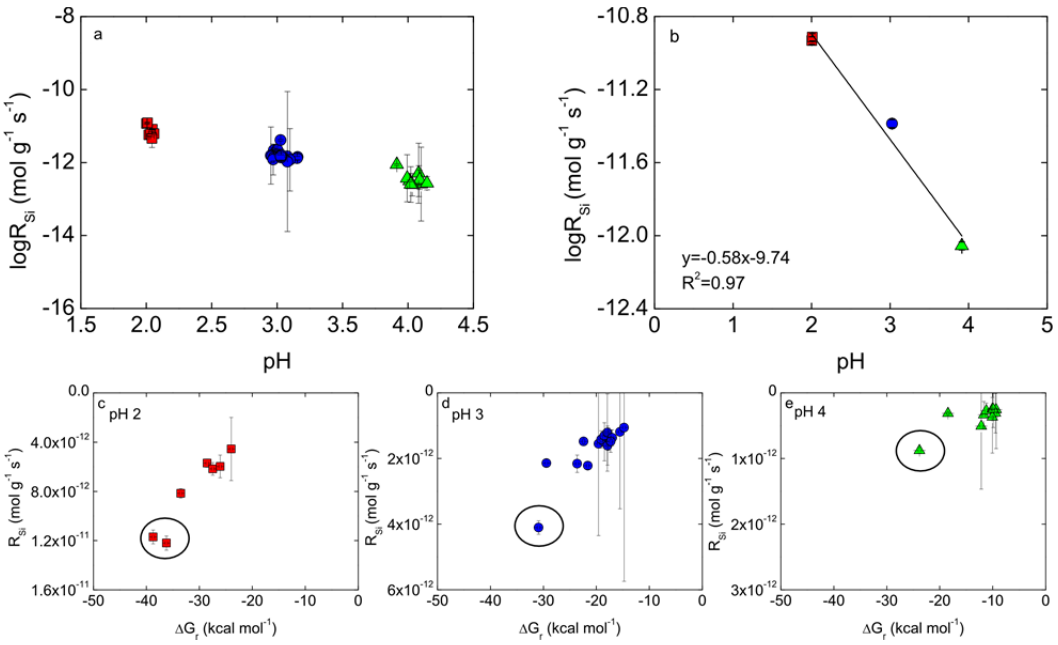

Figure 3.20. Variation in log R_{Si} (mol g^{-1} s^{-1}) versus pH (a,b) and ΔG_r (c-e). Ellipses show the rate values taken to calculate the R_{Si}-pH dependence (see text).

Once the pH effect on the K-montmorillonite dissolution rate was known, it was possible to separate the pH effect from the ΔG_r effect. By doing so the R_{Si}-ΔG_r dependency could be estimated properly. Corrected R'_{Si} values were obtained as:

$$R'_{Si} = R_{Si}/a_{H^+}^{0.58} \qquad 3.19$$

Then R'_{Si} was plotted as a function of ΔG_r (Figure 3.21), where R'_{Si} increased by decreasing ΔG_r. Based on Eq. (3.5), the K-montmorillonite dissolution rate dependence on ΔG_r was calculated as:

$$R'_{Si} = k \cdot f(\Delta G_r) \qquad 3.20$$

where k was $10^{-9.85\pm0.07}$ (mol g^{-1} s^{-1}) and m and n were $3.84\cdot10^{-4}$ and 2.13, respectively. The solid line in Figure 3.21 shows the calculated R_{Si} variation as a function of ΔG_r. The resulting expression:

$$R = 2 \cdot 10^{-10} \cdot \left(1 - exp\left(-3.8 \times 10^{-4} \cdot \left(\frac{|\Delta G_r|}{RT}\right)^{2.13}\right)\right) \quad 3.21$$

shows that the dissolution plateau could be reach at $\Delta G_r \approx$ -40 kcal·mol^{-1}.

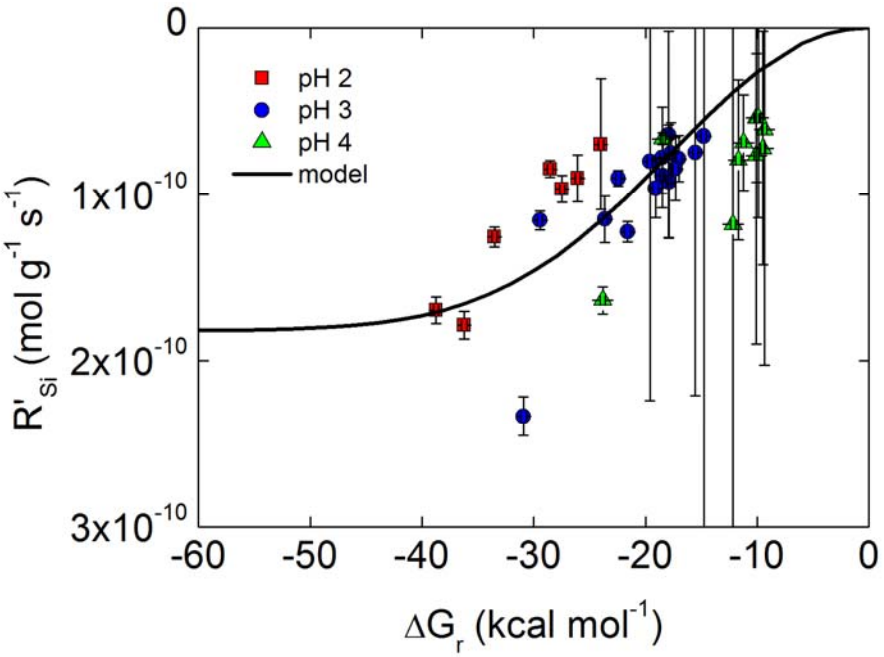

Figure 3.21. Variation in log R'_{Si} (mol g^{-1} s^{-1}) as a function of deviation from equilibrium, ΔG_r. Rates were obtained at pH 2, 3 and 4.The solid line represent the calculated R'_{Si} values (see text).

Figure 3.22 compares the shape of $f(\Delta G_r)$ obtained in this study with those of previous studies in which the ΔG_r-*R* dependency was reported for the dissolution rate of different montmorillonites under different pH and temperature (Table 3.3); pH 8.8 and 80 °C (Cama et al., 2000); pH 3 and 50 °C (Metz, 2001) and pH 9 and 25 °C (Marty et al., 2011). Interestingly, Zhang et al. (2015) obtained a similar ΔG_r shape for chlorite dissolution at the pH range from 3 to 7.5 and 100 °C (Table 3.3). Note that as pointed out by Cama et al. (2000) the empirical values of m and n in Eq. (3.5) are not unique. It is important to highlight that even though in this study, the rate-ΔG_r dependence was obtained at acid pH, it shows that is similar for the entire range of pH (i.e., pH from 0 to 14).

Therefore, a general rate law that accounts for both the pH and ΔG_r effects on the K-montmorillonite dissolution rate at acid pH is of the form:

$$R(mol\ g^{-1}\ s^{-1}) = 10^{9.74\pm0.07} \cdot a_{H^+}^{0.58\pm0.01} \cdot \left(1 - exp\left(-3.8 \times 10^{-4} \cdot \left(\frac{|\Delta G_r|}{RT}\right)^{2.13}\right)\right) \qquad 3.22$$

A comparison between the rates measured in this study with the modeled ones using Eq.(3.22) shows good agreement (Figure 3.23a-d).

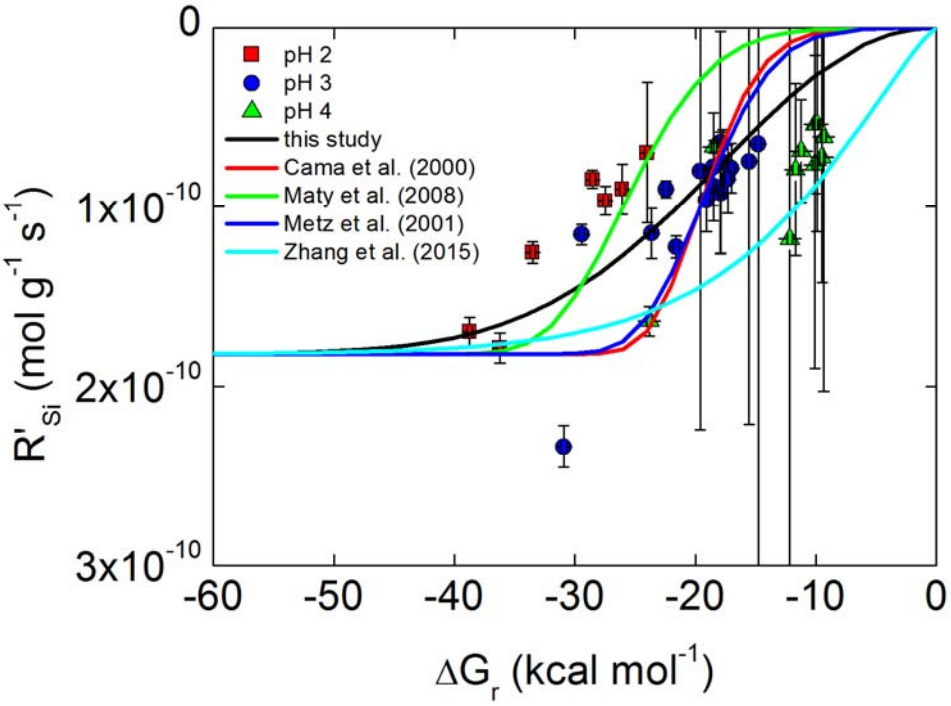

Figure 3.22. Variation in log R'_{Si} (mol g^{-1} s^{-1}) as a function of ΔG_r. Rates were obtained at pH 2, 3 and 4.The solid lines represent the calculated R'_{Si} values based on the rate laws proposed in this and previous studies (see text).

Table 3.3 Empirical *m* and *n* coefficients in Eq. (3.5) and *k* values obtained in the present and previous studies. Experimental conditions in which the values were obtained are also given.

Phyllosilicate	*m*	*n*	pH	T (°C)	Reference
K-montmorillonite	-3.80×10^{-4}	2.13	2-4	25	this study
Cabo de Gata smectite	-6.00×10^{-10}	6.00	8.8	80	Cama et al (2000)
Synthetic smectite	-8.23×10^{-11}	5.47	9	50	Marty et al. (2008)
SAz-1 smectite	-2.00×10^{-8}	5.00	3	50	Metz (2001)
CCa-2 chlorite	-1.68×10^{-2}	1.30	3-8	100	Zhang et al. (2015)

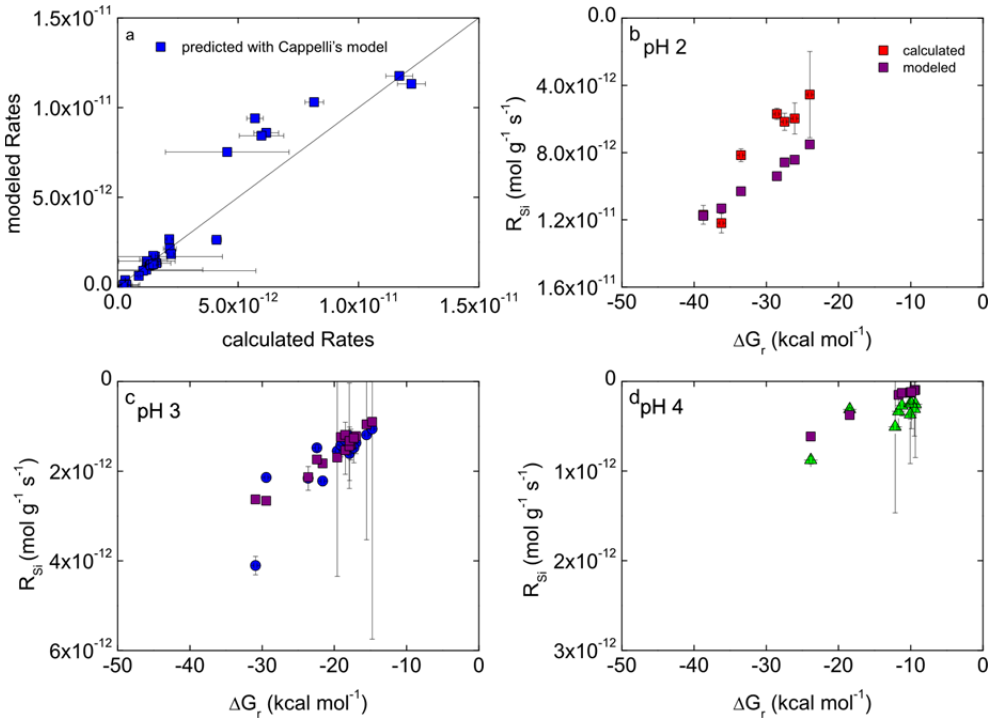

Figure 3.23. Comparison between measured and modeled R_{Si} rates using Eq. (3.22): a) all pH values and b) at pH of 2, 3 and 4.

3.6 Summary and conclusions

Dissolution of K-montmorillonite was studied at 25 °C and acidic pH using well mixed flow-through experiments. From the aqueous chemistry variation, the smectite dissolution congruency and the effects that the pH and degree of undersaturation exerted on the dissolution rate were examined. To this end, separation of the effects of pH and degree of undersaturation was performed.

During the experiments, microparticles dissolution controlled the overall process until their total consumption. Cation exchange between octahedral Mg^{2+} and K^{+} was likely responsible for the preferential Mg release. The Al deficit could not be explained by precipitation of Al-bearing phases since the outflow samples were undersaturated with respect to them. Dissolution of microparticles would account for a high Al release and Al adsorption would occur during the first hours of the experiment, being thus unable to reproduce the long and systematic Al deficit. With time, K-montmorillonite dissolution was characterized by the achievement of a steady-state release of Si and Mg, together with a deficit in Al. The average Mg/Si ratio in outflow samples is in good agreement with the molar ratio in the mineral, indicating stoichiometric dissolution of K-montmorillonite.

K-montmorillonite dissolution rates were analysed and fitted as functions of pH and chemical affinity (ΔG_r). Only the data that were under far from equilibrium conditions are used in fitting the relationship between dissolution rate and pH so as to ensure that the near-equilibrium (ΔG_r) effects were not included.

The measured dissolution rates showed that R_{Si} increased by decreasing pH and by decreasing ΔG_r and R_{Si} could be independent on ΔG_r (dissolution plateau) at ΔG_r < -40 kcal mol^{-1}. The K-montmorillonite rate as a function of pH and chemical affinity (ΔG_r) at 25 °C can be fit reasonably well with an empirical nonlinear rate law within the framework of transition state theory as shown by Cama et al. (2000)

$$R(mol\ g^{-1}\ s^{-1}) = 10^{9.74\pm0.07} \cdot a_{H^+}^{0.58\pm0.01} \cdot \left(1 - exp\left(-3.8 \times 10^{-4} \cdot \left(\frac{|\Delta G_r|}{RT}\right)^{2.13}\right)\right)$$

The K-montmorillonite dissolution rate varied as a function of the Gibbs free energy over a large range (-40 <ΔG_r < 0 kcal mol^{-1}). The shape of the $f(\Delta G_r)$ term is similar to those proposed for rate laws that account for dissolution of distinct montmorillonites obtained under different pH and temperature conditions (Cama et al., 2000; Metz, 2001; Marty et al., 2011) and that of chlorite disolution rate law (Zhang et al., 2015). This suggests that the obtained nonlinear $f(\Delta G_r)$ term could be extended to other phyllosilicate dissolution rate formulations.

4 MICA SURFACE REACTIVITY

Biotite and phlogopite were used to study the reactivity of mica in the acid pH range from 1 to 3 over the temperature range from 11.5 to 100 °C. The effect of the oxalic acid on the biotite dissolution rate and dissolution mechanism at pH from 1.2 to 2.2 was also investigated. Measurements of the reacted (001) basal surface of both mica minerals were performed by means of three microscopy techniques (LCM-DIM, VSI/PSI and AFM).

Oxalic acid, ubiquitous in soils and sediments, was chosen as a representative organic ligand because its well-known catalytic effect on silicate dissolution rates (Declercq et al.; Song and Huang, 1988; Barman et al., 1992; Wieland and Stumm, 1992; Welch and Ullman, 1993; Varadachari et al., 1994; Prapaipong et al., 1999; Oelkers and Gislason, 2001; Cheah et al., 2003; Johnson et al., 2004; Persson and Axe, 2005; Pokrovsky et al., 2005; Wang et al., 2005; Cama and Ganor, 2006; Golubev et al., 2006; Tu et al., 2007; Olsen and Rimstidt, 2008; Haward et al., 2011; Rozalén and Huertas, 2013; Ramos et al., 2014).

The main aim is to improve our understanding of the kinetics and mechanisms of mica dissolution based on the morphological and topographical changes. Biotite good reflectivity makes this mineral highly suitable for optical microscopic observations. In turn, phlogopite was selected to compare its reactivity with that of biotite in order to understand better the 2:1 phyllosilicate dissolution in acidic pH.

The obtained experimental results together with the kinetic data obtained by flow-through experiments, yield an enhanced overview of 2:1 phyllosilicate dissolution.

4.1 Biotite dissolution in the absence of oxalic acid

4.1.1 Dissolution mechanisms of the biotite (001) cleavage surface

In situ exploration of broad regions (0.3-2.0 mm^2) of the reacting biotite (001) surface at pH 1 was carried out using LCM-DIM. The freshly cleaved biotite (001) surface was a flat basal surface composed of terraces with variable extension and height (Figure 4.1a). Edges of the (001) cleavage planes did not show preferential crystallographic directions.

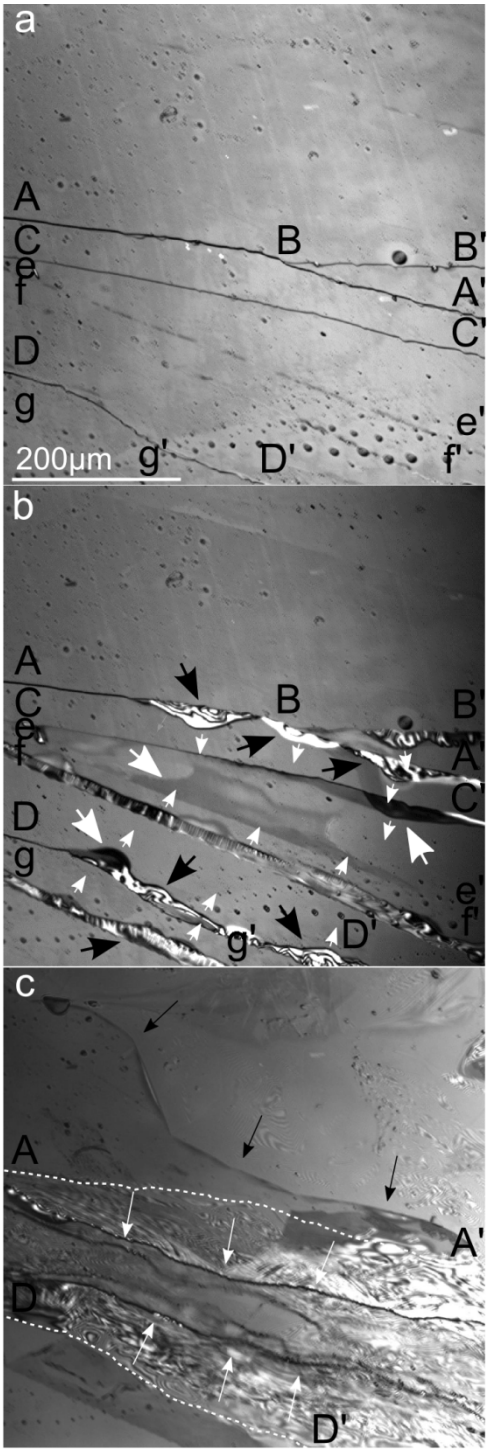

Figure 4.1. LCM-DIM images of biotite (001) cleavage surface: pristine (a), reacted for 53 min (b) and for ~ 6 h (c) at pH 1 and 50 °C. Capital letters and lower case letters indicate high and low step edges, respectively. Dissolution of higher steps at early stages of the reaction moves non-homogeneously inward from the edges. The spherical structures in (a) are air bubbles absorbed on the surface. Large white and black arrows in (b) indicate swelling and peeling layers, respectively, while small white arrows indicate dissolution directions. During the first hour of reaction the steps do not retreat, suggesting some dissolution of the upper layers. As the reaction continues most of the steps disappear to leave altered areas. Two uniform reaction fronts remain after 6h (AA' and DD' in c). Dotted lines in (c) indicate the AA' and DD' step positions after 53 min; white arrows show dissolution directions, and black arrows indicate dissolution of a new low-step leaving fresh surface.

Surface changes were readily visible as the biotite surface was interacting with the solution. Since dissolution started the retreat of high steps (macrosteps) occurred rather irregularly along the edges. An example of the evolution of the macrosteps is illustrated in the images of Figure 4.1 (experiment B50-1-2, Table 2.2). After ~ 1 h at pH 1 and 50 °C (Figure 4.1b), alteration of the high steps is visible only on certain sections, along with a simultaneous spread of few layers. In the altered sections, peeling of upper layers (overexposed regions pointed out by black arrows in Fig. 4.1c) occurred as a result of layer swelling and consecutive break. The altered regions spread out with time, yielding a wide degraded region (Figure 4.1c). Other high and lower steps disappeared due to either total dissolution of a terrace or coalescence of the main steps.

In general, the retreat of step edges was approximately normal to the terrace edges, irrespective of the experimental temperature (Figure 4.1c and Figure 4.2). Figure 4.2a,b shows edge retreat normal to the terraces (f1 and f2) after 5 h of dissolution at pH 1 and 70 °C (experiment B70-1-1, Table 2.2). Likewise, the retreat of steps with relatively low height yielded freshly new basal biotite surface (Figure 4.2b). Reaction fronts moved at different velocities. Similarly, some upper layers moved faster than lower ones, promoting the formation of new step edges (Figure 4.2c).

Therefore, dissolution of the (001) cleavage surface at pH 1 was mainly controlled by step retreat and contraction and breaking of layers promoted swelling and peeling of layers along macrosteps (Figure 4.3a,b). Although dissolution of surface edges dominated the biotite dissolution reaction, dissolution at the basal plane also occurred (Figure 4.3c,d). Indeed, AFM exploration of the basal surface altered at pH 1 and 70 °C showed uniform distribution of etch pits (diameter of ≈ 20-100 nm) with a depth of 3 nm (~3 mica layers; Figure 4.4a,b), indicating that the biotite basal surface contributes to the overall dissolution.

Ex situ VSI and PSI examination of the (001) cleavage surface confirmed that step retreat was also the main biotite dissolution mechanism in a broader range of pH (1-3) and temperature (25-80 °C). Existence of reaction fronts, increase in surface roughness, basal plane reactivity and swelling and peeling of the biotite (001) surface along high steps were observed (Figure 4.5a-c; experiments B64-25-1, B30-70-1, Table 2.3). The *ex situ* images also showed the presence of dissolution channels without preferential orientations (Figure 4.5c,d experiments B30-70-1, B47-70-3, Table 2.3; see also Figure 8.1a-Appendix II). Formation of this type of dissolution feature implies a generation of new reaction fronts from which dissolution took place, leading to an increase in the surface roughness.

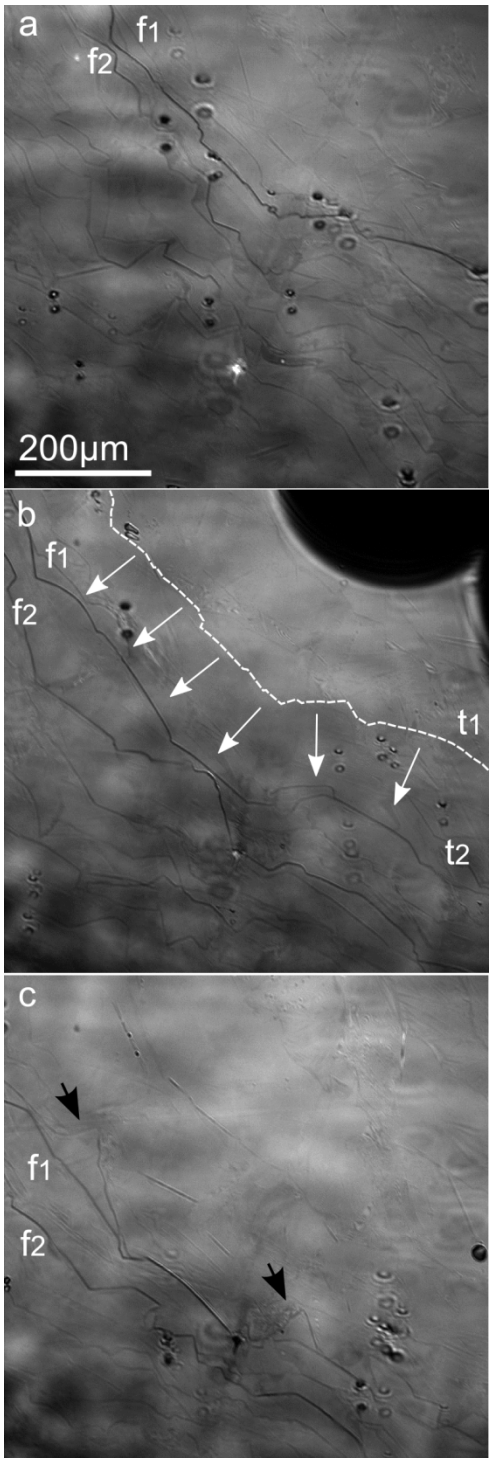

Figure 4.2. LCM-DIM images of reacted biotite (001) cleavage surface (a) after ~ 5 h (t1), (b) 5 h and 30 min (t2) and (c) 5 h and 46 min at pH 1 and 70 °C. In (b) the dotted line indicates the previous position of the main edge in (a). White arrows indicate retreat direction. Black arrows in (c) indicate areas where upper layers dissolved faster than the lower ones. The different distance between consecutive dissolution fronts for different time reaction (f1 and f2) is indicative of retreat fluctuation. The small dark spherical structures and the large dark area in the upper right corner in (b) are air bubbles; the pale elliptic structures are dust particles derived from the objective lens.

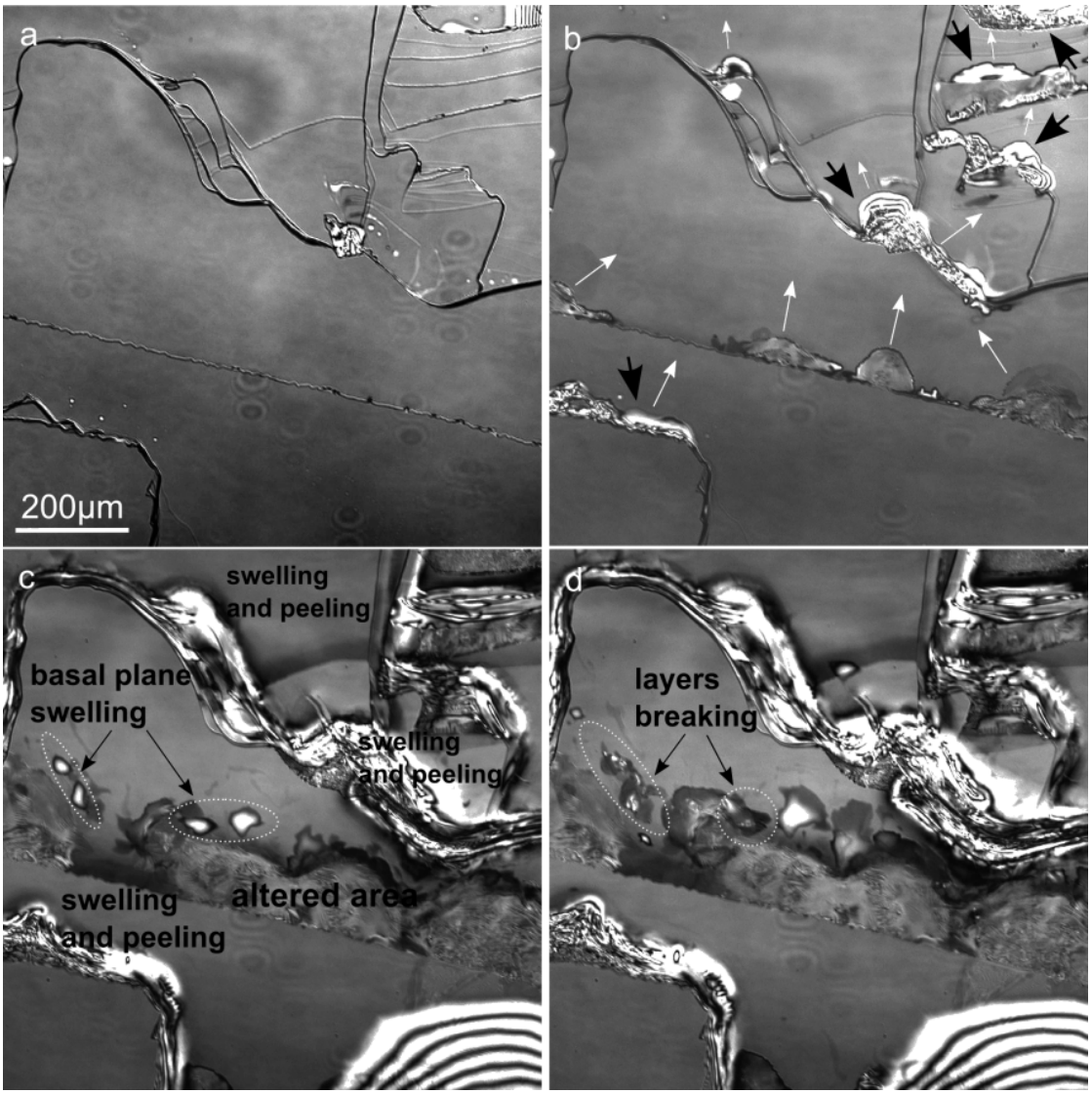

Figure 4.3. LCM-DIM images of biotite (001) cleavage surface: pristine (a) and after reaction at pH 1 and 11.5°C for 21 h (b), ~5 d (c) and ~6 d (d). Note the presence of high step edges (dark outlines). Dissolution started irregularly along the edges (white arrows in (b) indicate dissolution direction). Large black arrows indicate over lighted areas (regions with PMT saturation) where roughening and peeling of layers occur. A time-lapse movie of the last 42 h of the experiment is available.

VSI examination of the basal surface reacted at pH 3 showed the existence of small round-shaped etch pits with a diameter of ~3-4 μm and depth of ~20-50 nm on localized areas (Figure 4.5d). Therefore, although the formation of etch pits on the biotite basal surface contributes to the overall dissolution, solutions edge retreat predominates in HNO_3 (see section 4.4).

4.1.2 Biotite dissolution rate

Horizontal retreat rates (R_r) of the (001) cleavage biotite dissolution were obtained at pH 1 and 25-70°C using LCM-DIM sequential images (Table 4.1). It was inferred that higher steps retreated slower than the lower ones. According to (Aldushin et al., 2006), R_r represents dissolution of few layers. For example, at pH 1 and 50 °C (B50-1-2, Figure 4.1), the retreat rate of the higher steps was 5.4×10^{-3} μm s^{-1}, whereas that of the lower steps was 2.6×10^{-2} μm s^{-1}. R_r increased by increasing temperature (Table 4.1).

From the VSI/ PSI topographic measurements the biotite dissolution rate (R_{diss}) was obtained at pH 1, 2 and 3 and 25-80 °C using Eq (2.8) (Table 4.2). Note that variation in step height with time was measured at different regions of the basal surface in each experiment. In the batch experiments, biotite dissolution rates (R_j) based on the release of Si, Al, Mg, K and Fe (structural cations) into solutions were calculated using Eq. (2.11) (Table 4.3). As expected for the variation in dissolution rates with pH and temperature, R_j increases with temperature and decreases with pH. R_{Si} and R_{Al} were the same within the 20 % uncertainty, whereas the variability among R_{Mg}, R_K and R_{Fe} was in some cases up to 60 %.

Based on (1) variation in R_r with temperature at pH 1, (2) variation in R_{diss} with temperature at pH 1, 2 and 3 and (3) variation in R_{Si} and R_{Al} with temperature, also at pH 1, 2 and 3, the apparent activation energy of the overall reaction was calculated according to the Arrhenius law (Figure 4.6a,c):

$$R_{diss} = A \cdot e^{-\frac{E_a}{RT}} \qquad 4.1$$

where A is the pre-exponential factor, E_a is the apparent activation energy, R is the gas constant and T is the absolute temperature. Table 4.4 lists the apparent activation energy values than range from 31 to 67 kJ mol^{-1}.

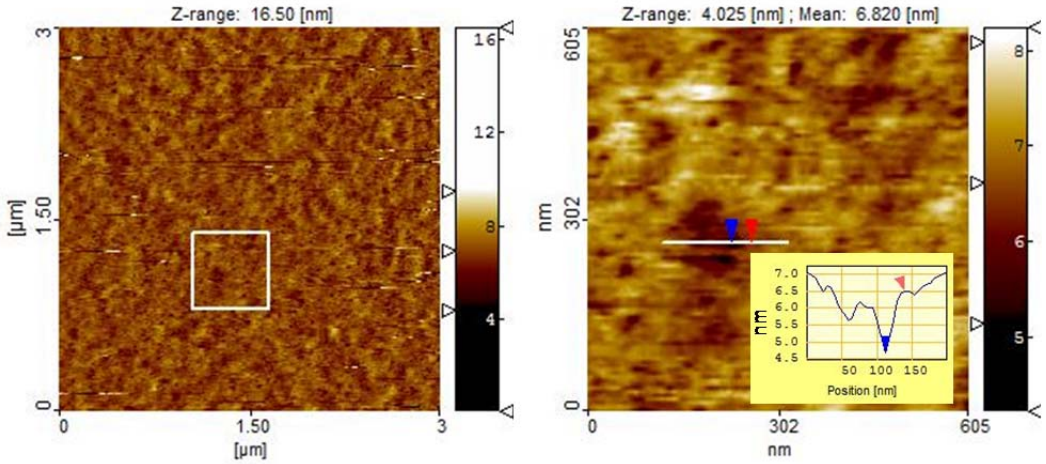

Figure 4.4. AFM images of biotite (001) surface after reaction at pH 1 and 70°C for 72h: (a) etch pits (dark spots) formed and distributed uniformly over the (001) surface and (b) detailed image of the squared region in (a). Etch pits are ≈ 20-100 nm wide and ≈3 nm deep.

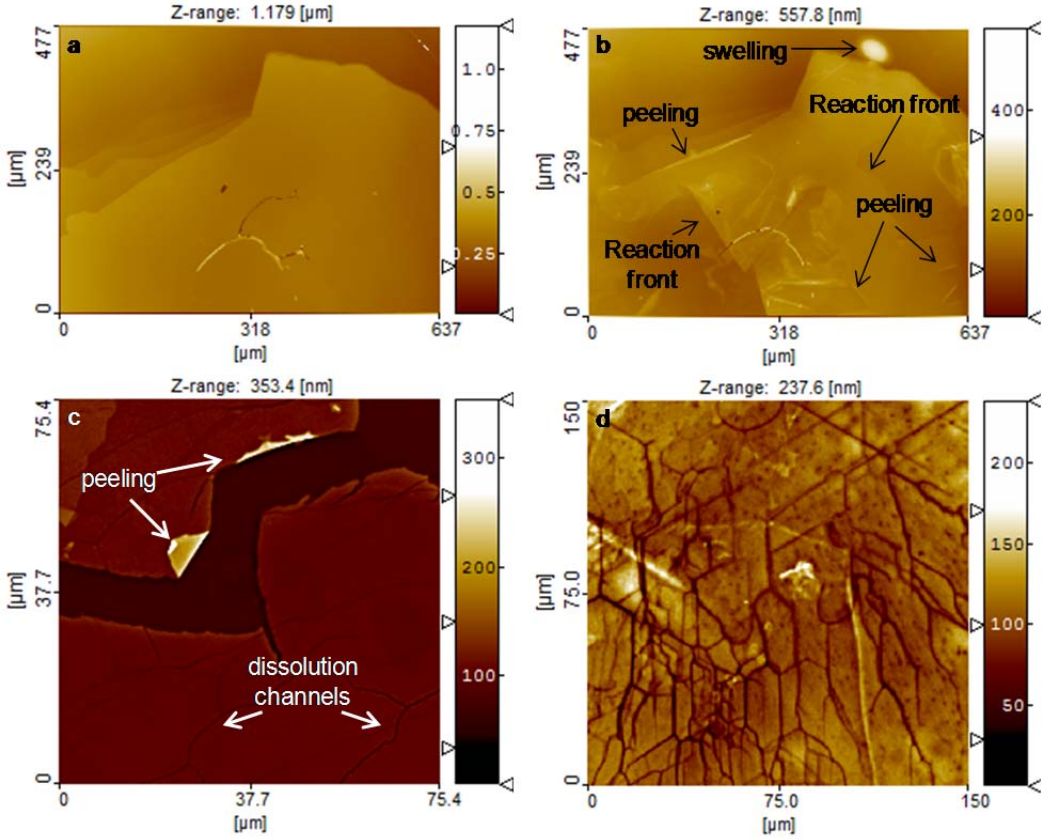

Figure 4.5. PSI (a, b) and VSI (c, d) images of biotite (001) surface: pristine surface (a) and after reaction at 25°C for 48 h at pH 1 (b) and 70 °C for 248 h at pH 1 (c) and 72h at pH 3 (d) respectively. Step edge retreat, swelling of basal plane and peeling of edge surface are shown (b-d). At 70 °C dissolution channel form all over basal plane (c, b) and at pH 3 little round shaped etch pits formed.

Table 4.1. Horizontal-retreat rates calculated by LCM-DIM from the horizontal surface retreat of the biotite lower steps at different temperature in HNO_3 acid solution.

T (ºC)	R_r (μms^{-1})
11.5	7.5×10^{-4}
25	3.8×10^{-3}
40	1.9×10^{-2}
50	2.6×10^{-2}
70	6.2×10^{-2}

Table 4.2. Vertical dissolution rates calculated by VSI/PSI measurements of biotite reacted in HNO_3 acid solutions.

nitric acid 0.1M Experiment	T (°C)	R_{diss} (mol $g^{-1}s^{-1}$)
B13_25_1	25	9.4E-10
B10_40_1	40	4.0E-09
B8_50_1	50	6.7E-09
B30_70_1	70	2.6E-08
B59_80_1	80	8.1E-08
nitric acid 0.01M Experiment		
B12_25_2	25	5.1E-10
B21/25_40_2	40	1.3E-09
B6/26_50_2	50	2.8E-09
B66_70_2	70	1.1E-08
nitric acid 0.001M Experiment		
B23_25_3	25	1.8E-10
B24_40_3	40	4.1E-10
B47_70_3	70	2.0E-09

Table 4.3. Dissolution rates calculated from the cations released from biotite dissolution in HNO_3 acid solutions.

nitric acid 0.1M						
Experiment	T (°C)	R_{Si}	R_{Al}	R_{Mg}	R_{Fe}	R_K
B13_25_1	25	7.9E-11	7.8E-11	8.7E-11	8.4E-11	8.8E-11
B10_40_1	40	1.9E-10	1.8E-10	2.1E-10	2.0E-10	2.1E-10
B8_50_1	50	4.2E-10	3.9E-10	1.6E-10	5.0E-10	5.9E-10
B30_70_1	70	1.6E-09	1.6E-09	5.5E-10	1.5E-09	7.0E-10
B59_80_1	80	-	-	-	-	-
nitric acid 0.01M						
B12_25_2	25	2.7E-11	3.5E-11	2.8E-11	3.7E-11	3.7E-11
B21_40_2	40	4.6E-11	4.3E-11	3.1E-11	5.7E-11	3.1E-11
B25_40_2	40	5.7E-11	8.8E-11	5.4E-11	8.1E-11	1.4E-10
B26_50_2	50	1.1E-10	1.4E-10	1.6E-10	4.1E-11	6.3E-11
B6_50_2	50	1.8E-10	1.9E-10	2.0E-10	2.4E-10	2.3E-10
B66_70_2	70	1.1E-10	-	-	-	-
B29_70_2	70	2.8E-10	-	2.0E-11	2.2E-10	5.8E-12
nitric acid 0.001M						
B23_25_3	25	8.1E-12	8.8E-12	3.3E-11	9.5E-12	2.3E-11
B24_40_3	40	2.6E-11	3.1E-11	2.5E-11	2.7E-11	3.7E-11
B47_70_3	70	4.5E-11	-	6.1E-11	-	1.2E-11

dissolution rates in mol g^{-1} s^{-1}

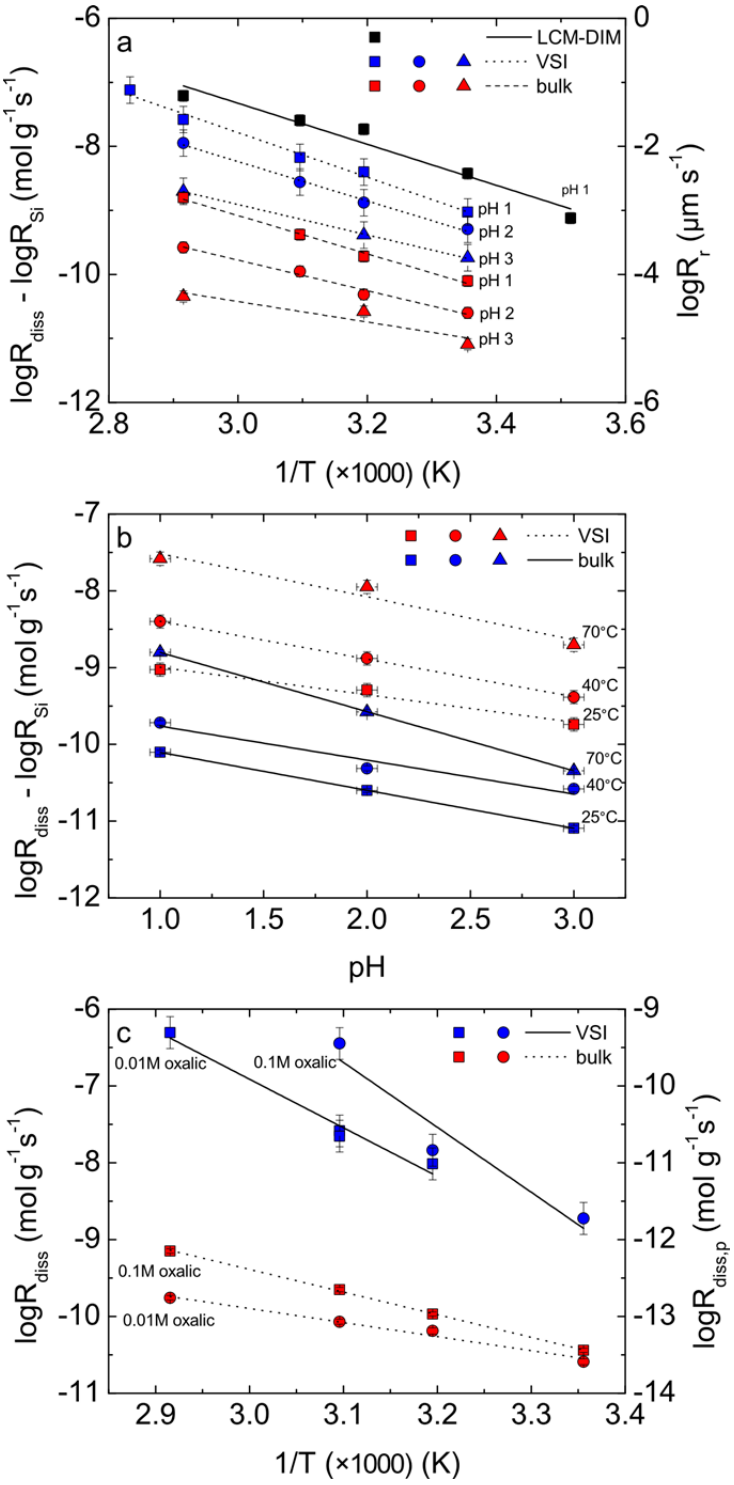

Figure 4.6. (a) Arrhenius plot calculated from: LCM-DIM measurement of horizontal biotite step retreat rates (R_r) at pH 1 and 11.5 to 70 °C (solid line); VSI and PSI measurement of normal biotite dissolution rates (R_{diss}) at pH 1-3 and 25 to 80 °C (dotted lines) and bulk solution dissolution rates (R_{Si}) at pH 1-3 and 25 to 70 °C (dashed lines). (b) Biotite normal dissolution rate dependence on pH: VSI/PSI dissolution rates (R_{diss}) (dotted lines) and bulk solution rates (R_{Si}) (dashed lines). (c) Arrhenius plots calculated from biotite dissolution rates based on bulk solution (R_{Si}) (solid lines) and loss of etch pit volume ($R_{diss,p}$) (dotted lines) in 0.01 and 0.1 mol L^{-1} oxalic acid and from 25 to 70 °C.

Taking into account that the estimated uncertainty, a reasonable agreement is found between the calculated E_a at pH 1 using LCM-DIM measurements (62 kJ mol^{-1}) and using VSI/PSI measurements (67 kJ mol^{-1}). In addition, little discrepancy exists between E_a obtained from the topographic measurements of the basal surface and the bulk dissolution. Overall, it is inferred that E_a decreases with pH as occurred with the montmorillonite dissolution rate as reported by Rozalén et al. (2009b).

Table 4.4. E_a values calculated from biotite R_r, R_{diss} and R_{Si} values; HNO_3 acid solution.

Expt.	E_a (kJ mol^{-1})	error %
LCDM-DIM	62	15
VSI-pH1	67	20
VSI-pH2	59	20
VSI-pH3	42	20
bulk-pH1	57	10
bulk-pH2	46	10
bulk-pH3	31	10

Based on the variation in R_{diss}, and in R_{Si} and R_{Al} with pH at 25-80 °C, the biotite dissolution rate-pH dependence was estimated assuming that the dissolution rate was proportional to a fractional power of the hydrogen ion activity (Figure 4.6b):

$$R_{diss} = k \cdot a_{H^+}^{n_{H^+}} and\ R_{Si} \approx\ R_{Al} = k \cdot a_{H^+}^{n_{H^+}} \quad 4.2$$

where k is a proportionality constant, a_{H+} is the proton activity in solution and n_{H+} is the proton reaction order. Based on R_{diss}, n_{H+} varies between 0.36 at 25 °C to 0.56 at 70 °C, increasing by increasing temperature. Variation in R_{Si} and R_{Al} yielded similar n_{H+} values (0.49 at 25 °C and 0.43 at 40 °C), whereas a value of 0.8 was calculated at 70 °C.

Similar n_{H+} values at 25 °C to the ones obtained in this study were reported in two previous studies using biotite powder experiments. Acker and Bricker (1992) calculated a n_{H+} value of 0.34 for biotite dissolution at 22°C in a pH range of 3-7 and Malmström and Banwart (1997) obtained a little higher n_{H+} value (0.48) for the proton-catalysed biotite dissolution at 25 °C. The high value obtained here at 70 °C from the macroscopic measurement could be caused by the fact that R_{diss} at pH 3 was calculated based on only one point (B47-70-3, Table 4.3 and Table 8.1-Appendix II).

4.2 Biotite dissolution in the presence of oxalic acid

4.2.1 Dissolution mechanisms of the biotite (001) cleavage surface

Similar to biotite dissolution in HNO_3 solutions, in the presence of oxalic acid, biotite (001) surface dissolution was controlled by both step edge retreat and formation of etch pits (Figure 4.7). On the one hand, the edge retreat was non-uniform, resulting in fingering formation (Figure 4.7b,c), and on the other hand, etch pits formed uniformly all over the biotite basal surface (Figure 4.7d).

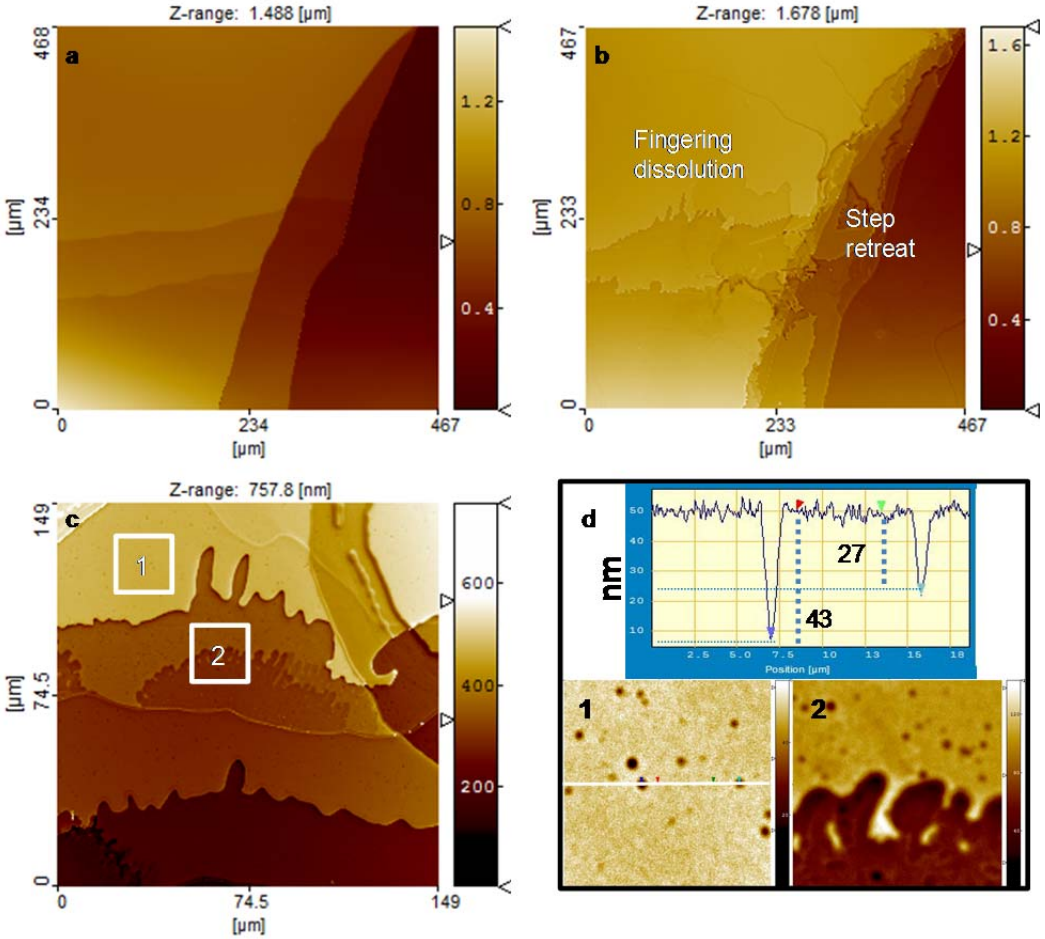

Figure 4.7. VSI images of biotite (001) surface: pristine surface (a) and reacted surface in 0.01 mol L^{-1} oxalic acid at 50°C for 72h (b, c). Fingering dissolution patterns are shown along retreating steps (b, c). Uniformly distributed etch pits (dark patches) with different size formed all over the biotite basal surface (c, d). The two images in (d) are the detailed images delimited in squares 1 and 2 in (c). The profile in (d) is that of the solid line shown in square 1.

Evolution of the dissolution features with time yielded an increase in surface roughness as nucleation and growth of etch pits progressed continuously (Figure 4.8). As a result, an increase in the root-mean-square roughness, R_q, was calculated using Eq.(2.9). R_q

increased from 4.4 nm to 9.2 nm in 120 h in 0.01 mol L^{-1} oxalic acid solution at 50 °C (Figure 4.8a,b -experiments B51-50-0.01 and B50-50-0.01). An increase in the oxalic acid concentration from 0.01 to 0.1 mol L^{-1} induced only a slight increase in surface roughness: at 70 °C, R_q was 20.0 nm in 0.01 mol L^{-1} oxalic acid (Figure 4.8c, experiment B52-70-0.01) and 22.7 nm in 0.1 mol L^{-1} oxalic acid (Figure 4.8d-experiment B54-70-0.1) after 72 h. However, the same increase in oxalic acid concentration favored etch pit merging by increasing the rate of etch pit formation and growth, preventing to recognize the pristine biotite (001) surface (Figure 4.8d). The experimental results in the presence of oxalic acid showed a strong effect of temperature on the basal surface roughness, resulting in an increase in R_q from 4.4 nm (50 °C) to 20.0 nm (70 °C).

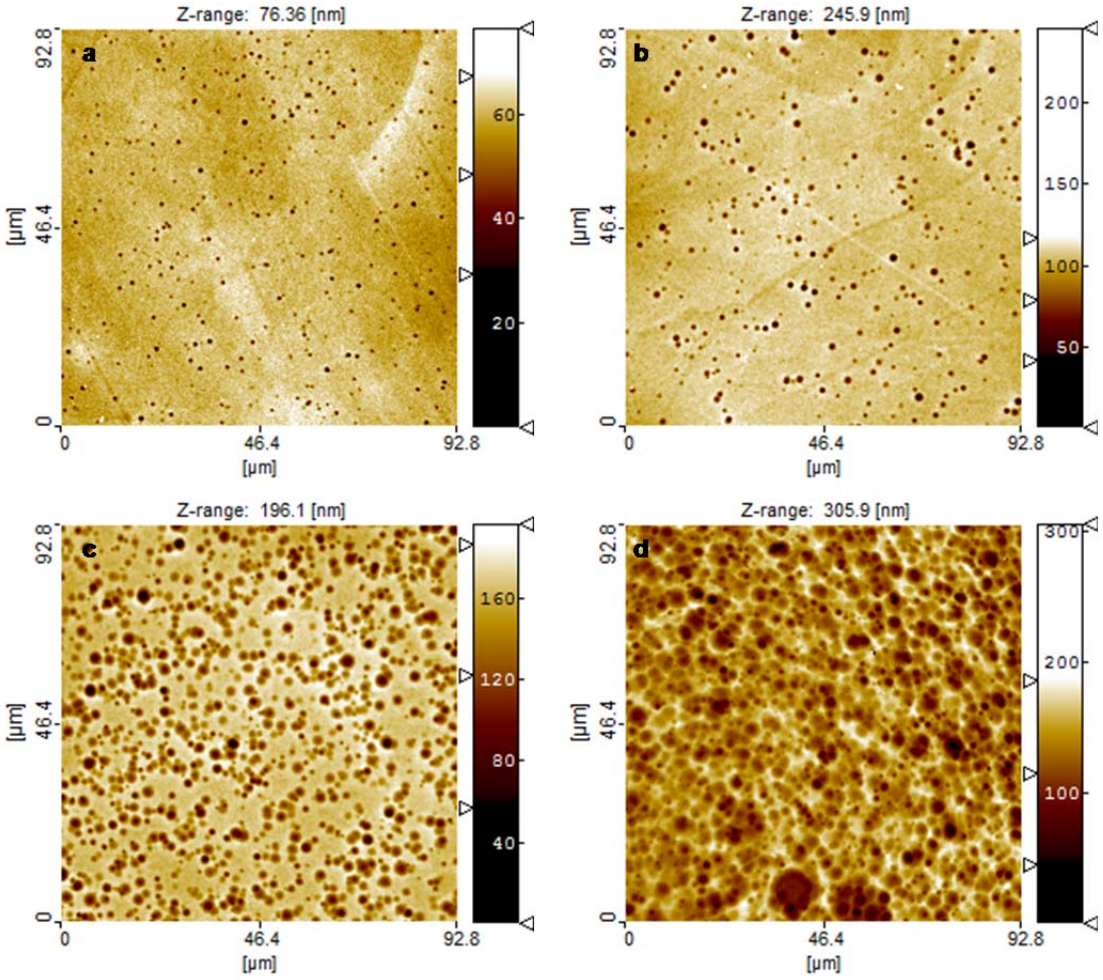

Figure 4.8. VSI images of biotite (001) surface after reaction at: 50°C with 0.1 mol L^{-1} oxalic acid for 72 (a) and 192 h (b); 70 °C with 0.01 (c) and 0.1 mol L^{-1} (d) oxalic acid for 72h. High concentration of oxalic acid and high temperature lead to intense surface etching: etch pits merge dissolving completely the initial surface.

Likewise, an increase in both the temperature and oxalic acid concentration affected the edge retreat and thus the shape of resulting fingering. Increasing temperature, widespread fingering changed from branched to jagged shapes (Figure 4.9b,c). Likewise, an increase in oxalic acid concentration yielded indented edges (Figure 4.9c,d; see also Figure 8.3, Appendix II).

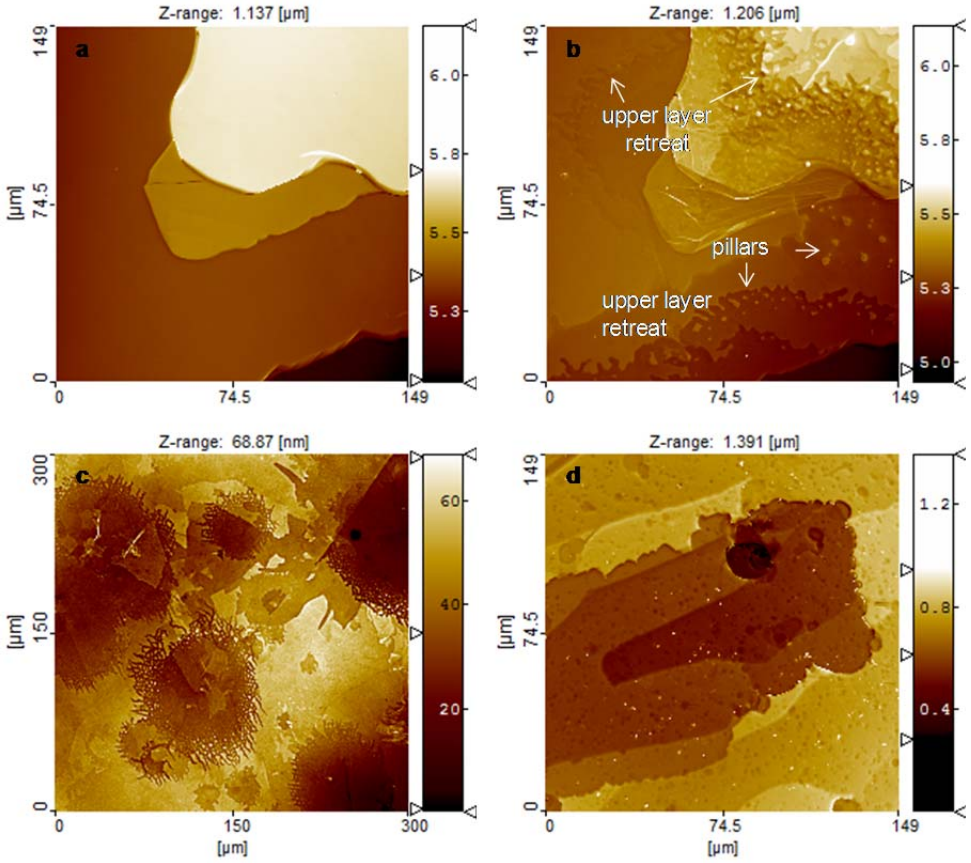

Figure 4.9 VSI images of biotite (001) surface: pristine surface (a) and same surface after reaction with 0.01 mol L^{-1} oxalic acid at 40 °C during 72h; after reaction at 25 °C with 0.01 (c) and 0.1 mol L^{-1} (d) oxalic acid for 816 and 1656 h respectively. Pillars of biotite surface (b) are shown on fresh surface uncovered after retreat of upper layers (see text for explanation).

In general, large circular and/or hexagonal or pseudo-hexagonal etch pits were frequently observed on the reacted biotite (001) surface (Figure 4.10 and Figure 8.3 Appendix II). The large etch pits exhibited circular or pseudo-hexagonal shapes in the 0.01 mol L^{-1} experiments and different temperatures (Figure 4.10a-c), whereas an increase in oxalic acid concentration to 0.1 mol L^{-1} led to formation of hexagonal etch pits (Figure 4.10d).

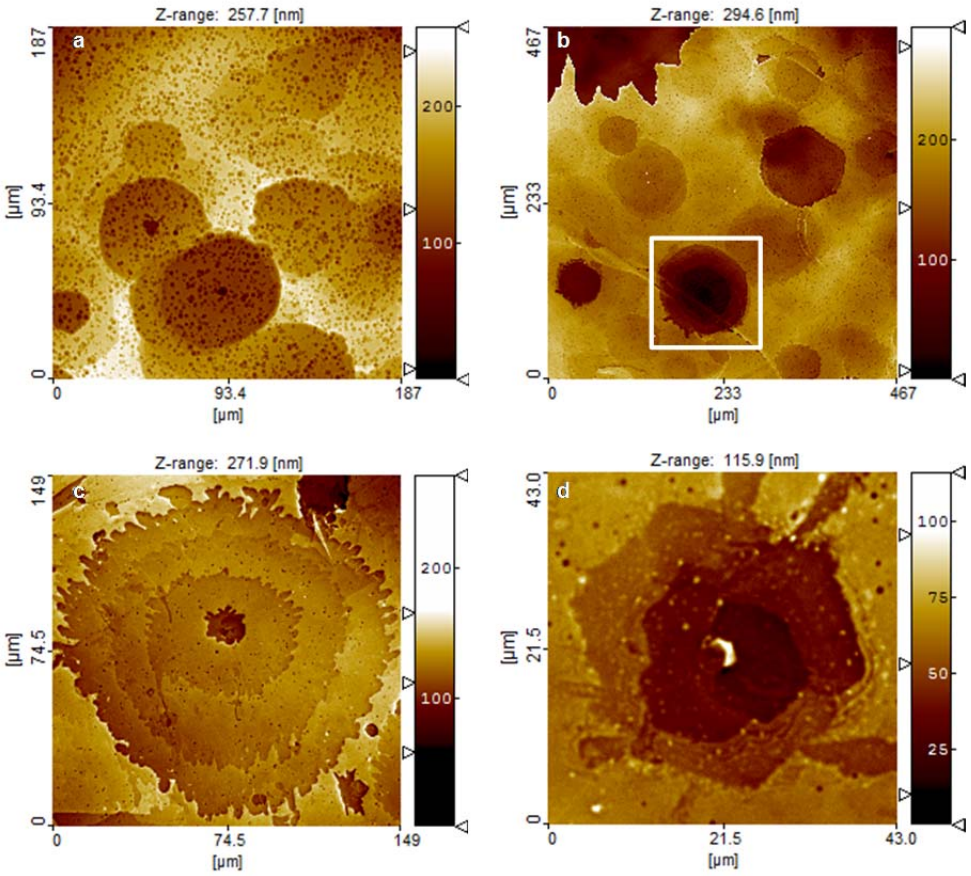

Figure 4.10. VSI images showing large etch pits over the reacted biotite (001) surface in the presence of oxalic acid in: 0.01 mol L^{-1} oxalic acid at 70 °C (a), 50 °C and 40 °C after 72 and 192 h, respectively (b,c); 0.1 mol L^{-1} oxalic acid at 40 °C for 72 h (d). Etch pits show circular (a, c), pseudo hexagonal (b) and hexagonal (d) shapes. Etch pit concentric fronts in (b), (c) and (d) would lead to formation of stepwaves (see text).

According to (Lasaga and Luttge, 2001), mineral dissolution occurs through generation of surficial stepwaves, which emanate from etch pit dissolution. The evolution of the etch pits observed in this study would support this mechanistic model for biotite dissolution (see Figure 8.2-Appendix II).

4.2.2 Dissolution rates of the biotite (001) cleavage surface

R_{Si}, R_{Al}, R_{Mg} and R_K were calculated according to Eq (2.11). The dissolution rates increased with temperature and oxalic acid concentration (Table 4.5). In general, R_{Si} and R_{Al} were the same, within an uncertainty of 15 %, whereas R_{Mg} and R_K were slower with some exceptions (see Mg/Si and K/Si stoichiometric ratios in Table 8.2-Appendix II).

Table 4.5. Dissolution rates calculated from the cations released from biotite dissolution in oxalic acid solutions.

Experiment	T (°C)	duration (h)	R_{Si}	R_{Al}	R_{Mg}	R_{Fe}	R_K
			(mol g^{-1} s^{-1})				
oxalic acid 0.1M							
B37b_25_0.1	25	212	3.6E-11	4.7E-11	7.7E-12	3.3E-11	1.9E-11
B38b_40_0.1	40	191	1.1E-10	1.1E-10	1.7E-11	9.7E-11	5.2E-11
B39b_50_0.1	50	191	2.2E-10	1.9E-10	2.4E-11	1.7E-10	1.0E-10
B40b_70_0.1	70	192	7.1E-10	1.1E-09	1.7E-10	6.3E-10	8.2E-10
oxalic acid 0.01M							
B48_25_0.01	25	212	2.6E-11	2.8E-11	2.3E-13	3.0E-11	-
B49_40_0.01	40	191	6.5E-11	7.5E-11	2.1E-12	6.5E-11	-
B50_50_0.01	50	191	8.5E-11	1.6E-10	9.0E-12	7.4E-11	1.1E-11
B43b_70_0.01	70	192	1.7E-10	1.6E-10	3.2E-11	1.3E-10	1.5E-10

Variation in R_{Si} with temperature depends on oxalic acid concentration. Activation energy values of 36 and 56 kJ mol^{-1} were obtained in 0.01 (pH 2.2) and 0.1 mol L^{-1} oxalic acid (pH 1.4) respectively. As in the absence of oxalic acid, E_a increases by increasing acidity. The obtained E_a values are similar to the value reported by Haward et al. (2011) for (hk0) biotite surface dissolution in presence of 0.1 mol L^{-1} oxalic acid (49 kJ mol^{-1}) and with those found in this study for biotite dissolved in the absence of oxalic acid (see Table 4.4).

The temperature effect on the biotite dissolution rate was also estimated from the variation in $R_{diss,p}$ using Eq. (2.10) from 25 to 70°C and 0.1-0.01 mol L^{-1} oxalic acid (Figure 4.6c) (see Figures 9.1 and 9.2; Appendix III). The estimated E_a values, associated to formation of etch pits, were 121 kJ mol^{-1} at pH 2.2 (oxalic acid 0.01 mol L^{-1}) and 162 kJ mol^{-1} at pH 1.4 (oxalic acid 0.1 mol L^{-1}). These values were higher than those derived from the biotite R_{Si} rates, but closer to the E_a value of 140 kJ mol^{-1} obtained by Haward et al. (2011) by measuring etch pit perimeters during biotite dissolution in presence of 0.1 mol L^{-1} oxalic acid at pH 1.3.

4.3 Phlogopite dissolution

4.3.1 Dissolution mechanism of the phlogopite (001) cleavage surface

VSI was used to perform *ex situ* topographical measurements of the reacted phlogopite (001) surface in the temperature range 40-100°C and in the absence (HNO_3) and presence of oxalic acid (Table 2.3-Table 2.4). Comparison between pristine and reacted basal

surfaces in 0.01 mol L^{-1} HNO_3 and 0.1 mol L^{-1} HNO_3 solutions (pH 1 and 2) shows that step retreat (Figure 4.11a-d) and formation of triangular-shaped etch pits (Figure 4.11e,f) are the mechanisms responsible for phlogopite dissolution.

In the absence of oxalic acid, formed triangular etch pits were not homogeneously distributed over the phlogopite (001) surface. In some regions coalescence of a large number of triangular etch pits of different sizes (sides of ~1-4 μm) produced trenches (Figure 4.12a). In some other regions, the large triangular etch pits (sides of ~ 4 μm) were dispersedly located (Figure 4.12b). It was also observed formation of triangular etch pits with opposite orientation, being associated to the hexagonal structure of the basal surface (Figure 4.12c). The presence of etch pits, as well as their size range (sides of ~1-5 μm), increased with temperature (Figure 4.12d). New generations of etch pits formed as preexisting ones grew.

In the presence of oxalic acid, nucleation of etch pits is strongly favored (Figure 4.12e,f). Dense populations of etch pits of different size formed and completely etched some areas of the (001) surface (Figure 4.12e,f). An increase in oxalic acid concentration leads to formation of larger triangular etch pits, indicating a catalytic effect of the oxalic acid on the dissolution rate (Figure 4.13a,b) as explained in the next section. As in the experiments with free-oxalic solution, etch pits distributed forming trenches. Similar arrangement of pits was observed by Kurganskaya et al. (2012) on reacted muscovite (001) surface at basic pH (9.4) and 155 °C (d).

4.3.2 Dissolution rates of the phlogopite (001) cleavage surface

In the absence of oxalic acid, R_{diss} could not be measured using VSI measurements over the experimental runs, indicating that phlogopite dissolution rate was slower than that of biotite under the experimental conditions of this study. It was possible to obtain an average value for the step retreat rate (R_r) of 2.35×10^{-4} μm s^{-1} at pH 1 and 100 °C by comparing the VSI images of unreacted and reacted phlogopite (001) surfaces (Figure 4.11a,b). Phlogopite retreat rate resulted to be 3 orders of magnitude slower than that of biotite at pH 1 and 100°C, which was derived using Eq. (4.1) and an E_a value of 67 kJ mol^{-1} (Table 4.4), equaling 5×10^{-1} μm s^{-1}. Reported phlogopite and biotite dissolution rates yield differences no larger than two orders of magnitude in acidic pH solutions (Clemency and Lin, 1981; Acker and Bricker, 1992; Kalinowski and Schweda, 1996; Malmström and Banwart, 1997; Taylor et al., 2000b).

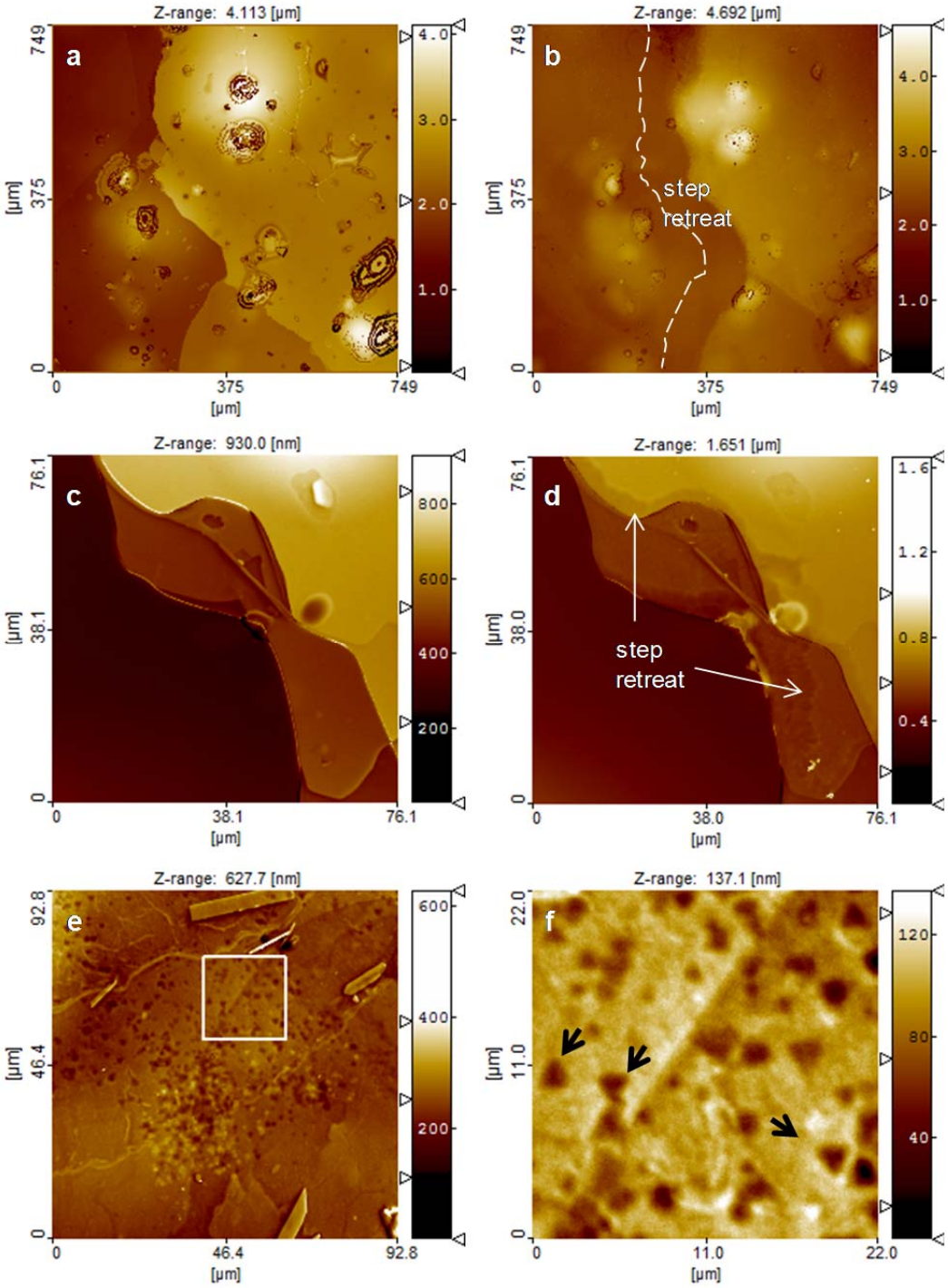

Figure 4.11. VSI images of phlogopite (001) surface: pristine surfaces (a, c) and after reaction with 0.1 mol L^{-1} HNO_3 at 100 °C for 96 h (b) and 0.01 mol L^{-1} HNO_3 at 100 °C for 24 h (d); surface after reaction with 0.1 mol L^{-1} HNO_3 at 40 °C for 1056 h (e, f). Step (b) and upper layers retreat (d) are shown. Dotted line in (b) indicates the previous position of the main edge. Image (f) shows the squared region in (e) in detail: small etch pits formed with triangular shape (shown by black arrows).

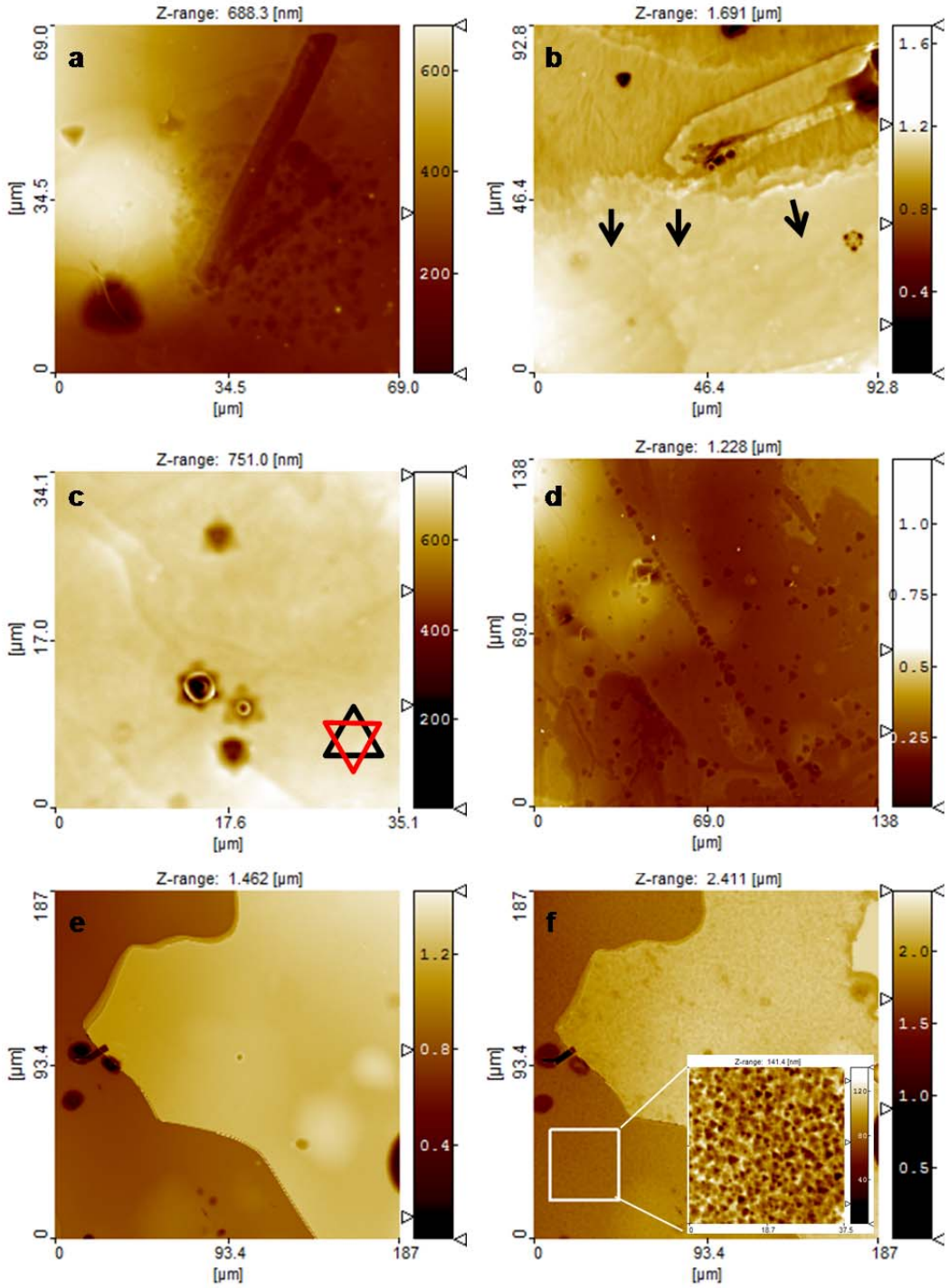

Figure 4.12. VSI images of phlogopite (001) surface after reaction with 0.1 mol L^{-1} HNO_3 at 70 °C for 168 h (a-c) and 100 °C for 48 h (d); pristine surfaces (e), and after reaction with 0.01 mol L^{-1} oxalic acid at 70 °C for 168 h (f) Trenches of etch pits (a, d) together with localized (a) or more dispersed (b-d) pits form. In (c) overlap of two pits is shown. Step retreat is also depicted (b) (black arrows indicate dissolution direction). In presence of oxalic acid the etching of the surface is much more intense (e, f).

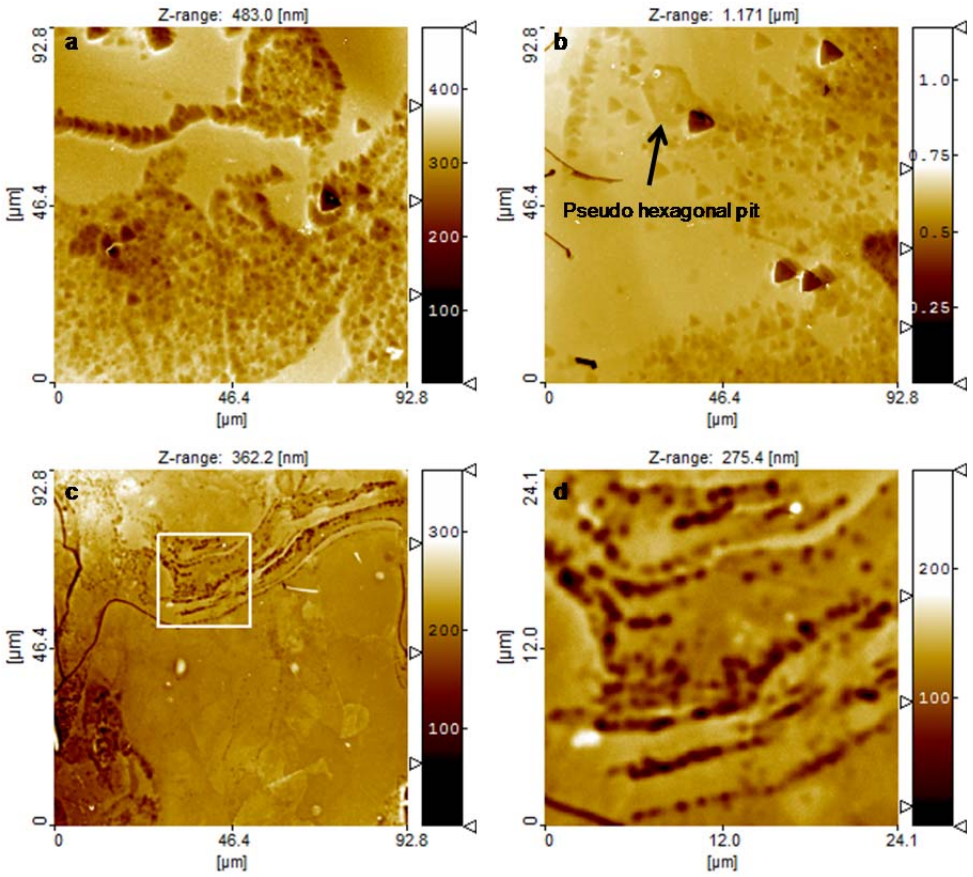

Figure 4.13. VSI images of phlogopite (001) surface after reaction with 0.1 mol L^{-1} oxalic acid at 70 °C for 168 h (a-c) and with 0.01 mol L^{-1} oxalic acid at 80 °C for 48 h (d). Big triangular etch pits formed and merged, leading to etch pits with pseudo-hexagonal shapes (a, b). In some areas over the (001) surface, etch pits distributed along tracks, forming trenches (a, b, c).

4.4 Comparison between biotite and phlogopite dissolution

In the absence of oxalic acid, edge retreat is the dominant mechanism that drives dissolution of the (001) surface of biotite and phlogopite. Simultaneously, localized formation and growth of etch pits on the biotite (001) surface and etch pit populations of different sizes on the phlogopite (001) surface contribute to the overall mica dissolution at pH 1 and 2 (Figures 4.4-4.5 and Figures 4.11-4.12). This observation disagrees with Haward et al. (2011), who observed only a widespread roughening on the (001) biotite surface at pH 1 (HCl) at room temperature, and Rufe and Hochella (1999) who, after etching the phlogopite surface with HF, did not observe the nucleation of etch pits on the (001) surfaces.

In contrast, in the case of mica dissolution in the presence of oxalic acid, formation of etch pits predominates over edge step retreat, in agreement now with Haward et al. (2011) who reported formation of etch pits on the biotite (001) surface in the presence of oxalic acid.

4.4.1 Step edge retreat

The step edge retreat on the biotite and phlogopite (001) surface is consistent with reported observations in previous studies of mica dissolution (Acker and Bricker, 1992; Kaviratna and Pinnavaia, 1994; Turpault and Trotignon, 1994; Rufe and Hochella, 1999; Aldushin et al., 2006). It is related with a selective release of interlayer (K^+, Na^+) and octahedral (Mg^{2+}, Fe^{2+}, Fe^{3+}, Al^{3+}) cations through the {hk0} surfaces that is followed by depolymerization and polymerization of tetrahedral sheets. These reaction stages lead to swelling and peeling of the uppermost layers of biotite on high steps and formation of a degraded, low reflective surface (Turpault and Trotignon, 1994), which is associated with a residual silica-rich layer, yielding a mica incongruent dissolution (Rufe and Hochella, 1999). The fact that swelling and peeling were not observed in the phlogopite images could be related to its highly low dissolution rate and stable structure in contrast to the biotite one, which is destabilized by Fe^{2+} oxidation and leads to charge imbalance.

Ruiz-Agudo et al. (2012) proposed an alternative mechanism to account for the mineral dissolution. Formation of a leached layer, due to the loss of octahedral and interlayer cations, is substituted by formation of a dissolution/re-precipitation interface where amorphous silica-rich surface layer form (Hellmann et al., 2012). The always congruent mineral dissolution would be followed by precipitation of a secondary phase. Accordingly, an increase in layer thickness is associated with a newly formed silica layer. However, it seems that the proposed model cannot account for the layer curling and peeling observed in this study and previous ones (Bisdom et al., 1982; Turpault and Trotignon, 1994).

Biotite step edge retreat exhibits different behavior depending on the nature of the acid. Lasaga and Lüttge (2004a, b) observed fluctuation of the step straightness in the elaboration of a kinetic model for dissolution of AB and A_3B structures. However, this fluctuation was not as sharp as breaking up the linearity of the overall dissolution that occurs through many layers. This theoretical model agrees with the biotite step retreat observed in nitric acid. Even if edge reactivity seems site specific at the beginning of dissolution, as reaction progresses steps start to retreat almost uniformly. In contrast, as oxalic acid reacts with biotite, edge dissolution shows fingering formation.

Shao et al. (2010) reported precipitation of amorphous and crystalline phases on phlogopite surface in an undersaturated bulk solution under geological CO_2 sequestration conditions. Mineral pillars remained under precipitates while layer continued to dissolve all around these particles. The pillars become thinner as dissolution proceed and eventually were

detached together with the particle, causing formation of a cavity. Considering possible precipitation of Mg and Fe oxalates on biotite edge surface due to the formation of saturated micro-environments, dissolution would take place in undersaturated regions, allowing step retreat around the blocking sites and formation of fingering (Figure 4.9b). Under the experimental conditions of this study, saturated micro-environments likely do not form during phlogopite dissolution and steps retreat as usual. In contrast, structural Fe in biotite probably leads to a rapid cation release due to Fe oxidation and formation of ligand-complexes on the surface and or in solution, promoting local supersaturation in spite of bulk solution undersaturation.

4.4.2 Etch pit formation

Crystal lattice defects (e.g., point and line defects, stacking fault and all types of transitions between otherwise homogeneous material) promote formation of etch pits (Lüttge and Arvidson, 2010). In particular, dislocations are an efficient nucleating agent for etch pit formation and stepwaves propagation. When the solution undersaturation exceeds a critical value ($\Delta G<\Delta G_{crit}$) etch pits form (Lasaga and Blum, 1986). For large undersaturation etch pits become the source of a train of steps that move away from the defect (Lasaga and Luttge, 2001, 2003). This dissolution model accounts for the variation of mineral dissolution rate with the degree of undersaturation on the basis of defect-generated dissolution stepwaves and is validated by Monte Carlo predictions and experimental results (Vinson and Lüttge, 2005; Cama et al., 2010; Kurganskaya and Luttge, 2013).

EQ3-NR calculations at 25 °C, using log K_{eq} = 31.8 (Vieillard, 2000) and Eqs. (2.4) and (2.5), show that ΔG_r ranges from -88 to -77 kcal mol^{-1} for the output oxalic-free solutions in the biotite experiments (Table 4.6). Owing to the restricted presence of etch pits on the biotite (001) basal surface, it is suggested that ΔG_r is not overcoming sufficiently ΔG_{crit}. In the case of dissolution of phlogopite (001) surface, etch pits spread over the surface in both the absence and presence of oxalic acid, suggesting that $\Delta G_r < \Delta G_{crit}$. However, in the present study, ΔG_{crit} could not be calculated.

The significant formation of etch pits and increase in surface roughness evidences that reactivity of biotite and phlogopite (001) surface enhances in the presence of oxalic acid. The catalytic effect of organic acids on the mineral dissolution rates is well-known and is associated to formation of surface complexes (Welch and Ullman, 1993; Pokrovsky et al., 2005; Cama and Ganor, 2006; Olsen and Rimstidt, 2008; Haward et al., 2011; Shao et al., 2011); aqueous complexes (Barman et al., 1992; Oelkers and Schott, 1998; Oelkers and

Gislason, 2001); simultaneous contribution of both surface and solution complexes (Wang et al., 2005; Golubev et al., 2006; Tu et al., 2007; Ramos et al., 2014).

In the presence of oxalic acid, aqueous complexation between oxalic species and metal cations yields a more understaurated solution than in the absence of oxalic acid. EQ3-NR calculations show that in the output solutions with 0.01 and 0.1 mol L^{-1} oxalic acid at 25°C, 99 % of Al and Fe and 97 % of Mg form oxalate complexes ($Al(Ox)_3^{3-}$and $Fe(Ox)_3^{3-}$, $Mg(Ox)_2^{2-}$), yielding a high undersarturated solution with respect to biotite. The calculated ΔG_r ranged from -138 to -131 kcal mol^{-1} (Table 4.6), becoming almost twice larger than that for oxalic-free solution.

The formation of different populations of etch pits is primarily related to the extent of lattice distortion, and consequently dislocation stress energy, whose magnitude is express by the Burgers vector (*b*) (van der Hoek et al., 1983). The ΔG_{crit} is very sensitive to *b* and surface free energy variation (Lasaga and Blum, 1986). Initial existence of different crystal deformations could cause formation of wide populations of etch pits of diverse sizes. Another plausible explanation is that inclusions of radionuclides in biotite and phlogopite, in addition to structural dislocation defects, could originate etch pits lattice distortion, leading to large circular-shaped and hexagonal etch pits (Gentry, 1974; Hashemi-Nezhad, 1985; Lang et al., 2002; Lang et al., 2004; Hashemi-Nezhad, 2005; Stübner and Jonckheere, 2006; Stübner et al., 2008).

Regardless the dependence of the etch pit morphology on the type of lattice defects, the observed formation of geometric-shaped etch pits indicates that reactivity of the biotite and phlogopite (001) surface is crystallographically controlled. This observation agrees with previous studies of dissolution of hectorite and nontronite (Bosbach et al., 2000; Bickmore et al., 2001). Recent results from AFM experiments on muscovite dissolution together with Kinetic Monte Carlo modeling show crystallographic control on mica dissolution (Kurganskaya et al., 2012; Kurganskaya and Luttge, 2013). Hexagonal etch pits on muscovite surface showed asymmetric shape with shallowest depths orientated along two preferential directions and formed a characteristic zigzag pattern reflecting stacking periodicity proper of polytypysm of mica minerals. In this study, this mechanism was observed when the biotite (001) surface reacted in the presence of oxalic acid (Figure 4.10d). The observed formation of hexagonal or triangular etch pits on biotite and phlogopite (001) surface validates the predictions of the PBC theory for phyllosilicate dissolution (Bickmore et al., 2001), although preferential

crystallographic orientations were not distinguished in the biotite (001) surface reacted in HNO_3 solution (Cappelli et al., 2013).

Table 4.6. ΔG_r and SI values calculated with EQ3-NR for biotite experimental solutions with 0.01-0.1 mol L^{-1} HNO_3 at 25-70°C and 0.01-0.1 mol L^{-1} oxalic acid at 25°C. Na-Mt = Na-montmorillonite; Qz= quartz; Na- and H-nontr= Na- and H-nontronite.

Experiment	Biotite	Na-Mt	SiO_2(am)	Qz	Boehmite	Gibbsite	Kaolinite	Muscovite	$Fe(OH)_3$	Brucite	Goethite	Na-nontr	H-nontr
	ΔG_r (kcal mol^{-1})						log IAP/K_{eq}						
B13_25_1-7	-82.8	-23.2	-1.3	**0.0**	-9.7	-9.9	-19.0	-35.5	-7.8	-18.9	-2.7	-8.5	
B12_25_2-12	-78.7	-19.8	-1.8	-0.5	-6.9	-7.1	-14.5	-28.1	-5.0	-17.4	**0.1**	-3.6	
B23_25_3-7	-76.5	-17.5	-2.5	-1.2	-4.6	-4.8	-11.2	-22.8	-3.3	-15.1	**1.8**	-1.5	
B23_25_3-8	-77.7	-17.6	-2.4	-1.1	-4.5	-4.7	-11.0	-22.5	-3.3	-15.9	**1.8**	-1.3	
B10_40_1-2	-84.8	-21.4	-1.3	-0.1	-8.6	-8.9	-17.1	-32.2	-6.9	-17.8	-2.0	-7.1	
B10_40_1-3	-85.7	-21.6	-1.3	-0.1	-8.6	-8.9	-17.2	-32.5	-7.0	-17.8	-2.0	-7.3	
B21_40_2-4	-81.0	-17.8	-1.7	-0.6	-5.8	-6.1	-12.4	-24.9	-4.1	-16.4	**0.9**	-1.9	
B25_40_2-3	-81.9	-18.7	-1.9	-0.7	-5.9	-6.2	-13.0	-25.5	-4.3	-16.4	**0.7**	-3.0	
B25_40_2-6	-82.5	-19.0	-2.0	-0.8	-5.9	-6.2	-13.2	-25.8	-4.4	-16.5	**0.5**	-3.5	
B24_40_3-3	-78.9	-15.1	-2.3	-1.1	-3.3	-3.6	-8.6	-18.5	-2.4	-14.8	**2.5**	**0.5**	
B8b_50_1-2	-88.5	-21.0	-1.3	-0.2	-8.2	-8.5	-16.5	-31.1	-6.6	-17.7	-1.8	-6.9	
B6_50_2-3	-80.0	-15.7	-1.6	-0.4	-5.0	-5.4	-10.8	-21.8	-3.5	-15.4	**1.3**	-0.3	**1.0**
B6_50_2-4	-81.1	-16.2	-1.6	-0.5	-5.1	-5.5	-11.1	-22.4	-3.6	-15.5	**1.2**	-0.8	**0.2**
B26_50_2-3	-82.2	-16.7	-1.8	-0.7	-5.1	-5.4	-11.3	-22.8	-3.8	-15.4	**1.0**	-1.7	
B30_70_1-2	-82.2	-15.8	-0.9	**0.2**	-6.2	-6.6	-12.0	-24.1	-5.1	-16.0	-0.5	-2.4	
B37b_25_0.1	-138.5	-63.0	-2.1	**-0.4**	-30.6	-30.9	-61.6	-102.1	-34.7	-28.3	-27.7	-66.7	
B56_25_0.1-3	-135.5	-44.3	-1.7	**0.0**	-22.1	-22.3	-43.9	-72.7	-25.2	-20.5	-20.0	-47.1	
B44_25_0.01-1	-131.3	-41.3	-1.6	**-0.3**	-19.9	-20.1	-40.1	-66.5	-22.8	-19.0	-17.7	-67.4	

4.4.3 Dissolution channels

Dissolution channels form recurrently on reacted mica surfaces in acidic pH. Brandt at al. (2003) reported formation of these dissolution structures during chlorite dissolution at 25 °C in acidic pH (HCl) and was ascribed to initial existence of cracks on the sample. Others studies identified dissolution channels on the reacted biotite and phlogopite basal surfaces in CO_2-rich and high saline solutions (Hu et al., 2011; Shao et al., 2011). It was argued that detachment of fibrous precipitates on mica surfaces was responsible for formation of deep channels. However, in the present study, EQ3-NR calculations show that most of the solutions are highly undersaturated with respect to aluminosilicates that could form under the present experimental conditions (kaolinite, Na-montmorillonite or muscovite; Table 4.6). Only in experiments B24-40-3 and B6-50-2 (Table 4.6) solution supersaturation with respect to Na-nontronite and H-nontronite was reached. In the case of phlogopite, streaks on (001) surface were observed in a few cases (Figure 8.1b-Appendix II) but it is difficult to distinguish whether these structures are swelled layers or precipitates.

4.4.4 Oxalic acid effect on mica dissolution kinetics

According to previous studies (Welch and Ullman, 1993; Johnson et al., 2004; Persson and Axe, 2005; Pokrovsky et al., 2005; Ramos et al., 2014) the oxalic acid has the capacity to form inner and outer-sphere bi dentate mononuclear complexes with cations (Fe^{3+}, Al^{3+} and Mg^{2+}) on edge mineral surface. Complexation of oxalic species enhances dissolution of aluminum and iron (hydr)oxides, and aluminosilicates (Stumm, 1986; Biber et al., 1994; Stumm, 1997). Functional groups of low molecular weight organic acids, such as oxalic acid, work as electron donors facilitating the detachment of the metal center complex (unlike to oxyanions that form bi or multinuclear complexes which are dissolution inert but have inhibitor effect due to blocking of reactive sites).

Some studies reported that the catalytic effect of ligands on mineral dissolution rates depends on pH. Whelch and Ullman (1993) observed that the degree of ligand-promoted enhancement of plagioclase dissolution rate decreases with the increase of acidity. Persson and Axe (2005) did not observe ligand-promoted dissolution when goethite reacted with oxalic acid over a pH range of 2.5-8. Ramos et al. (2014) showed that montmorillonite dissolution at pH < 3-4 was not promoted in the presence of 0.1, 0.3 and 1 mmol L^{-1} oxalic acid. The authors argued that, although oxalate adsorption on montmorillonite surface increases as pH acidity increases, ligand-promoted dissolution contribution to the overall rate

is significantly lower than the contribution of proton-promoted dissolution at very acidic pH (i.e., chelating affinity of weak acids decrease with the decrease of pH). This assumption could explain the decrease in biotite dissolution rate by adding oxalic acid in solution considering that the pH in that case is a little higher than inorganic solution (~1.4 and 2.2 in contrast to ~1 and 2). However, according to Johnson et al. (2004) and Pokrovsky et al. (2005) who showed the catalytic effect of the oxalic acid on corundum and brucite dissolution rates (Johnson et al., 2004; Pokrovsky et al., 2005), the increasing of ligand concentration should lead to a greater effect due to the enhancement of surface ligand-metal complexes and the promotion of surface protonation (Biber et al., 1994).

4.5 Summary and conclusions

The kinetics of biotite dissolution and reaction mechanism were investigated at acidic pH in the presence of inorganic (HNO_3) and organic (oxalic acid) acids over a wide temperature range (11.5-80 °C) by means of high-resolution microscopic techniques. Also, a comparison between biotite and phlogopite dissolutions in acidic condition was presented. The experiments were performed using mica fragments that allowed investigation of the (001) cleavage surfaces.

Biotite dissolution rates in the absence of oxalic acid (HNO_3 solutions) were obtained from (a) the measurement of the horizontal step retreat using LCM-DIM and normal step dissolution (PSI-VSI) and (b) the released structural cations in the solutions of batch experiments. Although the rates obtained from microscopic observation are not comparable with those obtained from the bulk solution, a similar dependence of dissolution rate on temperature was found.

Edge retreat was the dominant mechanism of dissolution of both the biotite and phlogopite (001) cleavage surfaces. Formation of etch pits also intervened in the dissolution process. However, triangular etch pits form and grow on phlogopite surface, whereas round-shaped etch pits were observed on the biotite surface by AFM and, only on localized areas of the biotite (001) surface reacted at pH 3 by VSI.

In the presence of oxalic acid, dissolution was dominated by etch pit formation and growth. On the biotite (001) surface, the originated etch pits showed two main shapes: circular and hexagonal. On the phlogopite surface triangular etch pits develop. Clearly, step retreat is also taking place. Fingering structures form along biotite step edges.

The solution saturation state is likely the main factor controlling the predominance of one dissolution mechanism over the other. Etch pits generate from surface defects on the biotite (001) surface in presence of both the HNO_3 and oxalic acids but hardly grow during dissolution with HNO_3. Ligand-metal complexes in solution ($Al(Ox)_3^{3-}$, $Fe(Ox)_3^{3-}$, $Mg(Ox)_2^{2-}$) lower ΔG_r below ΔG_{crit}, allowing etch pits to expand following the stepwave pattern. Triangular etch pits always open up on phlogopite surface being its density higher in the case of alteration with oxalic acid. Phlogopite dissolves slower than biotite. The presence of much less Fe in phlogopite structure should be the cause of the slower phlogopite dissolution and consequently lower ΔG_r.

5 GENERAL CONCLUSIONS AND FUTURE WORK

As a result of the experimental work carried out for this PhD study, it is concluded that:

1. Regarding dissolution of K-montmorillonite

During the experiments, microparticles dissolution controlled the overall process until their total consumption. Cation exchange between octahedral Mg^{2+} and K^{+} was likely responsible for the preferential Mg release. The Al deficit could not be explained by precipitation of Al-bearing phases since the outflow samples were undersaturated with respect to them. Dissolution of microparticles would account for a high Al release and Al surface adsorption would occur during the first hours of the experiment, being thus unable to reproduce the long and systematic Al deficit. With time, K-montmorillonite dissolution was characterized by the achievement of a steady-state release of Si and Mg, together with a deficit in Al. The average Mg/Si ratio in outflow samples is in good agreement with the molar ratio in the mineral, indicating stoichiometric dissolution of K-montmorillonite.

K-montmorillonite dissolution rates were analyzed and fitted as functions of pH and solution saturation state (ΔG_r). Only the data that were under far from equilibrium conditions are used in fitting the relationship between dissolution rate and pH so as to ensure that the near-equilibrium (ΔG_r) effects were not included.

The measured dissolution rates showed that R_{Si} increased by decreasing pH and by decreasing ΔG_r and R_{Si} could be independent on ΔG_r (dissolution plateau) at ΔG_r < -40 kcal mol^{-1}. The K-montmorillonite rate as a function of pH and solution saturation (ΔG_r) at 25 °C can be fit reasonably well with an empirical nonlinear rate law within the framework of transition state theory as shown by Cama et al. (2000)

$$R(mol\ g^{-1}\ s^{-1}) = 10^{9.74\pm0.07} \cdot a_{H^+}^{0.58\pm0.01} \cdot \left(1 - exp\left(-3.8 \times 10^{-4} \cdot \left(\frac{|\Delta G_r|}{RT}\right)^{2.13}\right)\right)$$

The K-montmorillonite dissolution rate varied as a function of the Gibbs free energy over a large range (-40 < ΔG_r < 0 kcal mol^{-1}). The shape of the $f(\Delta G_r)$ term is similar to those proposed for rate laws that account for dissolution of distinct montmorillonites obtained

under different pH and temperature conditions (Cama et al., 2000; Metz, 2001; Marty et al., 2011) and that of chlorite disolution rate law (Zhang et al., 2015). This suggests that the obtained nonlinear $f(\Delta G_r)$ term could be extended to other phyllosilicate dissolution rate formulations.

Taking into account the findings of this study, the following suggestions can be made for future studies to unravel all steps and mechanisms that control dissolution and precipitation of mica and all reactions that contribute to an incongruent dissolution of montmorillonite.

2. Regarding the use of LCM-DIM technique

LCM-DIM is a powerful noninvasive optical technique to investigate in situ the topographic changes on dissolving mineral surface areas over a broad temperature range. Hence, this technique is useful to unravel the major dissolution mechanisms of phyllosilicates.

3. Regarding dissolution of biotite and phlogopite

Biotite dissolution rates in the absence of oxalic acid (HNO_3 solutions) were obtained from (a) the measurement of the horizontal step retreat using LCM-DIM and normal step dissolution (PSI-VSI) and (b) the released structural cations in the solutions of batch experiments. Although the microscope-derived rates are not comparable with those obtained from the bulk solution, a similar dependence of dissolution rate on temperature was found.

Edge retreat was the dominant dissolution mechanism of dissolution of both the biotite and phlogopite (001) cleavage surfaces in absence of oxalic acid. Formation of etch pits also intervened in the dissolution process. However, triangular etch pits form and grow on phlogopite surface, whereas small round-shaped etch pits (≈20-60 nm diameter, 3 nm depth) were observed on the biotite surface by AFM and in localized areas of reacted biotite at pH 3 by VSI.

In the presence of oxalic acid, dissolution was dominated by etch pit formation and growth. On the biotite (001) surface, the originated etch pits showed two main shapes: circular and hexagonal. On the phlogopite surface triangular etch pits develop. Step retreat is also taking place. Fingering structures form along biotite step edges.

The solution saturation state is likely the main factor controlling the predominance of one dissolution mechanism over the other. Etch pits generate from surface defects on the

biotite (001) surface in presence of both the HNO_3 and oxalic acids but hardly grow during dissolution with HNO_3. Ligand-metal complexes in solution ($Al(Ox)_3^{3-}$, $Fe(Ox)_3^{3-}$, $Mg(Ox)_2^{2-}$) lower the ΔG_r below ΔG_{crit}, allowing etch pits to expand following the stepwave pattern. Triangular etch pits always open up on phlogopite surface being its density higher in the case of alteration with oxalic acid. Phlogopite dissolves slower than biotite. The presence of much less Fe in phlogopite structure should be the cause of the slower phlogopite dissolution and consequently lower ΔG_r.

Future work

1. Regarding montmorillonite process:

a) Detailed characterization of the raw and reacted montmorillonite samples by XRD to investigate whether the deficit of Al in solution is consistent with cation adsorption or intercalation by cation exchange processes. Exchange isotherms and XRD profile analysis may contribute know the selectivity of K-montmorillonite for Al^{3+} (Coulter, 1969).

b) Flow-through experiments and solution analysis based on the Si isotope ratio method proposed by Gruber et al. (2013) could be a suitable approach to improve the experimental results. This method increases the analytical resolution to measure changes in concentration due to mineral dissolution and to derive more accurate dissolution rates.

2. Regarding microscopy work to study dissolution and precipitation of phyllosilicates:

a) The experimental approach based on the LCM-DIM technique can be used to study in situ the surface alteration of the mica minerals (and other minerals) over a wider range of solution composition and temperature. Acquirement of (001) surface data at the mesoscale will complement with that obtained at higher resolution scale by AFM and VSI/PSI in shorter experimental runs, as well as with that from long batch and flow-through experiments which do not provide direct information on the occurring mineral surface mechanisms.

b) A promising future perspective could involve the integration of a micro-Raman spectrometer to the LCM-DIM setup to provide simultaneous monitoring of the surface topography and eventual chemical and mineralogical changes of the solid (phyllosilicate) during alteration weathering.

Conclusiones generales e investigación futura

Como resultado del trabajo experimental llevado a cabo en esta Tesis doctoral, las principales conclusiones son las siguientes:

1. Con respecto a la disolución de K-montorillonita

Durante los experimentos en reactores de flujo continuo, el proceso inicial de disolución está controlado por la disolución de micropartículas, hasta su completa desaparición. El intercambio cationico entre Mg^{2+} y K^{+} es probablemente el responsable de la liberación preferente de Mg. El déficit en la solución de Al no se ha podido explicar considerando la precipitación de fases alumínicas ya que las soluciones de salida del reactor estaban subsaturadas respectos a estas fases. La disolución de micropartículas explicaría una elevada liberación de Al, mientras que su adsorción, según los modelos, se produciría durante las primeras horas de los experimentos. Sin embargo, los modelos no consiguen reproducir el déficit sistemático y sostenido de Al . Con el tiempo, elproceso de disolución de K-montomorillonita alcanza condiciones de estadio estacionario con respecto a Si y Mg mientras que por lo general se mantiene el déficit de Al. La relación Mg/Si en las soluciones de salida es consistente con la relación molar en el mineral, indicando una disolución estequiométrica de la K-montmorillonita.

Las velocidades de disolución de K-montmorillonita han sido analizadas y estudiada en función del pH y de la saturación de la solución (ΔG_r). Solo las velocidades más lejanas de las condiciones de equilibrio han sido usadas en el ajuste de la variación de la velocidad de disolución con el pH para minimizar el efecto debido al acercamiento al equilibrio.

Las velocidades de disolución muestran que R_{Si} aumenta al disminuir el pH y al volverse más negativo ΔG_r. R_{Si} sería independiente de las condiciones de saturación (ΔG_r) (dissolution plateau) para ΔG_r < -40 kcal mol^{-1}. La variación de la velocidad de disolución de la K-montmorillonita con el pH y la saturación de la solución (ΔG_r) a 25°C se ajusta bastante bien a la ley empírica no lineal de velocidad en el marco de la teoría del estado de transición, en consonancia con Cama et al. (2000)

$$R(mol\ g^{-1}\ s^{-1}) = 10^{9.47\pm0.07} \cdot a_{H^+}^{0.58\pm0.01} \cdot \left(1 - exp\left(-3.8 \times 10^{-4} \cdot \left(\frac{|\Delta G_r|}{RT}\right)^{2.13}\right)\right)$$

La velocidad de disolución de la K-montmorillonita varía en función de la saturación de la solución en un amplio rango de valores ($-40 < \Delta G_r < 0$ kcal mol^{-1}). La forma del término $f(\Delta G_r)$ es consistente con la literatura distintas esmectitas obtenidas en diferentes condiciones de pH y temperatura (Cama et al., 2000; Metz, 2001; Marty et al., 2011) y de clorita (Zhang et al., 2015). Esto sugiere que el termino no lineal $f(\Delta G_r)$ obtenido podría ser extendido a la formulación de la ley de disolución de otros filosilicatos.

2. Con respecto al uso de la técnica LCM-DIM

LCM-DIM es una técnica de microscopía óptica no invasiva muy potente como herramienta para investigar *in situ* los cambios topográficos sufridos por la superficie mineral durante el proceso de disolución en un amplio rango de temperaturas. Por esto, esta técnica es útil para identificar los principales mecanismos de disolución de los filosilicatos.

3. Con respecto a la disolución de biotita y flogopita

Las velocidades de disolución de biotita en ausencia de ácido oxálico (en soluciones de HNO_3) han sido obtenidas a partir de (a) la medida del retroceso del borde de los escalones utilizando LCM-DIM y del cálculo de la disolución vertical (en z) mediante el uso de VSI/PSI y (b) la concentración de los cationes estructurales en las soluciones de los experimentos en reactores tipo batch. Aunque las velocidades obtenidas por microscopia no son comparables con aquellas obtenidas del análisis de la solución, la dependencia de la velocidad con la temperatura encontradas son similares en los diferentes casos.

El retroceso del borde de los escalones es el mecanismo predominante en el proceso de disolución de las superficies de biotita y flogopita en soluciones de ácido nítrico. No obstante, la formación de *etch pits* también contribuye en el proceso de disolución. *Etch pits* triangulares se forman y crecen en la superficie de flogopita, mientras en la superficie de biotita se observa mediante AFM la formación pequeños *etch pits* (≈20-60 nm diametro, 3 nm profundidad) redondeados y mediante VSI en áreas localizadas de la superficie alterada a pH 3.

En presencia de ácido oxálico, la disolución está dominada por la formación y el crecimiento de *etch pits*. En la superficie basal de biotita los *etch pits* que se originan muestran dos formas principales: circular o hexagonal. En la superficie de flogopita se forman *etch pits* triangulares. De forma similar a la disolución en soluciones de HNO_3, también se

observa el retroceso de los escalones. El estado de saturación de la solución es probablemente el factor que principalmente controla el predominio de un mecanismo de disolución sobre el otro. Los *etch pits* se generan a partir de defectos en la superficie basal de biotita en presencia de ambos ácidos (nítrico y ácido oxálico), pero difícilmente crecen durante la disolución con HNO_3. Los complejos acuosos ligando-metal ($Al(Ox)_3^{3-}$, $Fe(Ox)_3^{3-}$, $Mg(Ox)_2^{2-}$) producen la disminución de ΔG_r por debajo del ΔG_{crit}, permitiendo a los *etch pits* expandirse siguiendo el modelo de *stepwave*. Los *etch pits* triangulares siempre se forman en la superficie de flogopita siendo su densidad mayor en el caso de alteración con ácido oxálico. Según los datos cinéticos y la observaciones topograficas, la flogopita se disuelve más lentamente que la biotita. La presencia de menor contenido de Fe en la estructura de flogopita podría ser la causa de esta menor velocidad de disolución y de un valor de ΔG_r inferior al de la biotita alterada en las misma condiciones experimentales.

Sobre la base de los resultados obtenidos en el presente estudio, se pueden tener en cuenta las siguientes consideraciones y sugerencias para estudios futuros para la interpretación de los mecanismos que controlan la disolución de mica y las reacciones que contribuyen a una disolución incongruente de las esmectitas.

Estudio fututo

Con respecto a los procesos que tienen lugar durante la disolución de montmorillonita:

- Caracterización detallada de las muestras de montmorillonita no reaccionadas y reaccionadas mediante DRX para averiguar su el déficit de Al en solución es consistente con la adsorción de cationes o la intercalación por procesos de intercambio catiónico. Las isotermas de intercambio y el análisis de los perfiles de difracción podrán contribuir a conocer la de la K-montmorillonita por el Al^{3+} (Coulter, 1969).

- la realización de experimentos de flujo continuo y el análisis de soluciones basados sobre el método de la relación isotópica del Si propuesto por Gruber et al. (2013) sería una estrategia para obtener mejores resultados experimentales. Este método permite afinar la resolución analítica en la medida de las diferencias de concentración del Si en solución derivado de la disolución del mineral y calcular velocidades de disolución con mayor precisión.

Con respecto al trabajo de microscopia para el estudio de disolución de filosilicatos y precipitación de fases secundarias:

- continuar realizando experimentos de disolución basados en la técnica LCM-DIM para el estudio *in situ* de la alteración de mica (y otros minerales) en un amplio rango de composición de la solución y de temperatura. Los datos obtenidos sobre los cambios experimentados de la superficie basal de los minerales a meso-escala se complementarán con otros obtenidos a micro-escala gracias a AFM y VSI/PSI durante experimentos de más corto plazo, así como aquellos obtenidos mediante experimentos en batch y en reactores de flujo continuo de largo plazo que no proporcionan información directa de los mecanismos implicados en la alteración mineral.

- La integración de uno espectrómetro micro-Raman en el setup experimental del LCM-DIM podría ser muy prometedor para la adquisición simultanea de la topografía superficial y datos relacionados con los posibles cambios composicionales y mineralógicos del sólido (filosilicato) durante su alteración.

6 REFERENCES

Acker, J.G. and Bricker, O.P. (1992) The influence of pH on biotite dissolution and alteration kinetics at low temperature. Geochim. Cosmochim. Acta 56, 3073-3092.

Aldushin, K., Jordan, G., Aldushina, E. and Schmahl, W.W. (2007) On the kinetics of ion exchange in phlogopite an in situ AFM study. Clays Clay Miner. 55, 339-347.

Aldushin, K., Jordan, G. and Schmahl, W.W. (2006) Basal plane reactivity of phyllosilicates studied in situ by hydrothermal atomic force microscopy (HAFM). Geochim. Cosmochim. Acta 70, 4380-4391.

Amram, K. and Ganor, J. (2005) The combined effect of pH and temperature on smectite dissolution rate under acidic conditions. Geochim. Cosmochim. Acta 69, 2535-2546.

Baba, M., Kakitani, S., Ishii, H. and Okuno, T. (1997) Fine atomic image of mica cleavage planes obtained with an atomic force microscope (AFM) and a novel procedure for image processing. Chemical Physics 221, 23-31.

Banfield, J.F. and Eggleton, R.A. (1990) Analytical transmission electron microscope studies of plagioclase, muscovite, and K-feldspar weathering. Clays Clay Miner. 38, 77-89.

Banfield, J.F., Ferruzzi, G.G., Casey, W.H. and Westrich, H.R. (1995) HRTEM study comparing naturally and experimentally weathered pyroxenoids. Geochim. Cosmochim. Acta 59, 19-31.

Barman, A.K., Varadachari, C. and Ghosh, K. (1992) Weathering of silicate minerals by organic acids. I. Nature of cation solubilisation. Geoderma 53, 45-63.

Barrante, J. (1974) Applied Mathematics for Physical Chemistry. Englewood Cliffs, New Jersey.

Bauer, A. and Berger, G. (1998) Kaolinite and smectite dissolution rate in high molar KOH solutions at 35° and 80°C. Appl. Geochem. 13, 905-916.

Berger, G., Cadore, E., Schott, J. and Dove, P.M. (1994) Dissolution rate of quartz in lead and sodium electrolyte solutions between 25 and 300°C: Effect of the nature of surface complexes and reaction affinity. Geochim. Cosmochim. Acta 58, 541-551.

Biber, M.V., dos Santos Afonso, M. and Stumm, W. (1994) The coordination chemistry of weathering: IV. Inhibition of the dissolution of oxide minerals. Geochim. Cosmochim. Acta 58, 1999-2010.

Bibi, I., Singh, B. and Silvester, E. (2011) Dissolution of illite in saline–acidic solutions at 25 °C. Geochim. Cosmochim. Acta 75, 3237-3249.

Bickmore, B.R., Bosbach, D., Hochella, M.F., Jr., Charlet, L. and Rufe, E. (2001) In situ atomic force microscopy study of hectorite and nontronite dissolution: Implications for phyllosilicate edge surface structures and dissolution mechanisms. Am. Mineral. 86, 411-423.

Bickmore, B.R., Hochella, M.F., Bosbach, D. and Charlet, L. (1999) Methods for performing atomic force microscopy imaging of clay minerals in aqueous solutions. Clays Clay Miner. 47, 573-581.

Bisdom, E.B.A., Stoops, G., Delvigne, J., Curmi, P. and Altemuller, H.J. (1982) Micromorphology of weathering biotite and its secondary products Pedologie 32, 225-252.

Bosbach, D., Charlet, L., Bickmore, B. and Hochella, M.F., (2000) The dissolution of hectorite: In-situ, real-time observations using atomic force microscopy. Am. Mineral. 85, 1209-1216.

Bradbury, M.H. and Baeyens, B. (1997) A mechanistic description of Ni and Zn sorption on Na-montmorillonite Part II: modelling. Journal of Contaminant Hydrology 27, 223-248.

Brandt, F., Bosbach, D., Krawczyk-Bärsch, E., Arnold, T. and Bernhard, G. (2003) Chlorite dissolution in the acid ph-range: a combined microscopic and macroscopic approach. Geochim. Cosmochim. Acta 67, 1451-1461.

Brantley, S.L. and Conrad, C.F. (2008) Analysis of Rates of Geochemical Reactions, in: Brantley, S.L., Kubicki, J.D., White, A.F. (Eds.), Kinetics of Water-Rock Interaction. Springer, NewYork, pp. 1-38.

Brunauer, S., Emmett, P.H. and Teller, E. (1938) Adsorption of Gases in Multimolecular Layers. Journal of the American Chemical Society 60, 309-319.

Burch, T.E., Nagy, K.L. and Lasaga, A.C. (1993) Free energy dependence of albite dissolution kinetics at 80°C and pH 8.8. Chemical Geology 105, 137-162.

Buss, H.L., Lüttge, A. and Brantley, S.L. (2007) Etch pit formation on iron silicate surfaces during siderophore-promoted dissolution. Chemical Geology 240, 326-342.

Caballero, E., Cisneros, C., Huertas, F.J., Huertas, F., Pozzuoli, A. and Linares, J. (2005) Bentonites from Cabo de Gata, Almería, Spain: a mineralogical and geochemical overview. Clay Minerals 40, 463-480.

Cama, J. and Ganor, J. (2006) The effects of organic acids on the dissolution of silicate minerals: A case study of oxalate catalysis of kaolinite dissolution. Geochim. Cosmochim. Acta 70, 2191-2209.

Cama, J., Ganor, J., Ayora, C. and Lasaga, C.A. (2000) Smectite dissolution kinetics at 80°C and pH 8.8. Geochim. Cosmochim. Acta 64, 2701-2717.

Cama, J., Metz, V. and Ganor, J. (2002) The effect of pH and temperature on kaolinite dissolution rate under acidic conditions. Geochim. Cosmochim. Acta 66, 3913-3926.

Cama, J., Zhang, L., Soler, J.M., Giudici, G.D., Arvidson, R.S. and Lüttge, A. (2010) Fluorite dissolution at acidic pH: In situ AFM and ex situ VSI experiments and Monte Carlo simulations. Geochim. Cosmochim. Acta 74, 4298-4311.

Cambier, P. and Sposito, G. (1991) Interactions of citric acid and synthetic hydroxy-aluminum montmorillonite. Clays Clay Miner. 39, 158-166.

Cappelli, C., Van Driessche, A.E.S., Cama, J. and Huertas, F.J. (2013) In Situ Observation of Biotite Dissolution at pH 1 Using Advanced Optical Microscopy. Cryst. Growth Des. 13, 2880-2886.

Carroll, S., Mroczek, E., Alai, M. and Ebert, M. (1998) Amorphous silica precipitation (60 to 120°C): comparison of laboratory and field rates. Geochim. Cosmochim. Acta 62, 1379-1396.

Charlet, L., Schindler, P.W., Spadini, L., Furrer, G. and Zysset, M. (1993) Cation adsorption on oxides and clays: The aluminum case. Aquatic Sciences - Research Across Boundaries 55, 291-303.

Cheah, S.-F., Kraemer, S.M., Cervini-Silva, J. and Sposito, G. (2003) Steady-state dissolution kinetics of goethite in the presence of desferrioxamine B and oxalate ligands: implications for the microbial acquisition of iron. Chemical Geology 198, 63-75.

Clemency, C.V. and Lin, F.-C. (1981) Dissolution kinetics of phlogopite; II, Open system using an ion-exchange resin. Clays Clay Miner. 29, 107-112.

Coulter, B.S. (1969) The equilibria of K:Al exchange in clay minerals and acid soils. Journal of Soil Science 20, 72-83.

Declercq, J., Bosc, O. and Oelkers, E.H. (2013) Do organic ligands affect forsterite dissolution rates? Appl. Geochem. 39, 69-77

Devidal, J.-L., Schott, J. and Dandurand, J.-L. (1997) An experimental study of kaolinite dissolution and precipitation kinetics as a function of chemical affinity and solution composition at 150°C, 40 bars, and pH 2, 6.8, and 7.8. Geochim. Cosmochim. Acta 61, 5165-5186.

Fernández, A.M., Baeyens, B., Bradbury, M. and Rivas, P. (2004) Analysis of the porewater chemical composition of a Spanish compacted bentonite used in an engineered barrier. Physics and Chemistry of the Earth, Parts A/B/C 29, 105-118.

Ferrage, E., Lanson, B., Sakharov, B.A. and Drits, V.A. (2005) Investigation of smectite hydration properties by modeling experimental X-ray diffraction patterns: Part I. Montmorillonite hydration properties. Am. Mineral. 90, 1358-1374.

Gaines, G.L. and Thomas, H.C. (1953) Adsorption Studies on Clay Minerals. II. A Formulation of the Thermodynamics of Exchange Adsorption. The Journal of Chemical Physics 21, 714-718.

Ganor, J., Cama, J. and Metz, V. (2003) Surface protonation data of kaolinite--reevaluation based on dissolution experiments. Journal of Colloid and Interface Science 264, 67-75.

Ganor, J., Mogollón, J.L. and Lasaga, A.C. (1995) The effect of pH on kaolinite dissolution rates and on activation energy. Geochim. Cosmochim. Acta 59, 1037-1052.

Gautier, J.-M., Oelkers, E.H. and Schott, J. (1994) Experimental study of K-feldspar dissolution rates as a function of chemical affinity at 150°C and pH 9. Geochim. Cosmochim. Acta 58, 4549-4560.

Gentry, R.V. (1974) Radiohalos in Radiochronological and Cosmological Perspective. Science 184, 62-66.

Golubev, S.V., Bauer, A. and Pokrovsky, O.S. (2006) Effect of pH and organic ligands on the kinetics of smectite dissolution at 25°C. Geochim. Cosmochim. Acta 70, 4436-4451.

Grasshoff, K., Ehrhardt, M. and Kremling, K. (2009) Methods of Seawater Analysis. John Wiley & Sons.

Gruber, C., Harpaz, L., Zhu, C., Bullen, T.D. and Ganor, J. (2013) A new approach for measuring dissolution rates of silicate minerals by using silicon isotopes. Geochim. Cosmochim. Acta 104, 261-280.

Hashemi-Nezhad, S.R. (1985) On the parameters affecting the track opening geometry in biotite mica. Nuclear Instruments and Methods in Physics Research Section A: Accelerators, Spectrometers, Detectors and Associated Equipment 234, 172-176.

Hashemi-Nezhad, S.R. (2005) The geometry of etched heavy ion tracks in phlogopite mica; a clear dependence on energy deposited. Nuclear Instruments and Methods in Physics Research Section B: Beam Interactions with Materials and Atoms 234, 533-547.

Haward, S.J., Smits, M.M., Ragnarsdóttir, K.V., Leake, J.R., Banwart, S.A. and McMaster, T.J. (2011) In situ atomic force microscopy measurements of biotite basal plane reactivity in the presence of oxalic acid. Geochim. Cosmochim. Acta 75, 6870-6881.

Hellmann, R. (1997) The albite-water system: Part IV. Diffusion modeling of leached and hydrogen-enriched layers. Geochim. Cosmochim. Acta 61, 1595-1611.

Hellmann, R., Wirth, R., Daval, D., Barnes, J.-P., Penisson, J.-M., Tisserand, D., Epicier, T., Florin, B. and Hervig, R.L. (2012) Unifying natural and laboratory chemical weathering with interfacial dissolution–reprecipitation: A study based on the nanometer-scale chemistry of fluid–silicate interfaces. Chemical Geology 294–295, 203-216.

Hodson, M.E. (2006a) Does reactive surface area depend on grain size? Results from pH 3, 25 °C far-from-equilibrium flow-through dissolution experiments on anorthite and biotite. Geochim. Cosmochim. Acta 70, 1655-1667.

Hodson, M.E. (2006b) Searching for the perfect surface area normalizing term--a comparison of BET surface area-, geometric surface area- and mass-normalized dissolution rates of anorthite and biotite. Journal of Geochemical Exploration 88, 288-291.

Howard, A.G., Coxhead, A.J., Potter, I.A. and Watt, A.P. (1986) Determination of dissolved aluminium by the micelle-enhanced fluorescence of its lumogallion complex. Analyst 111, 1379-1382.

Hu, Y., Ray, J.R. and Jun, Y.-S. (2011) Biotite–Brine Interactions under Acidic Hydrothermal Conditions: Fibrous Illite, Goethite, and Kaolinite Formation and Biotite Surface Cracking. Environmental Science & Technology 45, 6175-6180.

Huertas, F., Fuentes-Cantillana, J.L., Jullien, F., Rivas, P., Linares, J., Farina, P., Ghoreychi, M., Jockwer, N., Kickmaier, W., Martinez, M.A., Samper, J., Alonso, E. and Elorza, F.J. (2000) Full-scale engineered barriers experiment for a deep geological repository for high-level radioactive waste in crystalline host rock (FEBEX project). European Commission, EUR 19147EN, Brussels.

Huertas, F.J., Caballero, E., Jiménez de Cisneros, C., Huertas, F. and Linares, J. (2001) Kinetics of montmorillonite dissolution in granitic solutions. Appl. Geochem. 16, 397-407.

Huertas, F.J., Chou, L. and Wollast, R. (1999) Mechanism of kaolinite dissolution at room temperature and pressure Part II: kinetic study. Geochim. Cosmochim. Acta 63, 3261-3275.

Jaber, M., Bertin, F. and Thomas-David, G. (1977) Application de la spectrométrie infrarouge, Raman et résonance magnétique nucléaire à l'étude des complexes en solution aqueuse. Al^{3+}–$H_2C_2O_4$. Canadian Journal of Chemistry 55, 3689-3699.

Johnson, S.B., Yoon, T.H., Slowey, A.J. and Brown, G.E. (2004) Adsorption of Organic Matter at Mineral/Water Interfaces: 3. Implications of Surface Dissolution for Adsorption of Oxalate. Langmuir 20, 11480-11492.

Kalinowski, B.E. and Schweda, P. (1996) Kinetics of muscovite, phlogopite, and biotite dissolution and alteration at pH 1-4, room temperature. Geochim. Cosmochim. Acta 60, 367-385.

Kaviratna, H. and Pinnavaia, T.J. (1994) Acid hydrolysis of octahedral Mg^{2+} sites in 2:1 layered silicates; an assessment of edge attack and gallery access mechanisms. Clays Clay Miner. 42, 717-723.

King, H.E., Satoh, H., Tsukamoto, K. and Putnis, A. (2014) Surface-specific measurements of olivine dissolution by phase-shift interferometry. Am. Mineral. 99, 377-386.

Knauss, K.G. and Thomas J, W. (1989) Muscovite dissolution kinetics as a function of pH and time at 70°C. Geochim. Cosmochim. Acta 53, 1493-1501.

Köhler, S.J., Dufaud, F. and Oelkers, E.H. (2003) An experimental study of illite dissolution kinetics as a function of ph from 1.4 to 12.4 and temperature from 5 to 50°C. Geochim. Cosmochim. Acta 67, 3583-3594.

Kurganskaya, I., Arvidson, R.S., Fischer, C. and Luttge, A. (2012) Does the stepwave model predict mica dissolution kinetics? Geochim. Cosmochim. Acta 97, 120-130.

Kurganskaya, I. and Luttge, A. (2013) A comprehensive stochastic model of phyllosilicate dissolution: Structure and kinematics of etch pits formed on muscovite basal face. Geochim. Cosmochim. Acta 120, 545-560.

Kuwahara, Y. (2006) In-situ AFM study of smectite dissolution under alkaline conditions at room temperature. Am. Mineral. 91, 1142-1149.

Kuwahara, Y. (2008) In situ observations of muscovite dissolution under alkaline conditions at 25-50 ºC by AFM with an air/fluid heater system. Am. Mineral. 93, 1028-1033.

Kuwahara, Y. and Aoki, Y. (1995) Dissolution process of phlogopite in acid solutions. Clays Clay Miner. 43, 39-50.

Lang, M., Glasmacher, U.A., Moine, B., Müller, C., Neumann, R. and Wagner, G.A. (2002) Heavy-ion induced defects in phlogopite imaged by scanning force microscopy. Surface and Coatings Technology 158–159, 439-443.

Lang, M., Glasmacher, U.A., Moine, B., Neumann, R. and Wagner, G.A. (2004) Etch-pit morphology of tracks caused by swift heavy ions in natural dark mica. Nuclear Instruments and Methods in Physics Research Section B: Beam Interactions with Materials and Atoms 218, 466-471.

Lasaga, A.C. (1998) Kinetic Theory in the Earth Sciences. Princeton University Press, New Jersey.

Lasaga, A.C. and Blum, A.E. (1986) Surface chemistry, etch pits and mineral-water reactions. Geochim. Cosmochim. Acta 50, 2363-2379.

Lasaga, A.C. and Luttge, A. (2001) Variation of Crystal Dissolution Rate Based on a Dissolution Stepwave Model. Science 291, 2400-2404.

Lasaga, A.C. and Luttge, A. (2003) A model for crystal dissolution. Eur J Mineral 15, 603-615.

Lasaga, A.C. and Lüttge, A. (2004a) Mineralogical approaches to fundamental crystal dissolution kinetics. Am. Mineral. 89, 527-540.

Lasaga, A.C. and Lüttge, A. (2004b) Mineralogical approaches to fundamental crystal dissolution kinetics - Dissolution of an A3B structure. European Journal of Mineralogy 16, 713-729.

Lazic, D., Skundric, B., Penavin-Skundric, J., Sladojevic, S., Vasiljevic, L., Blagojevic, D. and Obrenovic, Z. (2010) Stability of tris-1, 10-phenanthroline iron (II) complex in different composites. Chemical Industry and Chemical Engineering Quarterly 16, 193-198.

Lee, J.O., Kang, I.M. and Cho, W.J. (2010) Smectite alteration and its influence on the barrier properties of smectite clay for a repository. Applied Clay Science 47, 99-104.

Leone, G., Reyes, E., Cortecci, G., Pochini, A. and Linares, J. (1983) Genesis of bentonites from Cabo de Gata, Almeria, Spain; a stable isotope study. Clay Minerals 18, 227-238.

Luettge, A., Bolton, E.W. and Lasaga, A.C. (1999) An interferometric study of the dissolution kinetics of anorthite; the role of reactive surface area. Am J Sci 299, 652-678.

Lüttge, A. (2006) Crystal dissolution kinetics and Gibbs free energy. Journal of Electron Spectroscopy and Related Phenomena 150, 248-259.

Lüttge, A. and Arvidson, R.S. (2010) Reactions at Surfaces: A New Approach Integrating Interferometry and Kinetic Simulations. Journal of the American Ceramic Society 93, 3519-3530.

Malmström, M. and Banwart, S. (1997) Biotite dissolution at 25°C: The pH dependence of dissolution rate and stoichiometry. Geochim. Cosmochim. Acta 61, 2779-2799.

Malmström, M., Banwart, S., Lewenhagen, J., Duro, L. and Bruno, J. (1996) The dissolution of biotite and chlorite at 25°C in the near-neutral pH region. Journal of Contaminant Hydrology 21, 201-213.

Martell, A. and Smith, R. (1977) Other Organic Ligands, Critical Stability Constants. Springer US.

Marty, N.C.M., Cama, J., Sato, T., Chino, D., Villiéras, F., Razafitianamaharavo, A., Brendlé, J., Giffaut, E., Soler, J.M., Gaucher, E.C. and Tournassat, C. (2011) Dissolution kinetics of synthetic Na-smectite. An integrated experimental approach. Geochim. Cosmochim. Acta 75, 5849-5864.

McMaster, T.J., Smits, M.M., Haward, S.J., Leake, J.R., Banwart, S. and Ragnarsdottir, K.V. (2008) High-resolution imaging of biotite dissolution and measurement of activation energy. Mineral. Mag 72, 115-120.

Metz, V. (2001) Dissolution Kinetics of Smectite and Kaolinite, PhD thesis, Department of Geological and Environmental Sciences. Ben-Gurion University of the Negev, Negev, Israel.

Metz, V., Amram, K. and Ganor, J. (2005a) Stoichiometry of smectite dissolution reaction. Geochim. Cosmochim. Acta 69, 1755-1772.

Metz, V. and Ganor, J. (2001) Stirring effect on kaolinite dissolution rate. Geochim. Cosmochim. Acta 65, 3475-3490.

Metz, V., Raanan, H., Pieper, H., Bosbach, D. and Ganor, J. (2005b) Towards the establishment of a reliable proxy for the reactive surface area of smectite. Geochim. Cosmochim. Acta 69, 2581-2591.

Murakami, T., Utsunomiya, S., Yokoyama, T. and Kasama, T. (2003) Biotite dissolution processes and mechanisms in the laboratory and in nature: Early stage weathering environment and vermiculitization. Am. Mineral. 88, 377-386.

Nagy, K.L., Blum, A.E. and Lasaga, A.C. (1991) Dissolution and precipitation kinetics of kaolinite at 80 degrees C and pH 3; the dependence on solution saturation state. Am J Sci 291, 649-686.

Nagy, K.L., Cygan, R.T., Hanchar, J.M. and Sturchio, N.C. (1999) Gibbsite growth kinetics on gibbsite, kaolinite, and muscovite substrates: atomic force microscopy evidence for epitaxy and an assessment of reactive surface area. Geochim. Cosmochim. Acta 63, 2337-2351.

Nagy, K.L. and Lasaga, A.C. (1992) Dissolution and precipitation kinetics of gibbsite at 80°C and pH 3: The dependence on solution saturation state. Geochim. Cosmochim. Acta 56, 3093-3111.

Oelkers, E.H. (2001) General kinetic description of multioxide silicate mineral and glass dissolution. Geochim. Cosmochim. Acta 65, 3703-3719.

Oelkers, E.H. and Gislason, S.R. (2001) The mechanism, rates and consequences of basaltic glass dissolution: I. An experimental study of the dissolution rates of basaltic glass as a function of aqueous Al, Si and oxalic acid concentration at 25°C and pH = 3 and 11. Geochim. Cosmochim. Acta 65, 3671-3681.

Oelkers, E.H., Golubev, S.V., Chairat, C., Pokrovsky, O.S. and Schott, J. (2009) The surface chemistry of multi-oxide silicates. Geochim. Cosmochim. Acta 73, 4617-4634.

Oelkers, E.H. and Schott, J. (1998) Does organic acid adsorption affect alkali-feldspar dissolution rates? Chemical Geology 151, 235-245.

Oelkers, E.H. and Schott, J. (1999) Experimental study of kyanite dissolution rates as a function of chemical affinity and solution composition. Geochim. Cosmochim. Acta 63, 785-797.

Oelkers, E.H., Schott, J. and Devidal, J.-L. (1994) The effect of aluminum, pH, and chemical affinity on the rates of aluminosilicate dissolution reactions. Geochim. Cosmochim. Acta 58, 2011-2024.

Oelkers, E.H., Schott, J., Gauthier, J.-M. and Herrero-Roncal, T. (2008) An experimental study of the dissolution mechanism and rates of muscovite. Geochim. Cosmochim. Acta 72, 4948-4961.

Olsen, A.A. and Rimstidt, J.D. (2008) Oxalate-promoted forsterite dissolution at low pH. Geochim. Cosmochim. Acta 72, 1758-1766.

Pachana, K., Zuddas, P. and Censi, P. (2012) Influence of pH and temperature on the early stage of mica alteration. Appl. Geochem. 27, 1738-1744.

Persson, P. and Axe, K. (2005) Adsorption of oxalate and malonate at the water-goethite interface: Molecular surface speciation from IR spectroscopy. Geochim. Cosmochim. Acta 69, 541-552.

Petit, J.C., Mea, G.D., Dran, J.C., Magonthier, M.C., Mando, P.A. and Paccagnella, A. (1990) Hydrated-layer formation during dissolution of complex silicate glasses and minerals. Geochim. Cosmochim. Acta 54, 1941-1955.

Pokrovsky, O.S., Schott, J. and Castillo, A. (2005) Kinetics of brucite dissolution at 25°C in the presence of organic and inorganic ligands and divalent metals. Geochim. Cosmochim. Acta 69, 905-918.

Prapaipong, P., Shock, E.L. and Koretsky, C.M. (1999) Metal-organic complexes in geochemical processes: temperature dependence of the standard thermodynamic properties of aqueous complexes between metal cations and dicarboxylate ligands. Geochim. Cosmochim. Acta 63, 2547-2577.

Putnis, A. and Putnis, C.V. (2007) The mechanism of reequilibration of solids in the presence of a fluid phase. Journal of Solid State Chemistry 180, 1783-1786.

Pyenson, H. and Tracy, P.H. (1945) A 1,10—Phenanthroline Method for the Determination of Iron in Powdered Milk. Journal of dairy science 28, 401-412.

Ramos, M.E., Cappelli, C., Rozalén, M., Fiore, S. and Huertas, F.J. (2011) Effect of lactate, glycine, and citrate on the kinetics of montmorillonite dissolution. Am. Mineral. 96, 768-780.

Ramos, M.E., Garcia-Palma, S., Rozalen, M., Johnston, C.T. and Huertas, F.J. (2014) Kinetics of montmorillonite dissolution: An experimental study of the effect of oxalate. Chemical Geology 363, 283-292.

Rimstidt, J.D. and Barnes, H.L. (1980) The kinetics of silica-water reactions. Geochim. Cosmochim. Acta 44, 1683-1699.

Rozalén, M., Brady, P.V. and Huertas, F.J. (2009a) Surface chemistry of K-montmorillonite: Ionic strength, temperature dependence and dissolution kinetics. Journal of Colloid and Interface Science 333, 474-484.

Rozalén, M. and Huertas, F.J. (2013) Comparative effect of chrysotile leaching in nitric, sulfuric and oxalic acids at room temperature. Chemical Geology 352, 134-142.

Rozalén, M., Huertas, F.J. and Brady, P.V. (2009b) Experimental study of the effect of pH and temperature on the kinetics of montmorillonite dissolution. Geochim. Cosmochim. Acta 73, 3752-3766.

Rozalén, M.L., Huertas, F.J., Brady, P.V., Cama, J., García-Palma, S. and Linares, J. (2008) Experimental study of the effect of pH on the kinetics of montmorillonite dissolution at 25 °C. Geochim. Cosmochim. Acta 72, 4224-4253.

Rufe, E. and Hochella, M.F. (1999) Quantitative assessment of reactive surface area of phlogopite during acid dissolution. Science 285, 874-876.

Ruiz-Agudo, E., Putnis, C.V., Rodriguez-Navarro, C. and Putnis, A. (2012) Mechanism of leached layer formation during chemical weathering of silicate minerals. Geology 40, 947-950.

Samson, S.D., Nagy, K.L. and Cotton Iii, W.B. (2005) Transient and quasi-steady-state dissolution of biotite at 22-25°C in high pH, sodium, nitrate, and aluminate solutions. Geochim. Cosmochim. Acta 69, 399-413.

Sánchez-Pastor, N., Aldushin, K., Jordan, G. and Schmahl, W.W. (2010) K+–Na+ exchange in phlogopite on the scale of a single layer. Geochim. Cosmochim. Acta 74, 1954-1962.

Satoh, H., Ishii, T. and Owada, H. (2013) Dissolution of compacted montmorillonite at hyperalkaline pH and 70C: in situ VSI and ex situ AFM measurements. Clay Minerals 48, 285-294.

Savage, D., Arthur, R., Watson, C., Wilson, J. and Strömberg, B. (2011) Testing geochemical models of bentonite pore water evolution against laboratory experimental data. Physics and Chemistry of the Earth, Parts A/B/C 36, 1817-1829.

Shao, H., Ray, J.R. and Jun, Y.-S. (2010) Dissolution and Precipitation of Clay Minerals under Geologic CO2 Sequestration Conditions: CO2−Brine−Phlogopite Interactions. Environmental Science & Technology 44, 5999-6005.

Shao, H., Ray, J.R. and Jun, Y.-S. (2011) Effects of organic ligands on supercritical CO2-induced phlogopite dissolution and secondary mineral formation. Chemical Geology 290, 121-132.

Song, S.K. and Huang, P.M. (1988) Dynamics of Potassium Release from Potassium-Bearing Minerals as Influenced by Oxalic and Citric Acids. Soil Sci. Soc. Am. J. 52, 383-390.

Sorai, M., Ohsumi, T., Ishikawa, M. and Tsukamoto, K. (2007) Feldspar dissolution rates measured using phase-shift interferometry: Implications to CO2 underground sequestration. Appl. Geochem. 22, 2795–2809.

Steefel, C.I. (2009) CrunchFlow. Software for Modeling Multicomponent Reactive Flow and Transport. User's Manual. Lawrence Berkeley National Laboratory, Berkeley, USA.

Steefel, C.I., Appelo, C.A.J., Arora, B., Jacques, D., Kalbacher, T., Kolditz, O., Lagneau, V., Lichtner, P.C., Mayer, K.U., Meeussen, J.C.L., Molins, S., Moulton, D., Shao, H., Šimůnek, J., Spycher, N., Yabusaki, S.B. and Yeh, G.T. (2014) Reactive transport codes for subsurface environmental simulation. Comput Geosci, 1-34.

Stübner, K., Jonckheere, R. and Ratschbacher, L. (2008) Revelation of nuclear tracks and dislocations: A Monte Carlo simulation of mineral etching. Geochim. Cosmochim. Acta 72, 3184-3199.

Stübner, K. and Jonckheere, R.C. (2006) A Monte-Carlo calculation of the size distribution of latent alpha-recoil tracks in phlogopite: Implications for the recoil-track dating method. Radiation Measurements 41, 55-64.

Stumm, W. (1986) Coordinative interactions between soil solids and water — An aquatic chemist's point of view. Geoderma 38, 19-30.

Stumm, W. (1997) Reactivity at the mineral-water interface: dissolution and inhibition. Colloids and Surfaces A: Physicochemical and Engineering Aspects 120, 143-166.

Taylor, A.S., Blum, J.D. and Lasaga, A.C. (2000a) The dependence of labradorite dissolution and Sr isotope release rates on solution saturation state. Geochim. Cosmochim. Acta 64, 2389-2400.

Taylor, A.S., Blum, J.D., Lasaga, A.C. and MacInnis, I.N. (2000b) Kinetics of dissolution and Sr release during biotite and phlogopite weathering. Geochim. Cosmochim. Acta 64, 1191-1208.

Tournassat, C., Neaman, A., Villieras, F., Bosbach, D. and Charlet, L. (2003) Nanomorphology of montmorillonite particles: Estimation of the clay edge sorption site density by low-pressure gas adsorption and AFM observations. Am. Mineral. 88, 1989-1995.

Tu, S.-X., Guo, Z.-F. and Sun, J.-H. (2007) Effect of Oxalic Acid on Potassium Release from Typical Chinese Soils and Minerals. Pedosphere 17, 457-466.

Turpault, M.P. and Trotignon, L. (1994) The dissolution of biotite single crystals in dilute HNO3 at 24°C: Evidence of an anisotropic corrosion process of micas in acidic solutions. Geochim. Cosmochim. Acta 58, 2761-2775.

Ueta, S., Satoh, H., Kato, H., Ueda, A. and Tsukamoto, K. (2013a) A novel technique of in situ phase-shift interferometry applied for faint dissolution of bulky montmorillonite in alkaline solution. Journal of Nuclear Science and Technology 50, 731-741.

Ueta, S., Satoh, H., Nishimura, Y., Ueda, A. and Tsukamoto, K. (2013b) Dynamic and topographic observation of calcite dissolution using enhanced in-situ phase-shift interferometry. J. Cryst. Growth 363, 294-299.

van der Hoek, B., Van Enckevort, W.J.P. and Van Der Linden, W.H. (1983) Dissolution kinetics and etch pit studies of potassium aluminium sulphate. J. Cryst. Growth 61, 181-193.

Van Driessche, A.E.S., García-Ruíz, J.M., Tsukamoto, K., Patiño-Lopez, L.D. and Satoh, H. (2011) Ultraslow growth rates of giant gypsum crystals. Proceedings of the National Academy of Sciences 108, 15721-15726.

Varadachari, C., Barman, A.K. and Ghosh, K. (1994) Weathering of silicate minerals by organic acids II. Nature of residual products. Geoderma 61, 251-268.

Vieillard, P. (2000) A new method for the prediction of Gibbs free energies of formation of hydrated clay minerals based on the electronegativity scale. Clays Clay Miner. 48, 459-473.

Vinson, M.D. and Lüttge, A. (2005) Multiple length-scale kinetics: an integrated study of calcite dissolution rates and strontium inhibition. American Journal of Science 305, 119-146.

Wang, X., Li, Q., Hu, H., Zhang, T. and Zhou, Y. (2005) Dissolution of kaolinite induced by citric, oxalic, and malic acids. Journal of Colloid and Interface Science 290, 481-488.

Welch, S.A. and Ullman, W.J. (1993) The effect of organic acids on plagioclase dissolution rates and stoichiometry. Geochim. Cosmochim. Acta 57, 2725-2736.

White, A.F. and Brantley, S.L. (2003) The effect of time on the weathering of silicate minerals: why do weathering rates differ in the laboratory and field? Chemical Geology 202, 479-506.

Wieland, E. and Stumm, W. (1992) Dissolution kinetics of kaolinite in acidic aqueous solutions at 25°C. Geochim. Cosmochim. Acta 56, 3339-3355.

Wolery, T.J. (1992a) EQ3/6, A Software Package for Geochemical Modeling of Aqueous Systems: Package Overview and Installation Guide (Version 7.0).

Wolery, T.J. (1992b) EQ3NR, A Computer Program for Geochemical Aqueous Speciation-Solubility Calculations: Theoretical Manual, User's Guide, and Related Documentation (Version 7.0).

Yang, L. and Steefel, C.I. (2008) Kaolinite dissolution and precipitation kinetics at 22 °C and pH 4. Geochim. Cosmochim. Acta 72, 99-116.

Yokoyama, S., Kuroda, M. and Sato, T. (2005) Atomic force microscopy study of montmorillonite dissolution under highly alkaline conditions Clays Clay Miner. 53, 147-154.

Zhang, S., Yang, L., DePaolo, D.J. and Steefel, C.I. (2015) Chemical affinity and pH effects on chlorite dissolution kinetics under geological CO2 sequestration related conditions. Chemical Geology 396, 208-217.

Zysset, M. and Schindler, P.W. (1996) The proton promoted dissolution kinetics of K-montmorillonite. Geochim. Cosmochim. Acta 60, 921-931.

7 Appendix I

Solid treatment, analytical methodology and reactive transport modeling data

7.1 Sample preparation

7.1.1 Smectite extraction

Flow-through experiments were performed on the < 4 μm[4b] fraction corresponding to a material composed of smectite almost 100%. This fraction was extracted from bentonite (El Cortijo de Archidona deposit, Cabo de Gata, Almería) by suspension-sedimentation cycles in ultrapure water. Particle sedimentation follows the Stokes law:

$$h = -\frac{2}{9}\frac{(\rho_S - \rho_l)}{\mu} \cdot g r^2 t$$

where

- h is the path travelled by particles with radius > r (height of solution containing the fraction < 4 μm),
- ρ_s is solid density,
- ρ_s is fluid density,
- μ is the fluid viscosity,
- g is the gravitational acceleration and
- t the time.

Procedure:

- Suspend 40 g of bentonite in 2 L of ultrapure water and shake suspension for 20 min with mechanic shaker
- disperse clay using an ultrasound probe for 3 min
- shake again the suspension for another 20 min with the mechanic shaker
- let the suspension settle for 1 h and 45 min at 25°C
- discard upper 10 cm of clay suspension, where fraction < 4 μm is contained
- clay slurry is dried at 40°C in oven, and the solid clay is ground with agate mortar and stored in plastic bottle.

7.1.2 Preparation of homoionic K-smectite

The smectite was saturated with K^+ by suspension in KCl solution.

Procedure:

- suspend 1 g of smectite in centrifuge tube with 50 mL of 0.1 mol·L^{-1} KCl, and shake vigorously for 20 min
- centrifuge suspension for 20 min at 5000 rpm and discard supernatant liquid
- repeat the suspension-centrifugation twice
- rinse the solid with 0.01 mol·L^{-1} KCl three times
- rinse solid with ultrapure water to remove Cl as indicated by $AgNO_3$
- dry residue at 40°C and grind solid with an agate mortar.

7.2 Chemical analysis

7.2.1 Si analysis

Si concentration in the output solutions was determined by colorimetry by using the molybdate blue method (Grasshoff et al., 1983). This method is based on the capacity of ammonium molybdate to form a yellow complex with silica in acidic media. The complex is reduced to form a silicomolybdate blue complex. This reaction is favored with a soft heat of the solutions.

Equipment:

- Perkin Elmer Lambda 25 UV/Vis spectrometer set at 825 nm
- Spectrophotometric cuvettes (quartz or disposable plastic)
- Pipettes
- Polyethylene vials (20 mL) with caps

Reagents:

- Ammonium molybdate solution: Dissolve 7.5 g of ammonium molybdate ($(NH_4)_6Mo_7O_{24}·4H_2O$) in 75 mL of Milli Q water. Introduce in an ice bath and add little by little 25 mL of 1:1 H_2SO_4.
- Tartaric acid solution: Prepare a 10% (weight) aqueous solution. It is necessary to take in account the biological activity and the appearance of sediments. To prevent fungi development, add a crystal of thymol or sodium azide (final concentration 2 ppm).
- Reductant solution: Dissolve 0.07 g of Na_2SO_3 in 1 mL of Milli Q water. Add 0.015 g of 1-amino-2-naphthol-4-sulfonic acid and shake until it is complete dissolved. Dissolve separately 0.9 g of $Na_2S_2O_3$ in 9 mL of Milli Q water. Mix both solutions. Prepare a fresh reductant solution for every analysis.

- Acidified Milli Q water (pH ~3) (AW): Add 70 µL of HNO_3 suprapur to 1 L of Milli Q water. This solution is used for dilutions and as background, both in standard and problem solutions.

Procedure:

Standard solutions: Prepare a 50 ppm Si solution from a stock standard solution of 1000 ppm. Store in cold to avoid evaporation. Prepare standard solutions from the 50 ppm solution with Si concentration of 0.05, 0.10, 0.15, 0.20, 0.25, 0.30, 0.40 and 0.50 ppm. Acidify all solutions to pH 3 with HNO_3 Suprapur.

- Add 5 mL of standard or sample solution to acid cleaned vials.
- Heat the vials at 40°C for 15 minutes before the addition of the reactants.
- Add 0.1 mL of ammonium molybdate solution and keep the vials at 40°C for 15 minutes.
- Add 0.2 mL of tartaric acid solution.
- Add 0.05 mL of reductant solution, shake and heat again for 30 minutes.
- Let cold down the samples at room temperature.
- Read the absorption in a UV/Vis spectrometer at 825 nm.

  The detection limit is 5 ppb and the associate error is 5%.

7.2.2 Al analysis

Al concentration was determined by spectrofluorimetry, using lumogallion as complexing agent (Howard et al., 1986). The fluorescence involves the excitation of a fluorescent complex with a monochromatic light, and it is relaxed with the emission of a photon with a higher wavelength than the excitation one. To favor the formation of the fluorescent complex, samples were buffered at pH 4.86 and heated for two hours at 80°C.

Equipment:

- FluoDia T70 High Temperature Fluorescence Microplate Reader
- 96-well microplate
- Pipettes
- Polyethylene vials (20 mL) with caps

  Reagents:
- Acetic/acetate buffer solution (pH 5.0 ± 0.1): Weight 6.875 g of sodium acetate (Merk Suprapur) and dilute with Milli Q water in a 250 mL volumetric flask. Add 2 mL of acetic acid (Merk suprapur), shake and bring to volume.

- Lumogallion solution: Prepare a 0.1% (volume) solution in Milli Q water. Dilute 20 times to prepare a 0.005% solution for the 0-100 ppb calibration curve. For the 0-10 ppb calibration curve prepare a 0.0025% solution by diluting 40 times the initial solution.
- Acidified Milli Q water (pH ~3) (AW): Add 70 µL of HNO_3 Suprapur to 1 L of Milli Q water. This solution is used for dilutions and as background, both in standard and problem solutions.

Procedure:

Standard solutions: Prepare a 50 ppm Al solution from a stock standard solution of 1000 ppm. Prepare 2 calibration curves of 0-10 or 0-100 ppb depending on the estimated Al concentration in the samples. Acidify all the solutions to pH 3 with HNO_3 Suprapur.

- Add 2 mL of standard or sample solution to acid cleaned vials. Use acidified Milli Q water to dilute the samples.
- Buffer the samples and standards at pH 5 by adding 0.2 mL of acetic/acetate solution and shake.
- Add 0.1 mL of lumogallion solution (0.005 or 0.0025% for 0-10 or 0-100 ppb calibration curve respectively) and shake.
- Heat the samples at 80°C during 2 hours to favor the complex formation. Let cold down in a refrigerator during 1 hour.
- Add 250 µL of each sample of standard in a 96-well microplate.
- Read the microplate in a fluorimeter (microplate reader) using λ_{em}= 486 nm and λ_{ex}= 550 nm.

  The detection limit is 0.2 ppb and the associate error 5%.

7.2.3 Fe analysis

Fe concentration in the output solutions was determined by colorimetry by using the 1,10–phenanthroline method _ENREF_77. This method is based on the capacity of 1,10-phenanthroline to form a red complex with iron (II).

Equipment:

- Perkin Elmer Lambda 25 UV/Vis spectrometer set at 520 nm
- Spectrophotometric cuvettes (quartz or disposable plastic)
- Pipettes
- Polyethylene vials (20 mL) with caps

  Reagents:

- 1,10–phenanthroline solution: Prepare a 0.1% (weight) aqueous solution.
- Hydroxylamine solution: Prepare a 10% (weight) aqueous solution.
- Na-citrate solution: Prepare a 10% (weight) aqueous solution.
- Acidified Milli Q water (pH ~3) (AW): Add 70 µL of HNO_3 suprapur to 1 L of Milli Q water. This solution is used for dilutions and as background, both in standard and problem solutions.

Procedure:

Standard solutions: Prepare a 50 ppm Fe solution from a stock standard solution of 1000 ppm. Store in cold to avoid evaporation. Prepare standard solutions from the 50 ppm solution with Fe concentration from 0.05 to 1 ppm. Acidify all the solutions to pH 3 with HNO_3 suprapur.

- Add 5 mL of standard or sample solution to acid cleaned vials.
- Add 50 µL of hydroxylamine solution and leave the samples at room temperature (22-25°C) for 10 minutes.
- Add 100 µL of 1,10-phenanthroline solution. Shake.
- Add 100 µL of Na-citrate solution. Shake.
- Leave the samples at room temperature during 1h.
- Read the absorption in a UV/Vis spectrometer at 520 nm.

The detection limit was 0.2 ppm and the uncertainty was less than 3%.

7.3.4 Mg and K analysis

The concentration of Mg^{2+} and K^{+} was determined by ion chromatography. Ion chromatography is a form of liquid chromatography that uses ion-exchange resin columns and polar eluents to separate ions or polar molecules based on their interaction with the resin.

Equipment:

- Metrohm 883 Basic IC Plus Ion Chromatograph
- Metrosep C3-250 column (working pressure of approximately 12 MPa)
- Pipettes
- Polypropylene sample tubes (11 mL)

Reagents:

- Milli Q water
- Eluent: 3.5 mmol L^{-1} HNO_3

Procedure:

Prepare a 0-1 ppm calibration curves.

- Dilute the samples with Milli Q water.
- Inject the samples using a flow of 1 mL/min by setting an analysis time of 30 min.

- Read the area at the retention time of 7.5 min.

The detection limit and associated error were 1 ppb and 3%, respectively.

Table 7.1. Equilibrium constants (log K_{eq}) for equilibria in solution. Reactions are written as the destruction of 1 mol of the species Ca^{2+}, $SiO_{2(aq)}$, H^+, HCO_3^-, Al^{3+}, F^{2+}, Fe^{3+}, Mg^{2+}, K^+ and HNO_3^-.

species	$\log K_{25}$
$Al(OH)_2^+$	10.59
$Al(OH)_2^{4+}$	7.69
AlO_2^-	22.87
$AlOH^{2+}$	4.95
$CO_{2(aq)}$	-6.34
CO_3^{2-}	10.32
$CaCO_{3(aq)}$	7.01
$CaHCO_3^+$	-1.04
$CaNO_3^+$	-1.30
$MgNO_3^+$	-1.30
$CaOH^+$	12.85
$Fe(OH)_{2(aq)}$	20.60
$Fe(OH)_2^+$	5.67
$Fe(OH)_{3(aq)}$	12.00
$Fe(OH)_3^-$	31.00
$Fe(OH)_4^-$	21.60
$Fe(OH)_4^{2-}$	46.00
$Fe_2(OH)_2^{4+}$	29.50
$FeCO_{3(aq)}$	5.59
$FeCO_3^+$	-0.62
$FeHCO_3^+$	-2.72
$FeNO_3^{2+}$	-1.00
$FeOH^+$	9.50
$FeOH^{2+}$	21.90
$H_2SiO_4^{2-}$	22.96
$HAlO_{2(aq)}$	16.43
$HNO_{3(aq)}$	1.31
$HSiO_3^-$	9.94
$KOH_{(aq)}$	14.46
$Mg_4(OH)_4^{4+}$	39.75
$MgCO_{3(aq)}$	7.35
$MgHCO_3^+$	-1.03
OH^-	13.99

Table 7.2. Selectivity coefficients for exchange reactions for montmorillonite (Gaines–Thomas (1953) convection); summary of site types, site capacities, and protolysis constants and surface complexation reactions.

Selectivity coefficients for exchange reactions for montmorillonite	
Exchange reaction	**Kc; Fernández et al. (2004)**
2K-mont+Mg --> Mg-mont+2K	4.5
Summary of site types, site capacities, and protolysis constants	
site type	**site capacity (mol m^{-2})**
>SOHw	$8.8x10^{-7}$
>SOHS	$4.4x10^{-8}$
surface complexation reaction	
>SOHs + H^+ = >SOs-	-7.9
>SOHw + H^+= >SOw-	-7.9
>SOHs = H^+ + SOH2s+	4.5
>SOHw = H^+ + >SOH2w+	4.5
>SOHs + Al^{3+} = H^+ + >SOAls^{2+}	1.5
>SOHw = Al^{3+} + H^+ + >SOAlw^{2+}	1.5
>SOAls^{2+} + 2Al^{3+} = >SOs-	15.6
>SOAlw^{2+} + 2 Al^{3+} = >SOw-	15.6
Values taken for FEBEX bentonite (Bradbury and Baeyens, 1997)	

8 Appendix II

Additional data from biotite and phlogopite experiments and VSI/PSI and LCM-DIM support images

Table 8.1. Batch experiments: experimental conditions and results of biotite reacted with HNO_3 acid.

					pH≈1								
Experiment	masa (g)	T (°C)	Duration (h)	Residence time (h)	Si (µM)	Al (µM)	Mg (µM)	Fe (µM)	K (µM)	Al/Si	Mg/Si	Fe/Si	K/Si
B13_25_1	0.08	25	1194										
B13_25_1-1				167	52.6	25.6	49.0	33.8	26.1	0.49	0.93	0.64	0.50
B13_25_1-2				170	77.8	31.6	44.4	44.1	35.8	0.41	0.57	0.57	0.46
B13_25_1-3				166	89.5	32.9	44.9	45.0	34.8	0.37	0.50	0.50	0.39
B13_25_1-4				168	88.9	31.5	42.8	45.2	31.9	0.35	0.48	0.51	0.36
B13_25_1-5				167	95.9	31.8	49.8	43.8	37.2	0.33	0.52	0.46	0.39
B13_25_1-6				170	90.6	30.4	46.5	43.9	31.9	0.34	0.51	0.48	0.35
B13_25_1-7				186	101.4	32.5	50.6	43.0	33.4	0.32	0.50	0.42	0.33
B10_40_1	0.05	40	504										
B10_40_1-1				167	122.3	49.9	76.5	72.6	45.9	0.41	0.63	0.59	0.38
B10_40_1-2				170	146.8	46.2	75.3	69.4	56.0	0.31	0.51	0.47	0.38
B10_40_1-3				166	136.8	43.1	66.3	57.9	42.5	0.31	0.48	0.42	0.31
B8_50_1	0.05	50	183										
B8_50_1-1				92	146.9	56.5	32.6	84.3	74.3	0.38	0.22	0.57	0.51
B8_50_1-2				91	177.4	55.2	30.8	89.4	79.5	0.31	0.17	0.50	0.45
B30_70_1	0.03	70	284										
B30_70_1-1				121	520.9	226.8	62.9	220.3	33.2	0.44	0.12	0.42	0.06
B30_70_1-2				163	624.4	208.0	69.5	243.6	24.9	0.33	0.11	0.39	0.04
					pH≈2								
Experiment	masa (g)	T (°C)	Duration (h)	Residence time (h)	Si (µM)	Al (µM)	Mg (µM)	Fe (µM)	K (µM)	Al/Si	Mg/Si	Fe/Si	K/Si
B12_25_2	0.06	25	2087										
B12_25_2-1				167	10.5	6.6	8.0	9.3	6.7	0.62	0.76	0.88	0.64
B12_25_2-2				170	16.9	9.5	10.2	12.7	10.4	0.56	0.60	0.75	0.61
B12_25_2-3				166	19.4	9.3	10.8	12.5	9.3	0.48	0.56	0.64	0.48
B12_25_2-4				168	19.0	10.0	12.2	13.6	9.5	0.53	0.64	0.71	0.50
B12_25_2-5				167	22.2	10.8	13.6	14.2	10.4	0.49	0.61	0.64	0.47
B12_25_2-6				170	21.0	9.6	10.5	12.5	9.5	0.46	0.50	0.60	0.45
B12_25_2-7				186	24.7	11.0	11.9	14.2	10.4	0.44	0.48	0.58	0.42
B12_25_2-8				173	24.2	11.3	12.8	14.7	10.7	0.47	0.53	0.61	0.44
B12_25_2-9				144	22.3	10.2	11.9	13.6	9.9	0.46	0.53	0.61	0.45
B12_25_2-10				215	-	-	14.0	-	11.3	-	-	-	-
B12_25_2-11				168	25.0	10.3	11.3	13.8	11.8	0.41	0.45	0.55	0.47
B12_25_2-12				192	29.5	12.6	13.0	17.0	12.1	0.43	0.44	0.58	0.41
B21_40_2	0.07	40	670										
B21_40_2-1				164	29.8	15.2	8.0	21.2	9.2	0.51	0.27	0.71	0.31
B21_40_2-2				166	41.0	18.1	14.2	24.1	11.5	0.44	0.34	0.59	0.28
B21_40_2-3				174	49.3	16.0	17.7	26.7	11.7	0.33	0.36	0.54	0.24
B21_40_2-4				167	51.2	15.5	14.3	26.9	9.9	0.30	0.28	0.52	0.19
B25_40_2	0.03	40	1026										
B25_40_2-1				164	16.0	10.9	7.1	12.5	13.7	0.68	0.44	0.78	0.85
B25_40_2-2				167	23.6	12.2	10.4	14.3	14.9	0.52	0.44	0.60	0.63
B25_40_2-3				244	33.2	15.2	14.6	20.5	18.9	0.46	0.44	0.62	0.57
B25_40_2-4				116	12.4	7.1	5.5	7.7	8.0	0.58	0.45	0.62	0.65
B25_40_2-5				160	23.0	12.0	10.2	13.2	26.9	0.52	0.44	0.57	1.17
B25_40_2-6				176	29.2	13.6	12.9	15.2	19.5	0.47	0.44	0.52	0.67
B6_50_2	0.03	50	560										
B6_50_2-1				111	59.4	30.7	60.2	51.1	37.2	0.52	1.01	0.86	0.63
B6_50_2-2				117	59.7	23.8	31.9	38.3	27.6	0.40	0.54	0.64	0.46
B6_50_2-3				167	92.7	32.4	47.3	51.7	36.6	0.35	0.51	0.56	0.40
B6_50_2-4				166	79.9	24.6	36.9	40.7	28.8	0.31	0.46	0.51	0.36
B26_50_2	0.08	50	496										
B26_50_2-1				164	43.0	26.6	35.0	20.1	44.5	0.62	0.81	0.47	1.04
B26_50_2-2				167	49.2	21.2	34.1	19.4	23.3	0.43	0.69	0.39	0.47
B26_50_2-3				164	56.7	21.9	35.5	19.8	21.3	0.39	0.63	0.35	0.38
B29_70_2*	0.04	70	458										
B29_70_2-1				121	110.2		4.6	45.1	1.3	-	0.04	0.41	0.01
B29_70_2-2				163	143.5		5.0	48.7	1.3	-	0.04	0.34	0.01
B29_70_2-3				173	140.0		4.3	49.5	0.6	-	0.03	0.35	0.00
B66_70_2	0.03		336	336	93.5					-	-	-	-
*replica performed in order to collect more sample solution and used for Eapp and nH+ calculations													
					pH≈3								
Experiment	masa (g)	T (°C)	Duration (h)	Residence time (h)	Si (µM)	Al (µM)	Mg (µM)	Fe (µM)	K (µM)	Al/Si	Mg/Si	Fe/Si	K/Si
B23_25_3	0.0289	25	2693										
B23_25_3-1				505	7.1	3.8	3.5	5.5	1.9	0.54	0.50	0.77	0.27
B23_25_3-2				338	5.4	2.5	8.9	3.6	2.1	0.46	1.64	0.67	0.38
B23_25_3-3				344	3.7	1.7	4.2	3.2	2.6	0.45	1.16	0.87	0.71
B23_25_3-4				283	3.6	1.7	9.1	2.9	3.0	0.45	2.49	0.81	0.82
B23_25_3-5				218	3.3	1.5	0.9	1.9	3.4	0.45	0.28	0.59	1.03
B23_25_3-6				335	6.5	2.5	2.9	3.5	2.5	0.39	0.44	0.53	0.38
B23_25_3-7				333	6.9	2.4	23.0	3.3	2.7	0.36	3.36	0.49	0.40
B23_25_3-8				337	7.2	2.7	4.1	3.5	3.1	0.38	0.56	0.48	0.43
B24_40_3	0.0231	40	577										
B24_40_3-1				164	4.7	2.0	2.1	2.8	2.1	0.43	0.45	0.60	0.45
B24_40_3-2				167	8.5	3.1	3.8	3.7	3.8	0.36	0.44	0.43	0.44
B24_40_3-3				247	13.7	5.7	6.0	6.0	6.0	0.42	0.44	0.44	0.44
B47_70_3	0.07	70	192	192	53.1		13.1	18.4	1.8	-	0.25	0.35	0.03

Table 8.2 Batch experiments: experimental conditions and results of biotite reacted with oxalic acid.

Experiment	masa (g)	T (°C)	Residence time (h)	Si (µM)	Al (µM)	Mg (µM)	Fe (µM)	K (µM)	Al/Si	Mg/Si	Fe/Si	K/Si
Oxalic acid≈0.1M												
B37b_25_0.1	0.078	25	212	52.4	22.4	5.1	19.5	9	0.43	0.10	0.37	0.17
B56_25_0.1-1	0.074*	25	311	132.1	53.4	15.0	47.1	34	0.40	0.11	0.36	0.26
B56_25_0.1-2		25	312	103.7	50.7	10.1	35.0	21	0.49	0.10	0.34	0.20
B56_25_0.1-3		25	338	108.0	45.3	8.7	36.7	18	0.42	0.08	0.34	0.17
B56_25_0.1-4		25	360	11.8	7.2	-	3.9	-	0.61		0.33	-
B56_25_0.1-5		25	339	46.0	23.3	0.7	10.0	-	0.51	0.01	0.22	-
B58_40_0.1	0.076*	40	121	98.9	38.9	6.0	35.1	25	0.39	0.06	0.35	0.26
B65_40_0.1	0.069*	40	72	25.1	13.9	1.2	11.4	8	0.55	0.05	0.45	0.32
B38b_40_0.1	0.071	40	191	126.7	41.4	9.2	46.2	20	0.33	0.07	0.36	0.16
B53_50_0.1	0.035	50	72	64.2	28.5	7.8	24.0	18	0.44	0.12	0.37	0.28
B39b_50_0.1	0.051	50	191	190.9	53.5	9.4	60.1	27	0.28	0.05	0.31	0.14
B54_70_0.1	0.057	70	72	202.7	95.5	137.3	68.7	15	0.47	0.68	0.34	0.07
B40b_70_0.1	0.052	70	192	618.8	321.0	68.8	221.2	227	0.52	0.11	0.36	0.37
Oxalic acid≈0.01M												
B44_25_0.01-1	0.063	25	407	45.7	12.9	4.6	11.9	10	0.28	0.10	0.26	0.22
B44_25_0.01-2		25	217	34.0	6.4	-	5.8	3	0.19		0.17	0.08
B44_25_0.01-3		25	186	30.1	6.0	0.7	4.3	4	0.20	0.02	0.14	0.12
B48_25_0.01	0.017	25	212	8.1	3.0	-	3.8	-	0.37	-	0.47	-
B71_25_0.01	0.065	25	72	4.6	3.5	-	2.6	-	0.76	-	0.57	-
B49_40_0.01	0.017	40	191	18.3	7.1	-	7.4	-	0.39	-	0.41	-
B57_40_0.01	0.046*	40	121	18.7	10.9	0.8	7.4	7	0.58	0.04	0.40	0.36
B70_40_0.01	0.056	40	72	12.7	7.1	0.9	5.9	3	0.56	0.07	0.46	0.23
B51_50_0.01	0.068	50	72	39.3	15.5	3.3	15.2	7	0.40	0.08	0.39	0.17
B50_50_0.01	0.035	50	191	50.4	31.7	2.5	17.7	2	0.63	0.05	0.35	0.04
B43b_70_0.01	0.042	70	192	123.5	38.3	10.5	38.1	35	0.31	0.08	0.31	0.28
B52_70_0.01	0.055	70	72	76.5	29.7	10.8	28.2	23	0.39	0.14	0.37	0.30

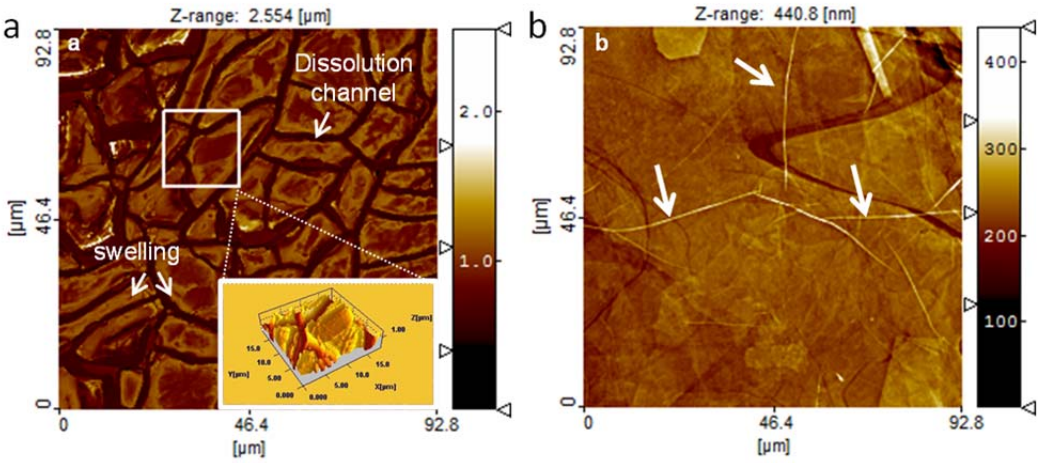

Figure 8.1 VSI image of biotite (001) surface after reaction at (a) pH 1 and 70°C for 248 h and (b) pH 2 for 96 h. At pH 1, dissolution channels formed all over the basal surface, creating islands with swelled layer edge (see inset). At pH 2, fibers formed over some areas of the basal surface (pointed out by white arrows).

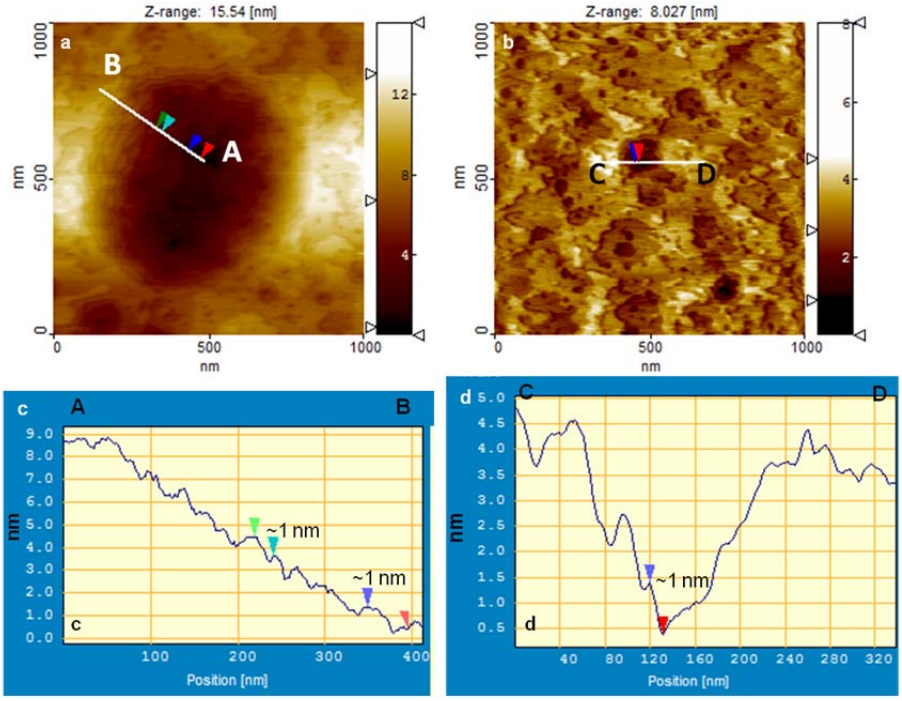

Figure 8.2 AFM image of biotite (001) surface after reaction with 0.1 mol L^{-1} oxalic acid at 40°C for 72 h: (a) large etch pit with stepwave patterns; (b) etched basal surface leading to an indented edge surface; (c and d) same profiles as those shown with solid lines in (a) and (b). Steps of ≈ 1 nanometer high (biotite TOT layer) were measured.

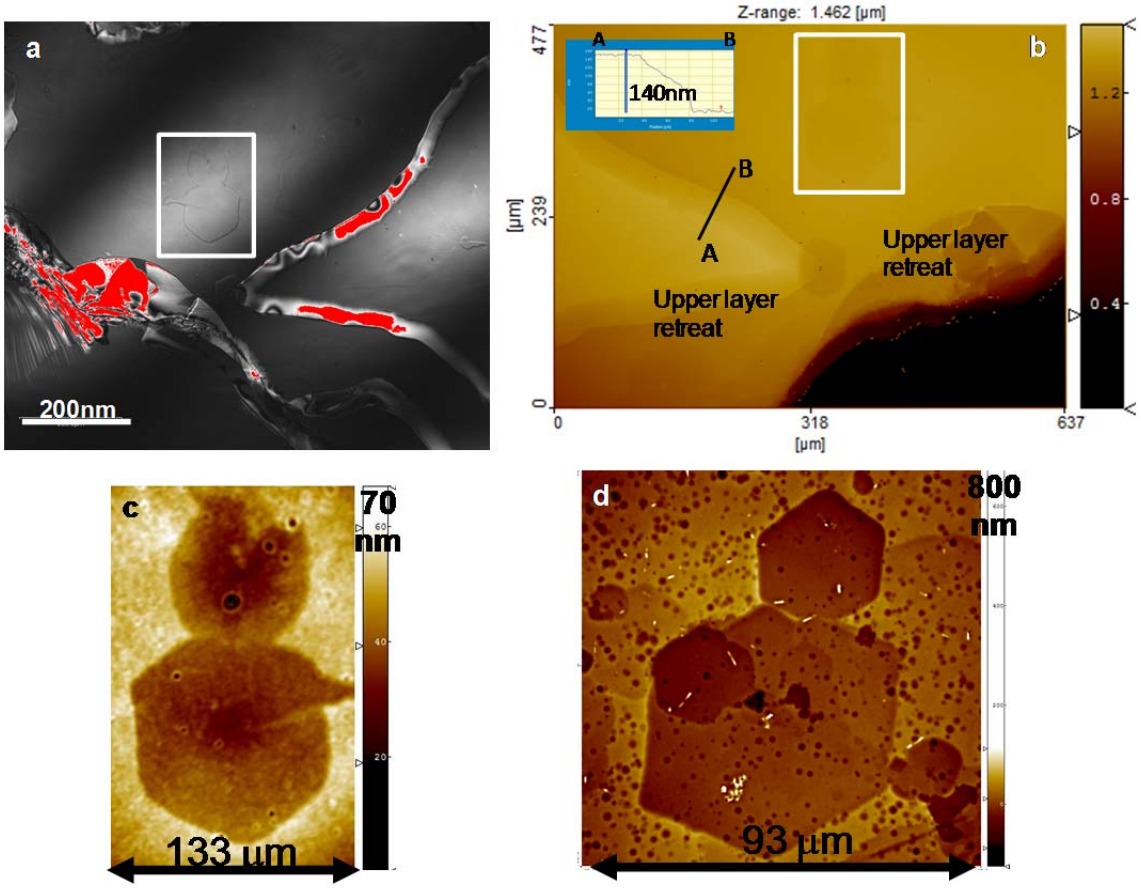

Figure 8.3 LCM-DIM image (a), PSI images (b,c) and VSI (d) of biotite (001) surface after reaction with 0.1 mol L^{-1} oxalic acid at 50°C for 18 (a-c) and 72h (d). Layer retreat occurred and large hexagonal and small rounded shaped etch pits formed. No branched fingering dissolution structures formed.

9 Appendix III

Labview scripts and output images

Hole Volume Estimation Procedure

Profile interferometric images were processed by means of three Labview scripts written ad-hoc for the application. The goal was to identify, count and measure the volume of each hole in each image. Scripts are based on Labview routines from the particle analysis library.

1. ASCII_2_AIPD.vi

   a. Open ASCII file with image content
   b. Split ASCII text into Header and pixel values parts
   c. From header, scan for x, y sizes in pixels and nanometers
   d. Create an empty numeric array (double, floating point) with (x,y) size
   e. Convert pixel string into numeric values and fill the array with.
   f. Calculate square pixel size
   g. Generate image name according to format: Originalname_pxz[pixelsize]pxz.aipd
   h. Save file in labview AIPD format for float images

2. Generate_Reference_Plane.vi

   a. Open AIPD float Image
   b. If image size is too big, resample to a smaller size for processing
   c. For n=1 to Scan size, perform a Cubic spline smoothing for a range of smoothing parameter.
      i. Substract the raw and smoothed Image
      ii. Calculate the image mean pixel value
   d. 4. Calculate the mean pixel value derivative against smoothing value
   e. 5. Sort the Smoothing value corresponding to a minima in derivative value
   f. 6. Choose to keep the sorted value or to introduce a manual smoothing parameter
   g. 7. Recalculate plane with chosen smoothing parameter
   h. 8. Generate reference plane image name according to format: Originalname_cspl[smoothparametervalue]cspl_planefitted.aipd
   i. 9. Save reference plane image (same folder as raw)

3. Hole_Volume_Meter.vi

a. Allocate memory for U8 and float images
b. Invert image histogram
c. Filter the image based on a convolution kernel and a median filter
d. Display threshold image with a binary palette
e. Fill in holes in the particles
f. Filter out all very small particles and non-circular particles
g. Return center of mass, first piyel *y* coordinate, and area for each identified particle
h. Overlay area value close to each particle in the image
i. Convert the raw image to RGB format
j. Overlay a transparency mask with particles on the raw image
k. Calculate volume of holes, one by one
l. Save values to a spreadsheet file
m. Normalize each hole volume, against the maximum and minimum hole volumes
n. Overlay normalized volume on raw image
o. Save as png file.

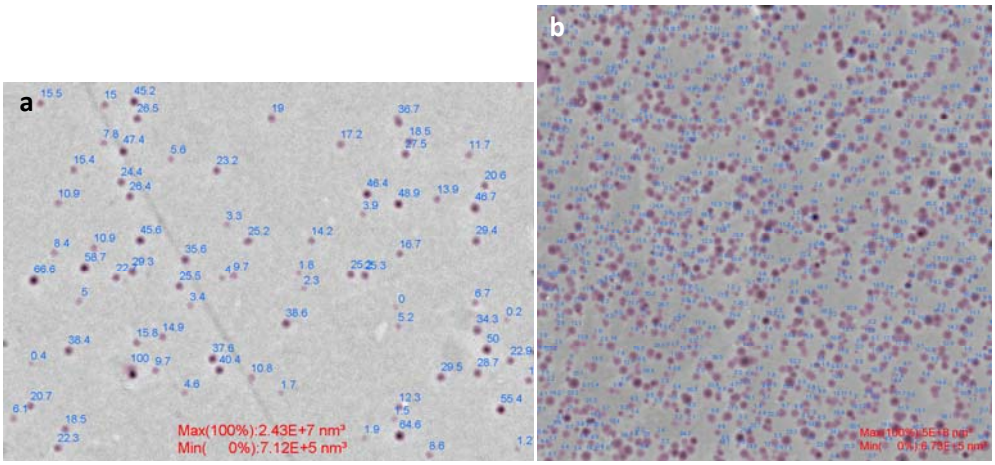

Figure 9.1 Labview output images of biotite (001) surface reacted at: (a) 25°C for 212 h and (b) 50°C for 72h in the presence of 0.1 M oxalic acid. Dots are etch pits homogenously distributed all over the surface.

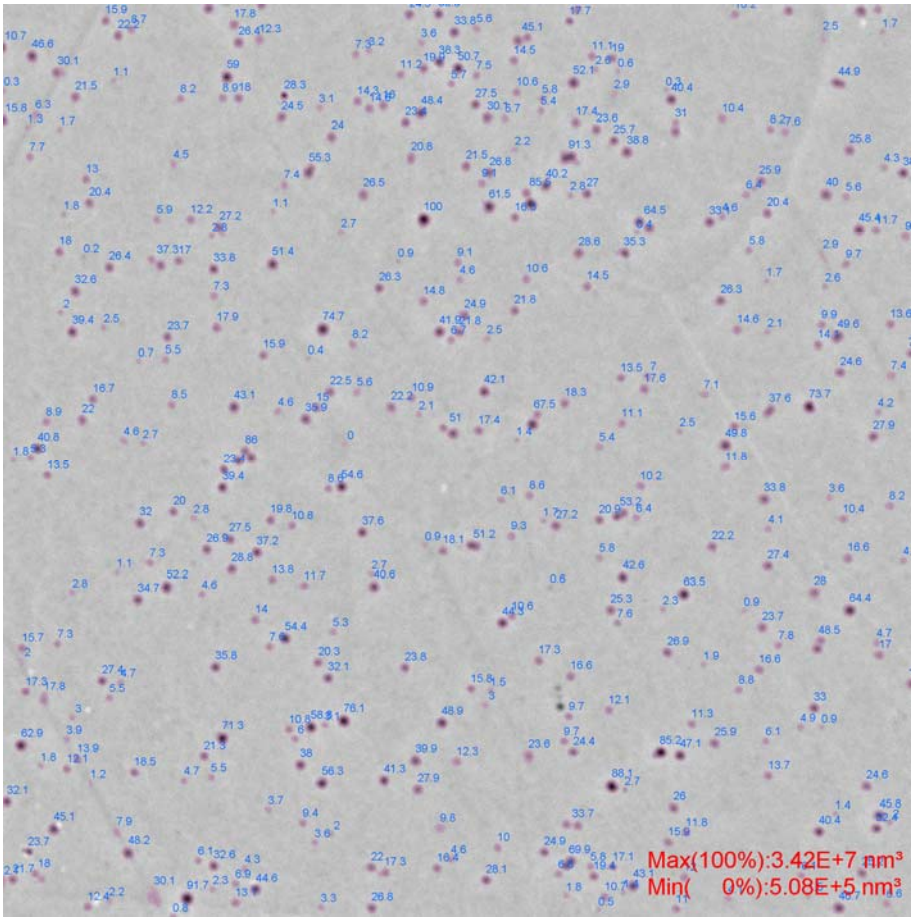

Figure 9.2 Labview output image of biotite (001) surface reacted at 50°C for 72h in the presence of 0.01 M oxalic acid. Dots are etch pits homogenously distributed all over the surface.